UNIVERSIDADE TÉCNICA DO ATLÂNTICO
INSTITUTO DE ENGENHARIA E CIÊNCIAS DO MAR

WEST AFRICAN SCIENCE SERVICE CENTRE ON CLIMATE CHANGE AND ADAPTED LAND USE

Master Thesis

FLUXES OF ATMOSPHERIC NUTRIENTS DURING DUST EVENTS TO THE ATLANTIC OCEAN AND THEIR IMPACT ON REGIONAL OCEAN PRODUCTIVITY

NONGMA KABORE

Master Research Program on Climate Change and Marine Sciences

São Vicente
2023

UNIVERSIDADE TÉCNICA DO ATLÂNTICO
INSTITUTO DE ENGENHARIA E CIÊNCIAS DO MAR

WEST AFRICAN SCIENCE SERVICE CENTRE ON CLIMATE CHANGE AND ADAPTED LAND USE

Master Thesis

FLUXES OF ATMOSPHERIC NUTRIENTS DURING DUST EVENTS TO THE ATLANTIC OCEAN AND THEIR IMPACT ON REGIONAL OCEAN PRODUCTIVITY

NONGMA KABORE

Master Research Program on Climate Change and Marine Sciences

Supervisor | Dr Khanneh Wadinga Fomba

Co-supervisor | Dr Corrine Almeida

São Vicente
2023

UNIVERSIDADE TÉCNICA DO ATLÂNTICO
INSTITUTO DE ENGENHARIA E CIÊNCIAS DO MAR

WEST AFRICAN SCIENCE SERVICE CENTRE ON CLIMATE CHANGE AND ADAPTED LAND USE

Fluxes of atmospheric nutrients during dust events to the Atlantic Ocean and their impact on regional Ocean Productivity

Nongma KABORE

Master's thesis presented to obtain the master's degree in Climate Change and Marine Sciences by the Institute of Engineering and Marine Sciences, Atlantic Technical University, in the framework of the West African Science Service Centre on Climate Change and Adapted Land Use

Supervisor

Dr. Khanneh Wadinga Fomba
Leipzig Institute for Tropospheric Research (TROPOS)

Co-supervisor

Dr. Corrine Almeida
Atlantic Technical University
Institute of Engineering and Marine Sciences

São Vicente
2023

UNIVERSIDADE TÉCNICA DO ATLÂNTICO
INSTITUTO DE ENGENHARIA E CIÊNCIAS DO MAR

WEST AFRICAN SCIENCE SERVICE CENTRE ON CLIMATE CHANGE AND ADAPTED LAND USE

Fluxes of atmospheric nutrients during dust events to the Atlantic Ocean and their impact on regional Ocean Productivity

Nongma KABORE

Panel defence

President

_____

Examiner 1

_____

Examiner 2

_____

São Vicente
2023

Financial support

The German Federal Ministry of Education and Research (BMBF) in the framework of the West African Science Service Centre on Climate Change and Adapted Land Use (WASCAL) through the WASCAL Graduate Studies Programme in Climate Change and Marine Sciences at the Institute for Engineering and Marine Sciences, Atlantic Technical University, Cabo Verde.

Dedication

To my late father, Ouango Kabore, who wanted to see me achieve what he wished for me, but God decided otherwise and to my mother, Ouango Kagambega, to my sisters, Vongonogo kabore and Kouilpoko Kabore, who finally have their son and brother back.

Acknowledgements

I would like to express my sincere thanks to the German federal ministry of education and research (BMBF) and the West African Science Service Centre on Climate Change and Adapted Land Use (WASCAL) Graduate Studies Programme for awarding me the scholarship for my study. My thanks go to the Atlantic Technical University (UTA)-Institute of Engineering and Marine Sciences (ISECMAR) for the admission and the provision of a good study environment. Thanks to the WASCAL-CV staff for their invaluable assistance in solving academic, administrative, and financial issues. I also want to thank Dr Bjorn Fiedler and the ocean science centre Mindelo (OSCM) staff for providing lab facilities during the data collection. I thank the Cape Verde Atmospheric Observatory (CVAO) staff and Luis Neves for providing me space and instruments and for helping in the collection of aerosol and weather data.

I sincerely thank my supervisors, Dr Khanneh Wadinga Fomba and Dr Corrine Almeida, for their honest, continued, and invaluable support, mentorship, scholarly encouragement, and fair criticism during this long and meaningful time. Their intuition and creativity led to many promising directions. My honest gratitude also goes to Prof Hartmut Herrmann for allowing me to intern at Leibniz Institute for Tropospheric Research (TROPOS) and for providing laboratory space and instruments at the Atmospheric Chemistry Department.

I thank Nabil Deabji and Eduardo Santos Souza for their excellent support during my laboratory analysis in the TROPOS laboratory. I would also like to thank Ivanice Monteiro Silva for assisting me during the biological data filtration phase at OSCM. I thank Paulo Alexandre Vasconcelos for his support during the seawater data collection in Calhau. My special thanks go to Prof Nilton Evora do Rosario for advice. I thank Dr Estanislau Baptista Lima for the linguistic improvements to my manuscripts and for reviewing the preliminary thesis. Thanks to all my colleagues for making my stay in Cape Verde unforgettable and making this project possible.

I sincerely thank my dear family for the patience, encouragement, and love they have shown me throughout my graduate years. I cannot find a way to express my gratitude to my mother, Mrs Ouango Kagambega, for her unconditional love and for being there for me every step of the way. Thank you for your love and support

Finally, I salute and bless all the people not mentioned above who have assisted me in any way during the completion of this work.

Resumo

As alterações ambientais e atividades humanas aumentam partículas antropogênicas nos ecossistemas marinhos, afetando o crescimento e produção de fitoplâncton. Para entender a resposta de ecossistemas oligotróficos à deposição atmosférica durante episódios de poeira, coletaram-se 22 amostras de PM_{10} na estação do Observatório Atmosférico de Cabo Verde (CVAO). A partir destas amostras, foram determinados os fluxos de iões inorgânicos e metais vestigiais depositados e o seu potencial impacto na produção primária. As amostras foram recolhidas utilizando um amostrador de baixo volume em filtros de fibra de quartzo de 37 mm de diâmetro, de 27 de janeiro a 18 de fevereiro de 2022. As espécies investigadas incluíram NO_3^-, NO_2^-, NH_4^+, PO_4^{3-}, SO_4^{2-}, K^+, Mg^{2+}, Ca^{2+}, Al, Fe, Ti, P, Zn, V, Ni, e Cr. Os dados do satélite Copernicus foram utilizados para investigar os eventuais impactos das poeiras nos ecossistemas. Os resultados mostraram que a concentração de PM_{10} durante os eventos de poeira (118,80 µg m^{-3}) foi sete vezes mais elevada do que nos eventos sem poeira (16,64 µg m^{-3}). A análise química mostrou que as concentrações de metais vestigiais e iões inorgânicos durante os episódios de poeira foram muito diferentes das dos dias sem poeira, com aumentos que variaram de 4 a 144% para os iões e de 3 a 642% para os elementos vestigiais.

A análise da trajectória inversa indicou que os mecanismos de mistura durante a rota de transporte podem afectar as concentrações das espécies. Zn, NO_2^-, NH_4^+, e PO_4^{3-} tiveram baixas taxas de deposição no oceano após as tempestades de poeira, enquanto os outros nutrientes como NO_3^-, SO_4^{2-}, K^+, Mg^{2+}, Ca^{2+}, Al, Fe, e Ti mostraram taxas de deposição mais rápidas. Utilizando um modelo de deposição não linear, estimámos os fluxos de deposição seca, com fluxos médios de azoto inorgânico dissolvido (DIN = NO_3^- + NO_2^- + NH_4^+) e PO_4^{3-} de 2,6 e 0,04 µmol m^{-2} d^{-1}, respectivamente, durante os eventos de poeira, e 1,8 e 0,03 µmol m^{-2} d^{-1}, respectivamente, durante os eventos sem poeira. Os rácios N/P inorgânicos foram superiores ao rácio de Redfield, indicando um aumento da entrada de nutrientes e potenciais limitações de fósforo nas águas circundantes. Os dados de satélite mostraram um aumento da clorofila a e da biomassa de fitoplâncton após os episódios de poeira. Conseguimos captar com êxito as flutuações da entrada de nutrientes na atmosfera através de medições laboratoriais do teor de nutrientes em partículas. O estudo aprimorou o entendimento dos impactos da poeira na vida marinha, destacando a necessidade de mais pesquisas para compreender respostas específicas às altas concentrações de nutrientes.

Palavras chave: Cabo Verde, tempestade de poeira, deposição seca, nutrientes, PM_{10}

Abstract

Environmental change and human activities are increasing anthropogenic particle loads in marine ecosystems, affecting phytoplankton growth and production. To understand how oligotrophic ecosystems respond to atmospheric deposition during dust episodes, 22 PM_{10} samples were collected at the Cabo Verde Atmospheric Observatory (CVAO) station. From these samples, the fluxes of inorganic ions and trace metals deposited and their potential impact on primary production were determined. The samples were collected using a low volume sampler on 37 mm diameter quartz fiber filters from January 27 to February 18, 2022. The investigated species included NO_3^-, NO_2^-, NH_4^+, PO_4^{3-}, SO_4^{2-}, K^+, Mg^{2+}, Ca^{2+}, Al, Fe, Ti, P, Zn, V, Ni, and Cr. The Copernicus satellite data was used to investigate impacts of dust events on the marine ecosystem. The results showed that the PM_{10} concentration during the dust events (118.80 µg m^{-3}) was seven times higher than that in the non-dust events (16.64 µg m^{-3}). Chemical analysis showed that concentrations of trace metals and inorganic ions during the dust episodes were very different from those of non-dust days, with increases ranging from 4 to 144% for ions and 3 to 642% for trace elements.

The back trajectory analysis indicated that mixing mechanisms during the transport route may affect species concentrations. Zn, NO_2^-, NH_4^+, and PO_4^{3-} had low deposition rates to the ocean after dust storms, while the other nutrients such as NO_3^-, SO_4^{2-}, K^+, Mg^{2+}, Ca^{2+}, Al, Fe, and Ti showed faster deposition rates. Using a non-linear deposition model, we estimated dry deposition fluxes, with mean fluxes of dissolved inorganic nitrogen (DIN = NO_3^- + NO_2^- + NH_4^+) and PO_4^{3-} of 2.6 and 0.04 µmol m^{-2} d^{-1}, respectively, during dust events, and 1.8 and 0.03 µmol m^{-2} d^{-1}, respectively, during non-dust events. The inorganic N/P ratios were above the Redfield ratio, indicating increased nutrient input and potential phosphorus limitations in surrounding waters. Satellite data showed an increase in chlorophyll *a* and phytoplankton biomass after dust episodes. We have successfully captured atmospheric nutrient input fluctuations through laboratory measurements of nutrient content in particulate matter. This has improved our knowledge of dust deposition impacts on marine planktons and highlights the need for more research to understand the species-specific response to high nutrient inputs.

Key words: Cabo Verde, dust storm, dry deposition, nutrients, PM_{10}.

Abbreviations and acronyms

Chl *a*	Chlorophyll *a*
NETA	North-eastern Tropical Atlantic
DIN	Dissolved Inorganic Nitrogen
DIP	Dissolved Inorganic Phosphate
PM	Particulate Matter
TMs	Trace Metals
WSIIs	Water Soluble Inorganic Ions

General index

Figure index

1. Introduction

1.1 Background and Context

The interactions between the atmosphere and the ocean involve the exchange of gases, water, energy, momentum, and particles, impacting the biochemical and physical processes of the ocean, as well as the water cycle and weather patterns. The exchange of water between the ocean and the atmosphere is controlled by the biological and physical pump, with the availability of nutrients being essential for biological activity such as photosynthesis. The bioavailability of macro and micronutrients such as nitrogen, phosphorus, iron, and other trace metals is the main factor controlling the productivity and biological nitrogen fixation in marine environments (Moore et al., 2013).

The most common reactive forms of nitrogen (N) and phosphorus (P) found in marine waters are dissolved inorganic nitrogen (DIN) and dissolved inorganic phosphorus (DIP), with nitrate (NO_3^-), nitrite (NO_2^-), and ammonium (NH_4^+) being the forms of DIN, while DIP is found as phosphate (PO_4^{3-}). N, P, and iron (Fe) are the major nutrients for marine biota. These nutrients enter the ocean through riverine and atmospheric inputs, including anthropogenic emissions from agriculture and combustion processes and biological fixation and mineralization. Nitrogen and phosphorus are needed for the synthesis of the adenosine triphosphate (ATP), amino acids and proteins. Fe is a key component of ferredoxins, enzymes involved with phosphorus in nitrogen fixation reactions by cyanobacteria.

The Atlantic Ocean provides an excellent laboratory for understanding the large-scale impact of dust deposition, with marked symmetry between the North and South Atlantic regions characterised by large deposition fluxes in the North Atlantic compared to the South Atlantic (Jickells et al., 2005). The Northeast Tropical Atlantic (NETA) is a large-scale frontal system surrounding the Cape Verde Archipelago (Fernandes et al., 2005), which receives significant dust deposition from the Sahara and Sahel regions, affecting large parts of the region (Chiapello, 1997). Accordingly, nutrient delivery to this remote NETA region through dry deposition may be one of the crucial external nutrient sources. The Cape Verde Atmospheric Observation (CVAO) station is a well-characterised location for understanding remote atmospheric composition and deposition due to the lack of local human impact (K. W. Fomba et al., 2014).

1.2 Problem Statement

Global warming, dust storms, and eutrophication are impacting nutrient fluxes today, affecting food webs in terrestrial and aquatic ecosystems. Also, human activities that enrich N and P in aquatic systems alter nutrient limitation patterns, thereby affecting food webs (Van De Waal et al., 2010). The eutrophication process is caused by the excessive release of limiting factors on the growth of primary producers (Howarth et al., 2011). Marine eutrophication results in high levels of algae growth, phytoplankton growth, and reduced fish yields (increased risk of mortality). Atmospheric deposition is one of the many causes of eutrophication, and it is mainly responsible for providing the limiting nutrients N, P, and Fe to the coastal and open oceans (Krishnamurthy et al., 2010).

Previous studies have shown the responses of phytoplankton to the atmospheric deposition onto the surface of the oceans, either by satellite observation (Eker-Develi et al., 2006; von Holdt et al., 2019), use of models (Okin et al., 2011; Tagliabue & Völker, 2011; Fu et al., 2015; Abadi et al., 2020; Myriokefalitakis et al., 2020), nutrient additions (Marañón et al., 2010) or mesocosm incubation (Ridame et al., 2014; Rahav et al., 2016; Pitta et al., 2017). Furthermore, a significant amount of literature is available in phytoplankton responses to effects of the nutrient, warming and light interactions by laboratory clonal cultures (Barcelos Ramos et al., 2017; Reich et al., 2020; Schulhof et al., 2019; Verbeek et al., 2018).

Despite the apparent importance of macro and micronutrients supplied by atmospheric deposition to phytoplankton revealed by the above-cited studies, we still have limited understanding of how marine oligotrophic ecosystems respond to abrupt nutrient supply during brief dust storm events. Therefore, characterising PM_{10} (particles with an aerodynamic diameter smaller than 10 μm) composition during dust events and using satellite-derived data are key to understanding marine ecosystem response to dust outbreaks.

1.3 Scientific relevance of the Results

We argue that more atmospheric nutrient measurements during dust outbreaks are needed to evaluate dust pollution's impact on the marine ecosystem. The intended outcomes of the study are to provide:

(1) estimates of short-term fluxes of nutrients during dust events.

(2) understanding of the impact of Saharan dust pollution on the atmospheric nutrient budget and the significance of nutrient variations under dust storms that may affect the chlorophyll-a concentration around CVAO.

(3) estimates of the differences between dust and non-dust days nutrient budgets and improve our understanding of the importance of dust episodes on temporal marine productivity.

1.4 Research Questions

- What is the variation in the abundance of atmospheric-derived nutrients, especially Phosphorus, nitrite, nitrate, iron, ammonium, and potassium, before and after short dust storms?
- To what extent do these nutrients supply impact the marine ecosystem during dust storms?
- How do primary productivity indicators such as chlorophyll *a* vary?
- Could this nutrient supply during the dust events lead to the eutrophication?

1.5 Aim and objectives of the study

The study's main goal was to investigate the influence of dust events on atmospheric PM_{10} component concentration levels and their potential impact on marine primary productivity.
The objectives of the study were:

- Quantify the atmospheric concentrations of PM_{10}, water-soluble inorganic species and trace metals, and chlorophyll-a during dust and dust-free days.
- Evaluate the relationships between the PM_{10} mass concentration and surface chlorophyll *a* concentration.
- Calculate the dry deposition velocity of PM_{10} using a particle deposition model.
- Calculate the dry deposition fluxes of nutrients for each sampling date.
- Evaluate the potential impact of these nutrient fluxes on primary production.

1.6 Structure of the work

The work is presented in the following six sections: Introduction, Literature Review, Materials and Methods, Results and Discussion, Conclusion, and References. The second section is the literature review, which provides an overview of the most relevant work by various researchers related to this thesis. Materials and methods have been described in the third section, which details the approaches used to achieve the study's objectives. The results are given and discussed in the fourth section. The conclusion is shown in the fifth section; the

references are cited in the last one. The thesis is written in English with extended abstracts in Portuguese and English.

2. Literature review

This chapter first presents some definitions. Secondly, the chapter reviews the atmospheric deposition of nitrogen and phosphorus species and the influence of dust intrusion on the variability of nutrients. Finally, a review of the different impacts of atmospheric input on the ocean's marine ecosystem is given.

2.1 Definitions and factors influencing the Chlorophyll-a production

❖ Definitions

Phytoplankton are microalgae that move freely and live near the sea surface where sufficient light can be reached. The phytoplankton capture solar energy and nutrients using chlorophyll, convert inorganic carbon into organic matter and release oxygen during photosynthesis. The main types of phytoplankton are cyanobacteria, diatoms, dinoflagellates, green algae, and coccolithophores. Due to their ecological functioning, the phytoplankton can function as nitrogen fixers (cyanobacteria, e.g., Trichodesmium), calcifiers (coccolithophores), dimethyl sulphide (DMS) producers (e.g., Phaeocystis, coccolithophores, dinoflagellates) and silicification agents (e.g., diatoms) (IOCCG, 2014). *Primary production (PP)* is the production of organic matter by marine phytoplankton (Falkowski & Raven, 2007). *Gross primary production (GPP)* can be defined as the amount of carbon sequestered during photosynthesis. *Net primary production (NPP)* is GPP minus the fixed carbon used for cellular respiration by autotrophic plankton (Boyd et al., 2014). Other concepts related to PP include new production, regenerated production, and export production. The *"new production"* is the fraction of NPP supported by introducing fresh nutrients (upwelling, vertical mixing) into the photosynthetic process. The bacterial oxidation of organic material maintains *regeneration production*. The *export production* is the portion of the PP that gets deeper into the water column as Particulate Organic Carbon (POC) from the surface layers (Giering et al., 2014; Henson et al., 2015).

❖ Factors affecting the productivity and distribution of phytoplankton

Primary production is driven by environmental factors such as light, nutrient inputs, CO_2, and temperature. The oceanic and atmospheric processes such as cloudiness, mixing

systems, convection, density stratification, eddy-induced upwelling, and boundary currents, indirectly affect primary production as they affect the environmental factors.

Radiation and temperature: Irradiation is an important driving force for photosynthesis. It warms up the surface of the ocean and regulates water temperature. Photosynthesis takes place in the euphotic zone. The euphotic area extends from the surface to the photonic depth, where the photosynthetically active radiation (PAR) is reduced to 1% of its surface value (Kirk, 1994). Phytoplankton cells rapidly adapt to changes in light quantity and quality. They have developed different pigment suites to cope with different light regimes in diverse ecosystems (Barlow et al., 2013). Temperature is an important parameter affecting biological processes in the ocean. The structure of the phytoplankton community varies in a regular, predictable pattern with temperature, particularly in temperate regions (Robinson et al., 2018).

Carbon dioxide: Ocean plankton contributes to removing carbon dioxide (CO_2) from the atmosphere by sloshing particles and transporting organic carbon to the depths. This flow of carbon is called the biological pump. The input of inorganic carbon into the ocean is key for primary production. For example, Hein & Sand-Jensen (1997) have shown that in surface waters, median primary production at low CO_2 (3 mM) was 75% of the level of ambient CO_2 (10 mM) and median primary production at elevated CO_2 (36 mM) was 115% of the ambient level based on manipulation of the CO_2 concentration.

Nutrient availability and their ratios: Nutrient supply is supported either through bacteria recycling, reintroduction from deeper waters through mixing, or external sources (e.g., rivers or atmospheric deposition). The optimal macronutrient pattern of the C:N:P molar ratio for growing phytoplankton is 106:16:1 (Redfield, 1963), which means that for every 106 atoms of carbon (C) Phytoplankton transfer into organic matter, 16 atoms of nitrogen (N) and one atom of Phosphorus (P) are required. Knowing that carbon (C) is never a limiting nutrient in the environment, oceans and seas are known to be N-limited (N:P < 16) or P-limited (N:P > 16) (Tyrrell T., 1999). Fe is an enzymatically essential trace metal for photosynthesis. It may be limited to off-shelf zones as it mainly enters the marine environment through windblown dust (Ward et al., 2013). By introducing Fe into the Redfield ratio, the C: N:P: Fe molar ratio for phytoplankton growth becomes 106:16:1:0.0075 (Bristow et al., 2017). Ocean currents are important features that strongly affect nutrient availability and phytoplankton distribution. Upwelling and freshwater input bring new nutrients to the ocean's surface layer. Upwelling is the process by which nutrient-rich deep water is transported to the surface layer (Ramessur et al., 2011)

2.2 Atmospheric N and P deposition fluxes

By analysing dry and wet deposition fluxes, several estimates of atmospheric deposition fluxes have been investigated on N and P in different areas, such as rural, urban, forest, and coastal regions.

Duarte et al. (2006) assessed depositional fluxes of aerosol bound N, P, and Fe to the North-Eastern subtropical Atlantic during a cruise in May -June 2003. They reported that the dry atmospheric deposition was dominated by N input (135 ± 28 and 132 ± 94 μmol m^{-2} d^{-1} in the North and South, respectively) followed by P (3.9 ± 2.5 and 5.8 ± 5.6 μmol m^{-2} d^{-1} in the North and South, respectively) and Fe (0.4 ± 0.1 and 0.60 ± 0.29 μmol m^{-2} d^{-1} in the North and South, respectively) in the open ocean. However, the molar N/P ratio for dry deposition in the North (47 ± 37) was higher than that in the Southern region (28 ± 10) for the open ocean.

Kocak (2015) investigated the dry and wet atmospheric N and P fluxes from 8-year samples (January 1999 to December 2007) in the Eastern Mediterranean. He reported that the dry atmospheric deposition was dominated by NO_3^- input (61 μmol m^{-2} d^{-1}) followed by NH_4^+ (7 μmol m^{-2} d^{-1}) and PO_4^{3-} (0.28 μmol m^{-2} d^{-1}). However, the dry deposition of dissolved inorganic nitrogen (DIN = NO_3^- + NH_4^+) was about 35.8% of the total N deposition (dry + wet, without organic N). The atmospheric flux of nitrate was equally influenced by dry and wet (60 μmol m^{-2} d^{-1}) deposition, and the molar N/P ratio for dry (243) deposition was a factor of two higher than that for wet deposition (131).

Xing et al. (2018) investigated the concentrations and the fluxes of water of various water-soluble N and P species based on one-year samples (June 2015 to May 2016) in Jiaozhou Bay, North China. They found high and comparable dry inorganic NO_3^- and NH_4^+ fluxes (29.9 and 29.4 mmol m^{-2} yr^{-1}, respectively) compared to low NO_2^- and PO_4^{3-} fluxes (0.058 and 0.099 mmol m^{-2} yr^{-1}, respectively). They stated that the high dry deposition value associated with NH_4^+ was due to agricultural production in the northern portion of the study. Also, their results revealed that the dry atmospheric deposition of NO_3^- exceeded one-third of the total atmospheric input (35.4%), and WSIN (NO_3^- + NO_2^- + NH_4^+) accounted for approximately 80% of N dry deposition, highlighting the importance of the dry deposition of inorganic N.

Zamora et al. (2013) investigated the concentrations and the fluxes of water of various water-soluble N and soluble reactive phosphorus (SRP) species in the subtropical North Atlantic. They reported high dry deposition fluxes of DIN of 14.8 ± 6.5 and 37.9 ± 11.3 μmol

m^{-2} d^{-1}, in Barbados and Miami, respectively, whereas, dry SRP fluxes were 0.10 ± 0.03 and 0.10 ± 0.08 µmol m^{-2} d^{-1}, in Barbados and Miami, respectively

Powell et al. (2015) estimated atmospheric inputs of N, P to the Eastern Tropical North Atlantic Ocean using aerosol and rain samples collected during 28 research cruises over a 12-year period. NO_3^- and NH_4^+ dry fluxes were 7.3 and 1.4 µmol m^{-2} d^{-1}, respectively, for the North and 9.0 and 1.0 µmol m^{-2} d^{-1}, respectively, for the South Atlantic during the December-January-February season.

Milinković et al. (2022) recently estimated the dry deposition fluxes of N and P species and discussed their environmental implications at the eastern central Adriatic Sea (Croatia) from February to July 2019. They concluded that atmospheric fluxes of DIN following biomass burning events provided a significant amount of dissolved N species to the sea surface microlayer. This excess of DIN enhanced the development of phytoplankton organisms. The daily dry rates of N species, NH_4^+ and NO_3^- were 17.1 ± 15.1 and 25.4 ± 18.9 µmol m^{-2} d^{-1}, respectively, while the dry flux of PO_4^{3-} was 1.4 ± 0.3 µmol m^{-2} d^{-1} which represents 88% of the total deposition (dry + wet). Also, NH_4^+ was the dominant form in the total deposited DIN (dry + wet). The dry DIN deposition flux was 42.5 ± 32.5 µmol m^{-2} d^{-1} and the dry DIN/ PO_4^{3-} ratio was 30 ± 21.

2.3 Impact of the dust events on the characteristics of atmospheric particulate matter

The impact of dust on atmospheric particulate matter (PM) components has been investigated in several studies. Dust storms may positively impact PM concentrations during long transport in some studies.

In their study, Fomba et al. (2014) analysed the chemical composition of tropical and marine aerosols at CVAO for a period of five years from 2007 to 2011. They found that Saharan dust events have a significant impact on atmospheric inorganic species throughout the year. Fomba and his co-workers reported a significant impact of dust events on SO_4^{2-} concentration in winter with 2.46 ± 1.05 µg m^{-3}. They also reported that the substantial contribution of long transport of dust from the Sahara region and European continent to NO_3^-, NH_4^+, and non-sea Ca^{2+} with a maximum concentration of Ca^{2+} of 4.44 µg m^{-3} while the concentrations of K^+, and Mg^{2+} were more attributed to the ocean.

Rodríguez et al., (2011) investigated the origin of some aerosol species observed in the SAL that may be influenced by anthropogenic activities. PM_{10} samples were collected at the Izana Global Atmospheric Watch (GAW) observatory in Tenerife (Canary Islands) in the

North Atlantic. The authors reported a significant increase in the concentration of PM_{10}, NO_3^-, SO_4^{2-}, Fe, V, Cr, and Ni during the dust episodes compared to non-dust events.

Formenti et al., (2003) collected the dust samples during the Saharan Dust Experiment (SHADE) in September 2000 in the Cape Verde region to analyse the chemical composition. Formenti and co-workers reported that samples of the coarse fraction (particles larger than ~1 mm in diameter) were collected within or above the elevated aerosol layer, NO_3^-, SO_4^{2-}, NH_4^+, K^+, Mg^{2+}, Ca^{2+}, Al, P, Ti, V, Fe, Mn, Ni, and Zn were detected.

Gama et al., (2015) characterised a complete annual aerosol cycle over Cape Verde using ground-based observations and model results. They carried out surface aerosol measurements for a year from January 2011 to January 2012 as part of the CV-DUST project and reported that PM_{10} concentrations reach hourly values of up to 710 mg m^{-3} during dust intrusion from North West Africa.

Almeida-Silva et al. (2013) whose second aim of their study was to evaluate the influence of Saharan desert dust on the composition of local airborne particles, reported a significant increase in PM_{10}, Fe and Cr concentrations during the dust incursion.

Using a ground monitoring network, Huang et al. (2010) collected $PM_{2.5}$ and TSP from four sites during a dust storm that hit China in March-April 2007. The authors reported that dust storms impact coarse particles (2.5μm < diameter ≤ 10μm) more in dust source regions, while fine particles (diameter ≤ 2.5μm) are more impacted in downstream areas. Also, they found that Zn, Cu, and SO_4^{2-} concentrations were elevated during the dust storm due to mixing mechanisms and heterogeneous reactions on the dust surface.

Additionally, two dust storms swept across Qingdao, a coastal city near the Yellow Sea, and were monitored in March 2010 (Qi et al., 2018). Based on online and in situ measurements, the authors found that the concentration of NO_3^-, NH_4^+, SO_4^{2-}, Al, Zn, Fe, and Cr increased in dust days compared to the reference non-dust days samples. They also found that NO_3^- and SO_4^{2-} exist in many forms of metal salts in the atmospheric total suspended particles.

In March 2010, Wang et al. (2018) combined online PM_{10} and pollutant gas measurement, in situ total suspended particulates sampling, and lidar observation to investigate a super dust storm in a coastal city, Shanghai, China. They found that the formation of secondary pollution species, including NO_3^-, NH_4^+, and SO_4^{2-}, strongly depended on the ambient conditions during dust events. Low relative humidity, low temperature, strong winds, and low concentrations of pollutant gases (SO_2, NO_x, and NH_3) did not favour heterogeneous reactions on dust surfaces. Similar results were reported by (Pan et al., 2017), who also found that the

concentration of NO_3^- and Ca^{2+} increased significantly in coarse mode, particularly in high relative humidity conditions.

Based on synergetic observation and modelling results, Wang et al. (2017) investigated the impacts of heterogeneous processes on the chemical components and the mixing state of dust particles. Wang and his colleagues found that the concentration of $NH4^+$ was relatively low in the coarse mode. They also reported that fine dust particles could exist separately from anthropogenic ammonium nitrate (NH_4NO_3) and sulphate $(NH_4)_2SO_4$.

On the other hand, previous researchers reported that dust could also negatively affect the concentration of PM components during the dust pathway. For example, Zhang et al. (2010) collected $PM_{2.5}$ and TSP samples during two consecutive dust plumes over northern China in 2006. They found that NO_3^-, NH_4^+, and SO_4^{2-} concentrations were lower in intense dust storms than in weak dust storms.

Moreover, Wang et al. (2013) investigated the physicochemical properties of PM_{10} during two dust events, including March 20-21, 2010, and April 26-27, 2010. The authors found that the concentrations of NO_3^-, NH_4^+, and SO_4^{2-} were lower in dust storms than in polluted air masses.

2.4 Impact of atmospheric deposition on marine ecosystems

- **Fertilising effect on primary production**

In the last decade, various studies have shown that atmospheric deposition impacts the N, P, and Fe cycles and enhances marine productivity. Several authors have used dust addition experiments (Wuttig et al., 2013) to investigate the dissolution and loss rates of Fe, Mn, and Al, through the mesocosm experiment DUNE-2 in the Mediterranean Sea. After two consecutive dust additions, they reported that the solubility of Fe increased after the addition of dust. They also confirmed that iron (Fe), manganese (Mn), and aluminium (Al)'s dust supply correlates with increased chlorophyll-a. Similar works have also been pursued and published in the same year by others (Giovagnetti et al., 2013; Moore et al., 2013) in which atmospheric deposition is now recognised as a significant source of external iron (Fe) and other nutrients for surface waters. Iron (Fe) is a primary limiting nutrient in High Nutrient Low Chlorophyll waters. It has been shown (Aghnatios et al., 2014; M. Bressac et al., 2014; Desboeufs et al., 2014; Guieu et al., 2014; Ridame et al., 2014a) by using the DUNE method that the Sahara dust deposition is considered to play a vital role in controlling primary production in Mediterranean surface waters. Dust addition increased the Chlorophyll

concentrations and large-sized phytoplankton abundance. A strong correlation between primary production and surface chlorophyll *a* concentration was reported by (Zhang et al., 2018). Zhang and co-workers found that phytoplankton growth was limited by two or more nutrients (i.e., N–P or N + P + Fe) in the Northwest Pacific Ocean and by a single nutrient (i.e., N or P) in the Yellow Sea. In the subtropical gyre of the North-west Pacific Ocean, adding Asian mineral dust provides N–P or N + P + Fe and micro-constituents to stimulate phytoplankton growth. More recent work by (Shen et al., 2020; Du et al., 2021) using satellite and in situ data has reported that the atmospheric input during the dust events enhances the primary production in the pacific ocean. In the North Atlantic Ocean, a strong correlation between atmospheric deposition and surface chlorophyll *a* concentration has been investigated. Phytoplankton production rates in the surface ocean are influenced in the open waters by the availability of a range of nutrient elements, primarily iron, phosphorus, and nitrogen, which are supplied by atmospheric input (Bristow et al., 2010; Jickells & Moore, 2015; Zamora et al., 2010, 2013).

- **Effect on Nitrogen fixation and nutrient stoichiometry**

Rahav et al. (2016) and Chu et al. (2018) studied the impact of the atmospheric deposition on dinitrogen fixation in the Cretan Sea in the Eastern Mediterranean and the effect of Asian dust on phytoplankton growth in the South China Sea, respectively. The authors have found that N_2-fixers predominate N_2 fixation, contributing 2–4% ($P > 0.05$) of primary productivity following the mixed aerosol additions and 3–8% ($P = 0.04$) after Saharan dust addition. Rahav and co-workers emphasised that adding Saharan mineral dust with a lower N:P ratio stimulated N_2 fixation rates more than European anthropogenic aerosols with a higher N:P ratio. In the same vein, the recent publications by (Kessler et al., 2020; Zhang et al., 2020; Ridame et al., 2022; Wang et al., 2022; Wen et al., 2022) support (Rahav et al., 2016) findings that the supply ratio of Fe: N from subsurface layers is an essential element in regulating N_2 fixation rates across the tropical Northwest Pacific Ocean and in the northern South China Sea. In the Eastern Tropical North Atlantic Ocean, supply of Fe and P are known to enhance the nitrogen fixation since both nutrients co-limit the N_2 fixation in that region (Mills et al., 2004).

- **Effect on phytoplankton composition, metabolism, and structure**

Guo and his co-workers have shown an unambiguous relationship between atmospheric inputs and phytoplankton and bacterial community structures (Guo et al., 2012, 2013, 2014). The finding by Guo and co-workers have been supported by Guo himself (Guo et al., 2016) and other authors (Chien et al., 2016; Maki et al., 2016; Meng et al., 2016) by investigating through microcosm experiments in the western tropical Atlantic Ocean, Pacific, and East Chinese. The authors reported that the larger micro-phytoplankton benefit more from the atmospheric nutrient deposition than picophytoplankton and nanophytoplankton. This creates a shift in the size structure of the phytoplankton community. A relative change (changes of 24.2 to 6.9%) in the heterotrophic bacterial community in response to aerosol input.

- **Inhibitory Effect**

The dry atmospheric deposition has also been proven to have an inhibitory effect on phytoplankton growth. The negative impact is linked to the toxicity of some trace metals in the aerosols (Echeveste et al., 2012; C. Guo et al., 2012; Mackey et al., 2012)**.** Many studies have highlighted that phytoplankton growth was more inhibited after adding aerosol with high Cu than with high Cu and Fe (Liao et al., 2017; Wang et al., 2017).

As described in the literature, it has been observed that studies have been conducted to evaluate the impact of atmospheric deposition on phytoplankton growth, phytoplankton and bacterial community composition, nitrogen fixation, and chlorophyll *a* production. A few studies have involved modelling, satellite observation, and bottle incubation experiments. Atmospheric deposition of nutrients in the upper ocean affects ocean productivity differently depending on water characteristics, especially in low-nutrient, low-chlorophyll waters, such as those of the North Subtropical Atlantic Gyre. Further studies are necessary to clarify how abrupt atmospheric deposition affects ocean biota in terms of supply and demand. Studies on the way atmospheric deposition of organic and inorganic nutrients affects the upper ocean optical properties were missing.

3. Materials and Methods

A combination of field and laboratory measurements was conducted to examine dust storms' potential effects on atmospheric nutrient fluxes and their impact on ocean productivity as follow: (1) Field studies at the CVAO to collect atmospheric particulate matter (PM_{10}) samples and sea water samples during dust and non-dust events; (2) Laboratory analysis of nutrient content in PM_{10} samples; (3) Analysis of chlorophyll a concentration in seawater samples; (4) Investigation of the relationship between atmospheric input and ocean productivity.

3.1 Field Study

3.1.1 Site description

Field studies were done in the Republic of Cabo Verde, which is a volcanic archipelago of 10 large and eight islets (Figure 1). Amongst the ten Islands, nine are inhabited and one uninhabited. The archipelago is located in the North-East Tropical Atlantic (NETA) between 14° 40′ and 17° 30′ N latitudes and between 21° 30′ and 25° 30′ W longitudes. The country is about 450–600 km off the coast of Senegal. The archipelago's total land area corresponds to about 4068 km^2 (Ramalho, 2011; Faria & Fonseca, 2014). Due to its location, Cabo Verde is directly exposed to the Sahara's dust to the North Atlantic throughout the year.

The samplings were carried out on the Sao Vicente Island at 16° 51' N, 24° 52' W. With 227 km^2, Sao Vicente Island is the seventh island in the country in terms of land area compared to the other islands and has a maximum elevation of 725 m above sea level. The island of Sao Vicente is downwind of the Mauritanian coastal upwelling region off northwest Africa, an area of high marine biological productivity (Carpenter et al., 2010). The Sao Vicente Island is heavily influenced by the transport of Saharan dust from land to sea (Niedermeier et al., 2014). The average annual temperature in Sao Vicente is 23.6 ± 4.0 ◦C. It is a dry region with a maximum of 24–350 mm annual precipitation with a frequency of about 3 to 10 events per year, mainly between August and October.

The sampling of atmospheric particles was conducted at the Cape Verde Atmospheric Observatory (CVAO) station, marked as a violet star in Figure 1. The CVAO is located in Calhau on the island of So Vicente, 70 m from the coast (16° 51′ 49" N, 24° 52′ 02" W) and

about 10 m above sea level. Seawater sampling was carried out in 13 stations, between 6 and 8 km from the coastline around CVAO, as shown in green dots in Figure 1.

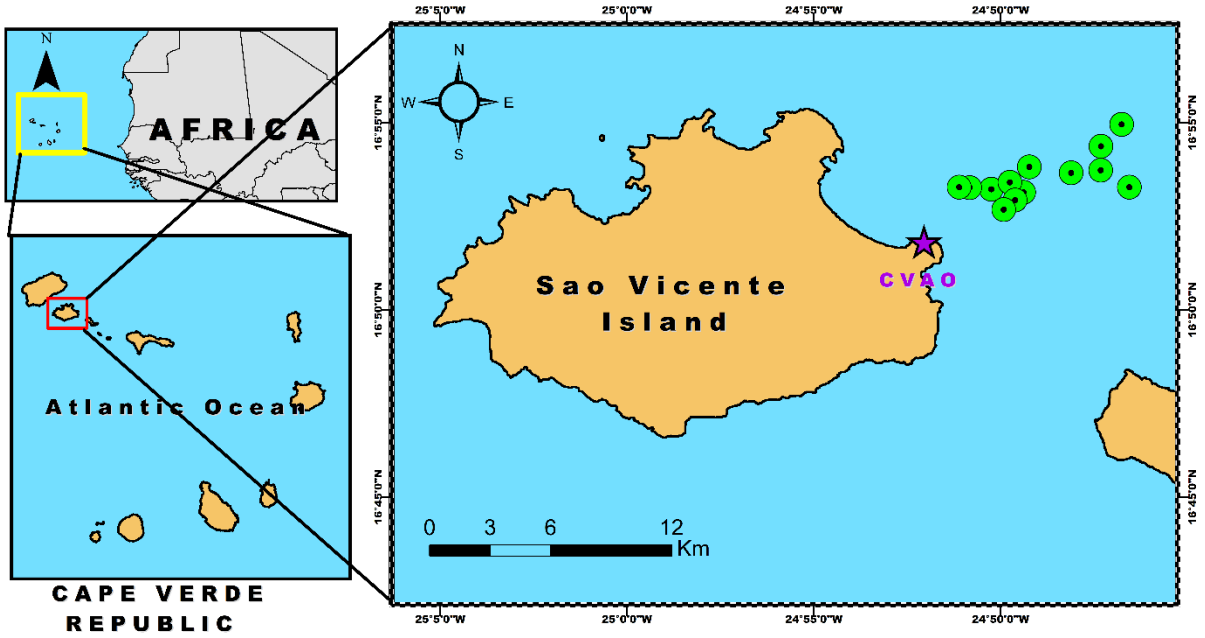

Figure 1. Map of the study area. The Cape Verde location is framed in a yellow rectangle. The Cape Verde Observatory (CVAO) on Sao Vicente Island is marked with a purple star, and seawater sampling sites are marked with green dots.

3.1.2 Collection and filtration of Seawater samples

A total of 13 seawater samples were collected daily but not continuously: eight continuous samples from January 27 to February 3, four successive samples from February 10 to February 13, and 1 sample on February 15 were collected. The seawater samples were collected at a depth of two meters using a fisherman's boat at a distance of at least 6 km (offshore sample). One litre of seawater was collected daily between 9:30 and 11:30 (local time) using a glass bottle attached to a telescopic rod to monitor the sampling depth. The bottle was opened underwater at the intended sampling depth with a specifically designed seal opener. The bottle filled with seawater was removed from the water column. After sampling, the water sample was immediately poured into clean bottles (fluoropolymer Nalgene FEP). 500 mL were filtered using 25 mm (0.7 µm) GF/F filters (Whatman, Maidstone, UK) at the Ocean Science Centre in Mindelo (OSCM) using the filtration setup shown in Figure 2). The filtered sample was transferred to a glass screw cap and stored at −20 °C until further processing. The tubes were wrapped in aluminium foil and stored at −20 °C to prevent

photodegradation of pigments. The filter samples were stored at −20 °C for chlorophyll-a analysis until analysed using Turner Designs Fluorometer onboard the Maria S. Merian cruise (MSM106).

Figure 2: Seawater samples filtration apparatus at the Ocean Science Centre in Mindelo.

3.1.3 Satellite-derived chlorophyll-a

Chlorophyll concentration and phytoplankton data were downloaded from Copernicus Marine Environment Monitoring Service (CMEMS) 's website[1] with a selected rectangular area: latitude (20, 12), longitude (−28, −20), from January 1 to May 31, 2022. The satellite-derived data was packed in Network Common Data Form (netCDF) with a gregorian daily averaged 4 km resolution.

3.1.4 Atmospheric aerosols sampling

A total of twenty-two PM_{10} samples were collected from January 27 to February 18, 2022. PM10 samples were collected continuously for 24 hours using a low-volume sampler consisting of a Gilian 12, pump (Figure 3A) and a PM_{10} impactor inlet, shown in Figure 3B, operating at a flow of 10 L min⁻1 that was mounted at the top of the 30 m tower (Figure 3C). Samples were collected on 37 mm diameter quartz fibre filters (Whatman, Quartz Filter). The filter change was always done under a fume hood (Figure 3D). After sampling, the filters

[1] https://resources.marine.copernicus.eu/

were transported and kept in a −20 °C freezer. The samples were transported from Cape Verde to Leipzig (Germany) under frozen conditions (at −20 °C) for chemical analysis.

Three dust storms marked the sampling period from January 31 to February 5, 2022, February 9–11, 2022, and February 17–18, 2022. The sample collected immediately before each dust event was regarded as the reference sample(background) for those collected during the dust storms.

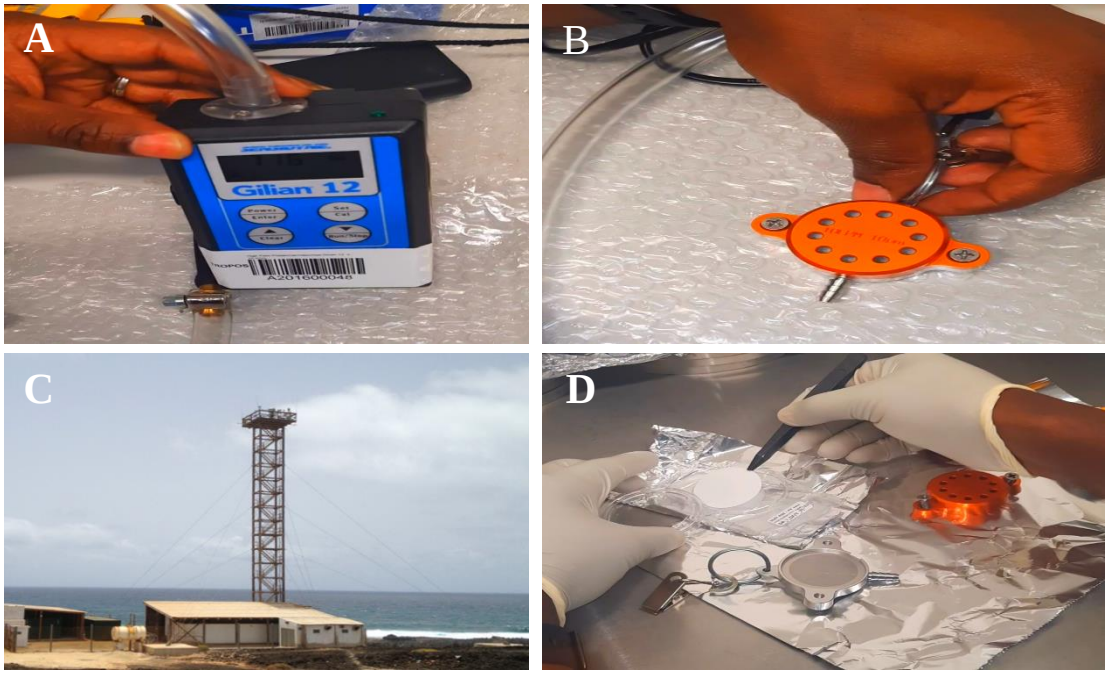

Figure 3. PM_{10} collection process. A) Gilian 12 pump. B) PM_{10} impactor inlet (PEM). C)input and removal of filter sample under a fume hood.

3.2 Laboratory Measurement

3.2.1 Chlorophyll-a Measurement

The analytical principle of the fluorometry technique will first be described, followed by the quantification of the concentration of chlorophyll *a* from the filtered samples.

- **Fluorometry principle**

The fluorometry principle, as described by Bishop (2020), is based on a luminescence and energy exchange process to measure fluorescence using fluorometry, the following essential steps need to be taken, as shown in Figure 4: First, light of short wavelength is

directed onto the sample through a primary filter that removes any unwanted radiation. When the molecules absorb this light, they become excited and then fluorescent as they return from the excited state to their ground state. Next, the fluorescence radiation emitted from the sample is filtered and recorded by a detector. Finally, the transmitted radiant energy is converted into an electrical signal by a light sensor. This signal can be further analysed and interpreted to obtain valuable information about the sample being measured.

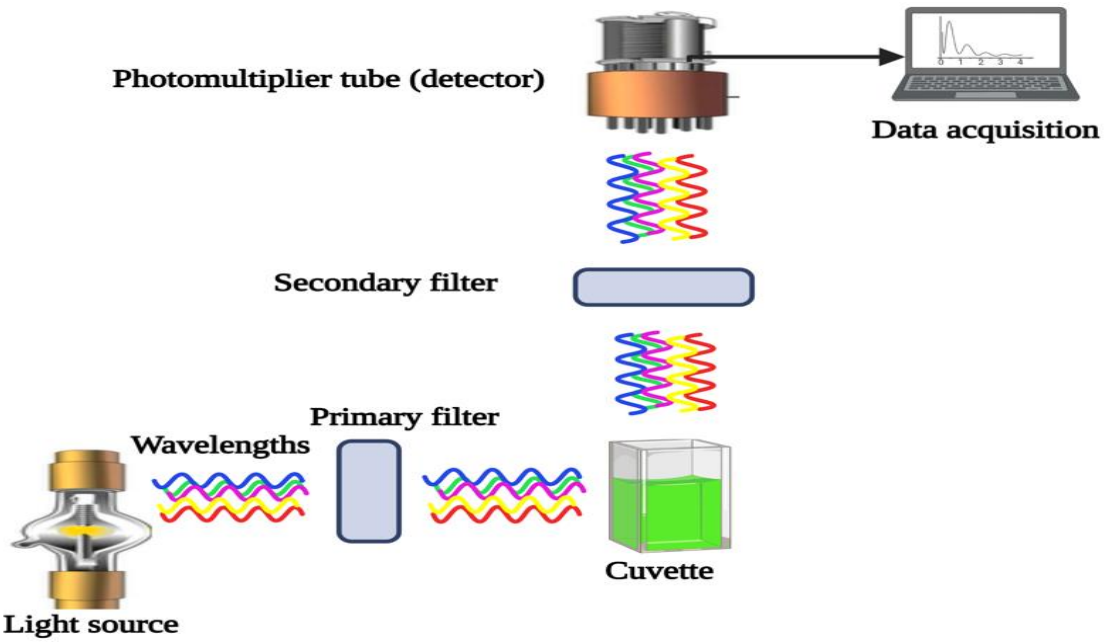

Figure 4: Design of the fluorometry setup for chlorophyll *a* measurement. Adapted from Designs, T. (2006).

- **Chlorophyll-a measurement using Turner Designs**

During the Maria S Merian cruise, samples of chlorophyll-a were measured using a Fluorometer (Turner Designs, San Jose, USA), in accordance with Designs (2006). The filter samples were taken out of the freezer (−20 °C) and extracted in 5 ml of cold (−20 °C) 100% acetone. Using an external standard of commercially available chlorophyll a (SIGMA) and zeroing out with 100% acetone, the Turner Design was calibrated following the procedure described by Strickland & Parsons, (1972). Before analysing the filter samples, they were brought to room temperature for two hours. Each sample was run twice in order to obtain two different values for calculating chl *a* concentration: one without acid and one with 2 drops of HCl (1 M). The dilution factor, the fluorometer door used, and the readings before and after acidification are recorded. The extract and filtered volumes were entered into the machine (Figure 5A), which then collected fluorescence data for each sample. The chl *a* concentration

was determined using equation 1. Finally, the concentration value was displayed on the machine's screen (Figure 5B)

$$\textbf{Chl } \boldsymbol{a} = \left(\frac{\mathbf{T}}{\mathbf{T}-\mathbf{1}}\right) \times (\mathbf{R_b} - \mathbf{R_a}) \times \mathbf{F_d} \times \left(\frac{\mathbf{Vol_{ex}}}{\mathbf{Vol_{filt}}}\right) \quad \textbf{(Eq.1)}$$

Where:

- Chl a = concentration of Chl *a* (µg/l)
- T = acidification coefficient (R_b/R_a obtained during the calibration of the fluorometer)
- R_b = reading before acidification
- R_a = reading after acidification
- F_d = door factor (µg/ (ml* reading units))
- Vol_{ex} = volume of extraction (ml)
- Vol_{filt} = volume filtered (l)

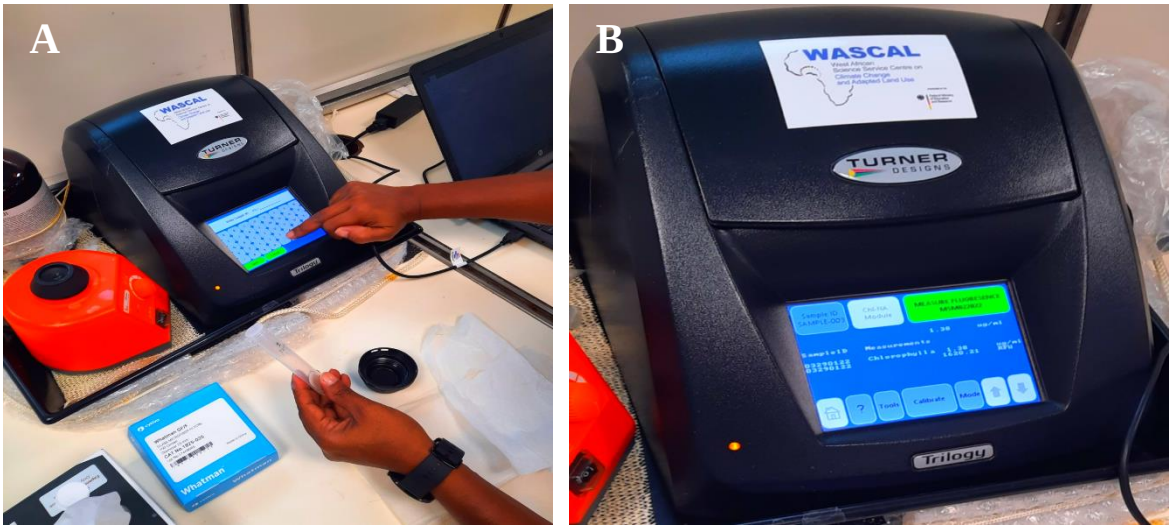

Figure 5: Chlorophyll-a measurement with Turner Designs Fluorometer: A) entering of the sample name, filtered and solvent volumes. B) the chlorophyll-a concentration displayed on the screen.

3.2.2 Particulate matter (PM_{10}) mass determination

A microbalance (Mod. XS105, DualRange, Mettler Toledo, Switzerland) was used to weigh individual filters before and after sampling, as shown in Figure 6. The mass concentration of PM_{10} was calculated as the difference in filter mass before and after sampling per unit sampling volume.

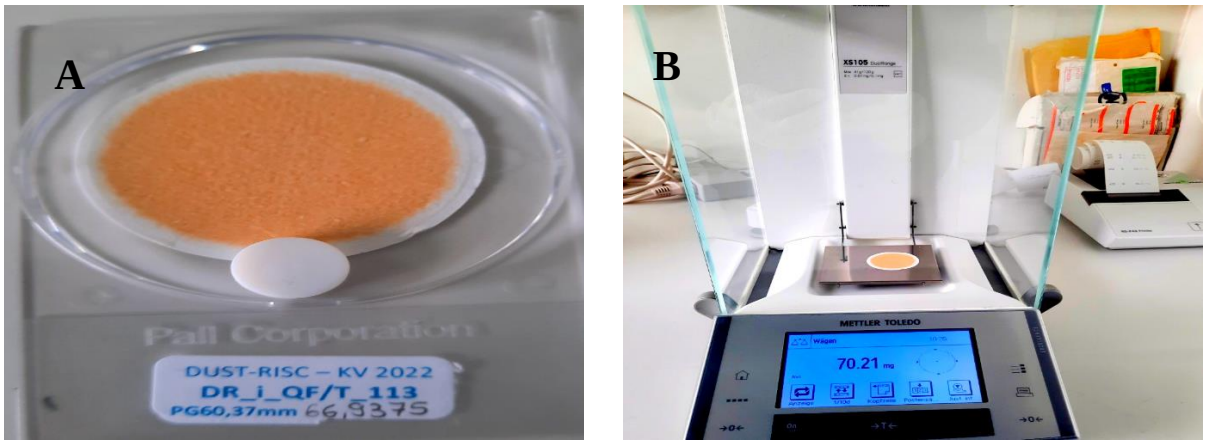

Figure 6. PM10 mass calculation. A) PM10 Sample, B) Picture of Toledo balance where filters were weighed.

3.2.3 Trace Metals Measurement

In this section, we outlined the steps for the quantitative determination of metal concentrations. These include carrier cleaning, sample digestion, internal standard preparation, and measured sample preparation. Next, we described the analytical principle of total reflection x-ray fluorescence and the S4 T-STAR machine used for measurement. Finally, we described the process for measuring the samples.

- **Carrier cleaning**

To ensure accurate measurement of elements' mass concentration and prevent overestimation due to dirty carriers, proper cleaning is essential. The carrier cleaning was done under a laboratory fume hood to prevent contamination following (Fomba et al., 2020). The carrier cleaning process comprises four main steps, as described below:

(i) Firstly, the carrier cleaning process begins by mechanically wiping each carrier using Kimberly-Clark tissue paper soaked in acetone and ethanol. This step is crucial to remove any residual dirt or contaminants on the carrier surface and is depicted in Figure 7A.

(ii) Secondly, three subsequent solutions were prepared to ensure proper cleaning. The first solution (S1) is a mixture of 400 ml of 35% HCl (Supra grade, ROTIPURAN, Roth, Germany) and deionized water in a 1:1 ratio. The second solution (S2) is a mixture of 500 ml of alkaline detergent solution (RBS 50, Roth, Germany) and deionized water in a 1:3 ratio. The third solution (S3) is a mixture of 400 ml of 69% nitric acid HNO3 (supra grade, ROTIPURAN, Roth, Germany) and deionized water in a 1:1 ratio.

(iii) Thirdly, the holder with carriers is then boiled in each of the three subsequent solutions as seen in Figure 7B, in the order of solution numbers, at 350°C for 45 minutes. After each treatment, the holder with carriers is rinsed with deionised water in an ultrasonic bath for 30 minutes (Figure 7C).

(iv) Finally, the carriers are dried in an oven for 2 to 3 hours to ensure complete drying.

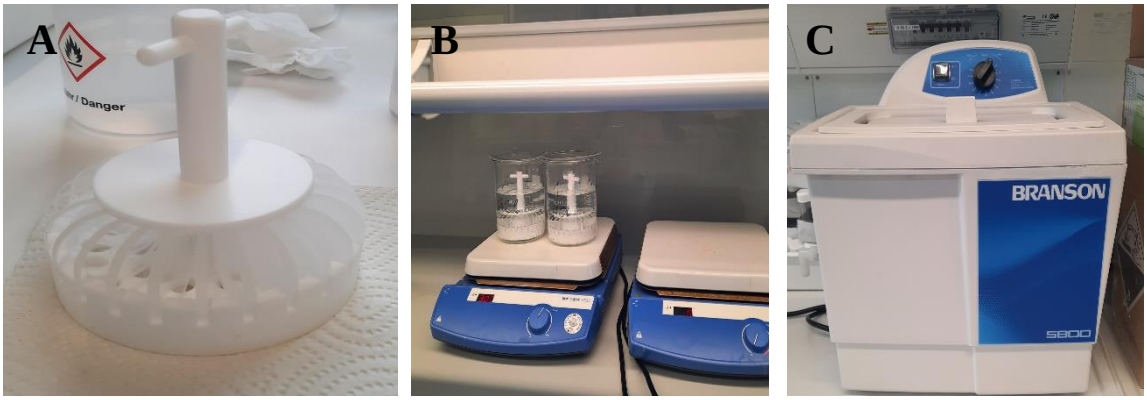

Figure 7: The cleaning of carrier process: A) The carriers are cleaned with ethanol and acetone in the carrier holder, B) The boiling of the carriers in the different acid solutions, and C) The ultrasonic batch system used for rinsing the carriers after treatment from each solution.

- **Selection of the clean carriers**

To select the clean carriers for measurement, the following steps were carried out:

(i) A volume of 0.5 µl of silicon solution was added to the centre of each carrier. This was carefully done to avoid spillage and ensure that the silicon solution was added precisely.

(ii) The carrier was then heated at 80°C for a few seconds to facilitate adhesion of the samples to the carrier's surface. This step ensured that the samples were securely attached to the carrier, which would prevent any loss of sample during measurement.

(iii) The carrier's background values were evaluated using S4 T-STAR (Bruker Nano GmbH, Berlin, Germany). This step was essential to select clean carriers for measurement, as any contamination or high background values would compromise the accuracy of the results.

(iv) Carriers with acceptable background values were selected for measurement.

By following these steps, we could ensure that the carriers were properly prepared for measurement, and only carriers with minimal background values were selected for analysis.

This would result in accurate and reliable measurement of the samples' properties, without any interference from the carrier material.

- **Sample digestion**

The digestion process is a crucial step in preparing samples for analysis and its main aim is to wash particles off the filter surface and store them in a uniform solution representing the sample for easy quantification. Here is a breakdown of the steps involved:

(i) Three spots of 8 mm in diameter were punched out of each filter using a ceramic puncher as seen in Figure 8A. These spots, which formed a total area of 1.51 cm^2, were carefully removed to ensure that they were not damaged or contaminated during the process.

(ii) The punched spots were then placed into labelled digestion vessels (Figure 8B) to keep track of the samples. The vessels were labelled in accordance with the sample number. This step ensured that the samples remained organised and could be easily identified during the digestion.

(iii) Next, the samples were digested in 1500 µl of HNO3: HCl (3:1) using microwave-assisted digestion (CEM Co., MARS), as shown in Figure 8C**.** This method allowed for efficient and rapid digestion of the samples.

(iv) After the digestion process, the solution was allowed to cool and then poured into 2 ml vials (Figure 8D). The vials were labelled as in the vessels and stored in a fridge (4.5°C) until the measurement.

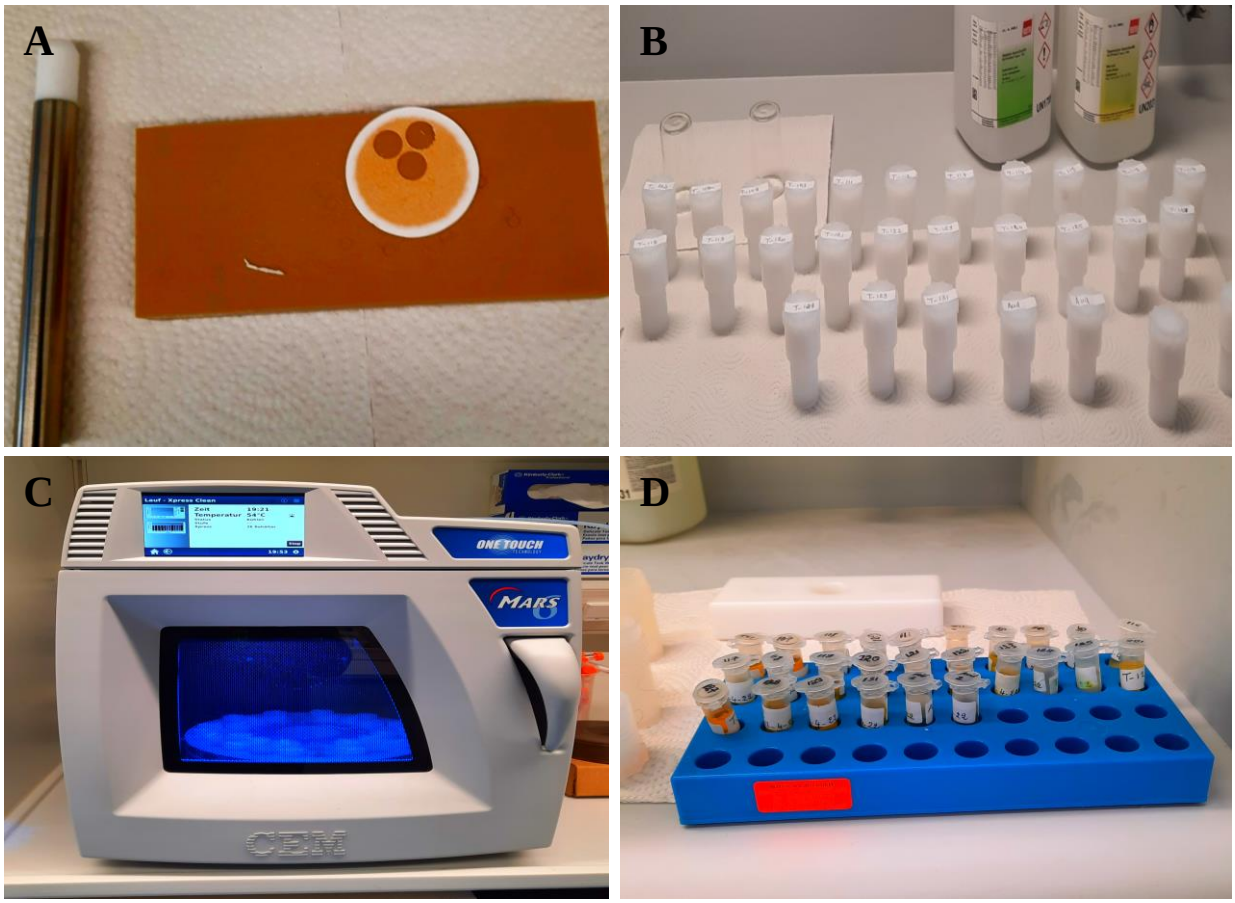

Figure 8. Sample digestion process: A) Three spots of 8 mm punched out from each sample, B) The samples placed in the digestion vessels and 1.500 mL of HNO_3 + HCl added into the vessels, C) the microwave digestion system, D) the digested samples.

- **Preparation of the internal standards**

To prepare the internal standards, two inductively coupled plasma (ICP) standard solutions were used - 1000 mg/l Gallium (from Merck, Germany) and Yttrium (from Roth, Germany). Two internal standard solutions were prepared:

(1) 2 ml of each standard solution and 16 ml of HNO_3-nitric acid 69% (from ROTIPURAN, ROT, Germany) were mixed in a 20 ml beaker, resulting in a concentration of 100 ng μl^{-1} Gallium and Yttrium in the first internal standard solution.

(2) 2 ml of the first internal standard solution were diluted with 18 ml of HNO_3 in another 20 ml beaker to obtain the second internal standard solution, which had a concentration of 10 ng μl^{-1} Gallium and Yttrium.

The two internal standards were used to prepare the sample for measurement.

- **Sample preparation**

The sample preparation process is shown in Figure 9.

(1) Firstly, an aliquot of 10 µl of each digested sample solution was pipetted onto the centre of previously cleaned and siliconized carriers. The carrier was then placed on a heating plate at 80°C for a few minutes to allow the solution to evaporate.

(2) Secondly, depending on the mass load of the sample, an aliquot of 10 ng μl^{-1}, 100 ng μl^{-1}, or 1000 ng μl^{-1} of the standard was pipetted and added to the centre of the sample carrier.

(3) Once the standards were added, the prepared sample carriers were dried on a heating plate at 80°C for a few seconds and then were ready for measurement using S4 T-STAR.

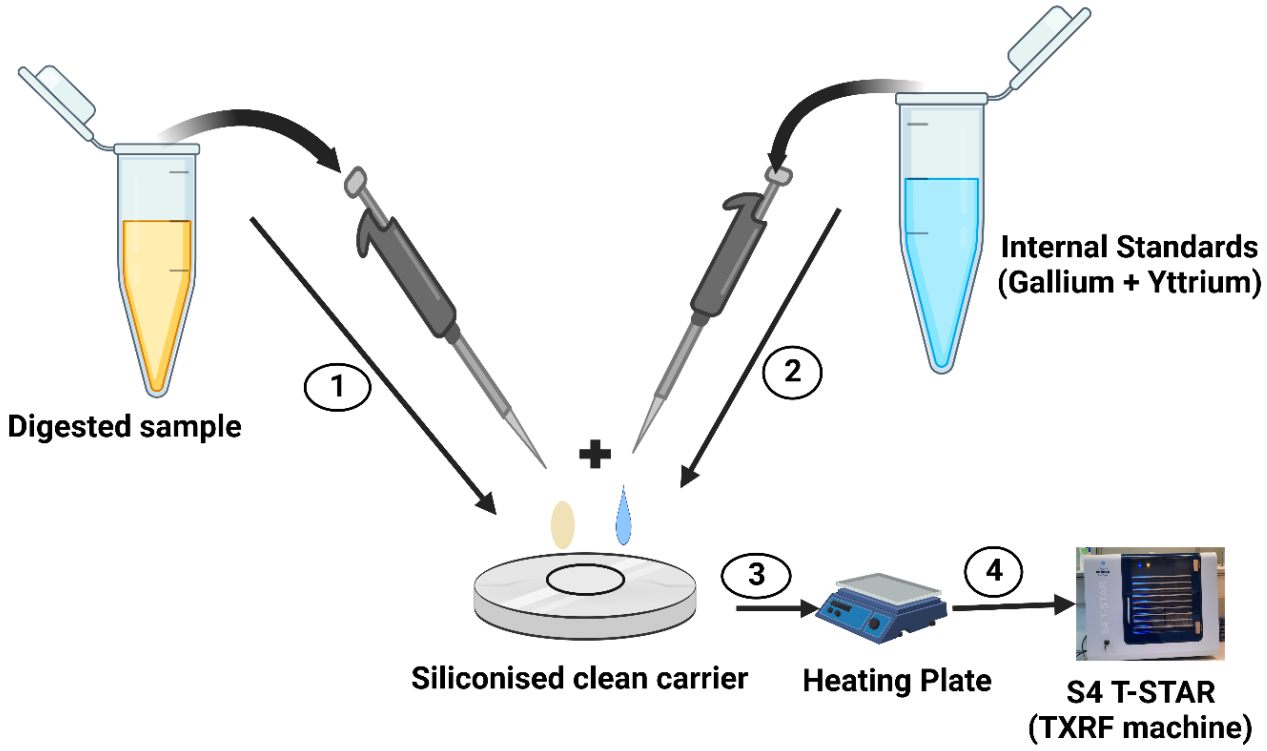

Figure 9 The Process of sample preparation: Adding the sample and standard onto the cleaned carrier in 1&2, Heating the digested sample in (3), and measuring in (4).

- **The analytical technique of total reflection x-ray fluorescence**

Trace metals were determined using the Total Reflection X-Ray Fluorescence technique (TXRF). The TXRF system has an energy source that irradiates the sample to be measured with an x-ray beam, leading to one electron vacancy, for instance, in the inner shell of the atom. This results in a transition phase in which an electron from the outer shell replaces the removed electron, and energy is released in the form of X-ray fluorescence. The specific energy value of the fluorescence associated with each transition is determined by the energy difference between the inner and outer shells, as given by Equation 2.

$$\mathbf{E_{(X-ray)} = E_K - E_L \ for\ K_\alpha\ transit} \qquad \textbf{(Eq.2)}$$

Where K_α is the irradiation resulting from an electron coming from the L shell to the inner K shell.

The TXRF system has a detector above the sample that records the different energy values and translates them into specific voltage counts and sample signal intensity. The energy values of the fluorescence signals are used to determine the trace metal concentration in the sample.

- **The analytical instrument: S4 T-STAR**

S4 T-STAR is a TXRF table spectrometer designed mainly for routine analysis of various sample types. It has a robot sample changer that handles 90 sample carriers through 10 trays and uses 30 mm sample carrier quartz discs (as shown in Figure 10). The S4 T-STAR has two microfocus X-ray tubes: one for tungsten and the other for molybdenum. Each is optimised for the characteristic fluorescence lines: Mo-K (17.5 keV) and W-L (8.5 keV).

Figure 10. The S4 T-STAR spectrometer used for the metals analysis shows the ten trays' entries and one tray on which nine carries are placed

- **Trace Metals Measurement**

The prepared samples were measured using the above-described S4 T-STAR instrument. Trace metals in PM_{10} were quantified for 500 seconds using two excitation lines (Mo and W). Trays with samples were rotated at 90° angles and measured again. The rotation makes it possible to measure the preparation off the centre of the carrier outside a 1 cm diameter circle, thus increasing the probability of effectively analysing the entire sample. An internal standard is a selected reference element of a specific concentration used by the machine to determine the mass concentration of the other trace metals. The device has an internal library containing the signals of all the elements and allowing it to multiply each with the internal value. It starts fitting each metal in the spectrum according to the library and what it has measured. Using the following formula, the instrument reports the mass concentration of each element based on internal standards.

$$\mathbf{C_i = C_{is} \times \frac{N_i}{N_{is}} \times \frac{S_{is}}{S_i}} \qquad \textbf{(Eq.3)}$$

Where:

- C_i : element concentration
- C_{is} : internal standard concentration
- N_i : element net count

- N_{is}: internal standard net count
- S_i: element sensitivity factor
- S_{is}: internal standard sensitivity factor.

3.2.4 Ions Measurement

The nutrients such as NO_3^-, NH_4^+, NO_2^-, SO_4^{2-}, and PO_4^{3-} were quantified using the ion chromatography (IC). Hence, the working principle and sample preparation steps will be described.

- **Extraction of the filtrate**

Two spots of 10 mm forming a 1.57 cm^2 area from each filter have been punched out of the samples. The punched-out samples were placed into the labelled vials, and 2 ml of 18.2 mΩ milli-Q water was added to the vials. The filter samples were shaken at 420 rpm for 120 minutes to resuspend the aerosol particles into the solution (Figure 11A). The obtained solution was then filtered through a 13 mm diameter, 0.45 µm pore size membrane filter (Pall Ion Chrom Acrodisc syringe filters, Pall Co.) to eliminate colloidal particles that could eventually block the chromatographic columns (Figure 11B).

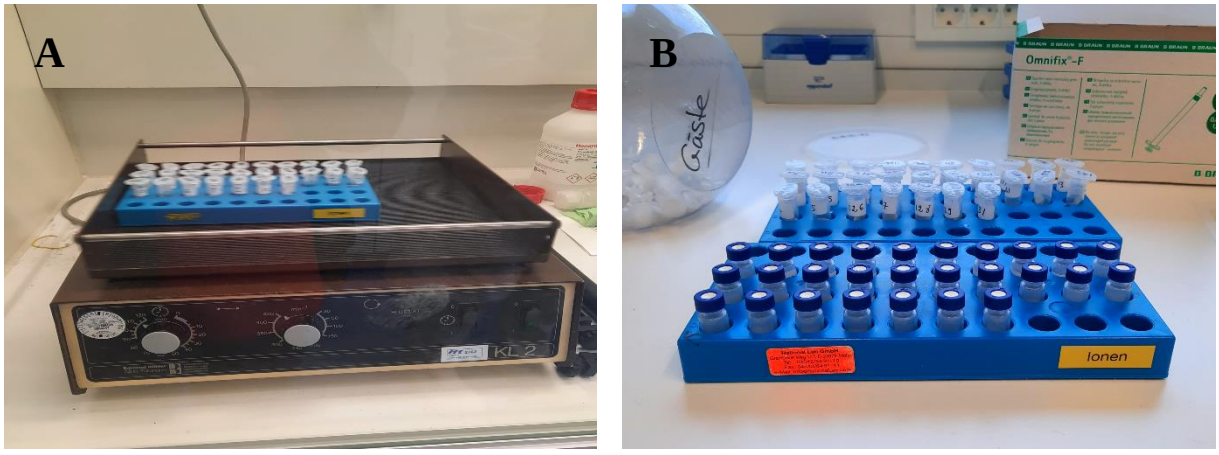

Figure 11. The preparation process of the filtrates. A) Punched samples in the milli-Q water on the shaking plate, and B) Filter extracts.

- **The analytical technique of ion chromatography**

Ion Chromatography (IC) is a technique used to separate a mixture of chemicals into its elements based on their affinity for a liquid or stationary phase. Figure 12 shows how an

IC works. The eluent (mobile phase), injector, column (stationary phase), and detector compose an IC system. The eluent is a liquid or gas that carries molecules through the IC system. In contrast, a stationary phase is a fixed material like a column or capillary tube**.** With the help of the eluent, which continuously eludes the system, the sample solution is moved into the column system. The separation of the ions in the column depends on the charge and size ratio. The ions with the slightest affinity (regarding their charge, size, and electronegativity) take the shortest time to come out, and the ions with the highest affinity take longer. Every ion takes a specific time to pass through the column and reach the detector. That time is called retention time. After the ions are separated on the analytical column, they pass through a compounding reagent or a transparent cell before they get to the detector. The ions attach to the complexing agent. A light source illuminates the complexing agent, and the molecules absorb light in the ultraviolet spectral range (190-400 nanometers). The fact that a complex with ions absorb light at a specific wavelength influences the amount of light transmitted to the detector. The detector measures the absorption of light and records it as a chromatogram for each ion. A standard curve for each ion is generated using a solution containing a known concentration of the ions to quantify the amount of each ion in the solution. In the standard curve, the concentration of each ion is linked to the absorption response through the area underneath the peak of each ion.

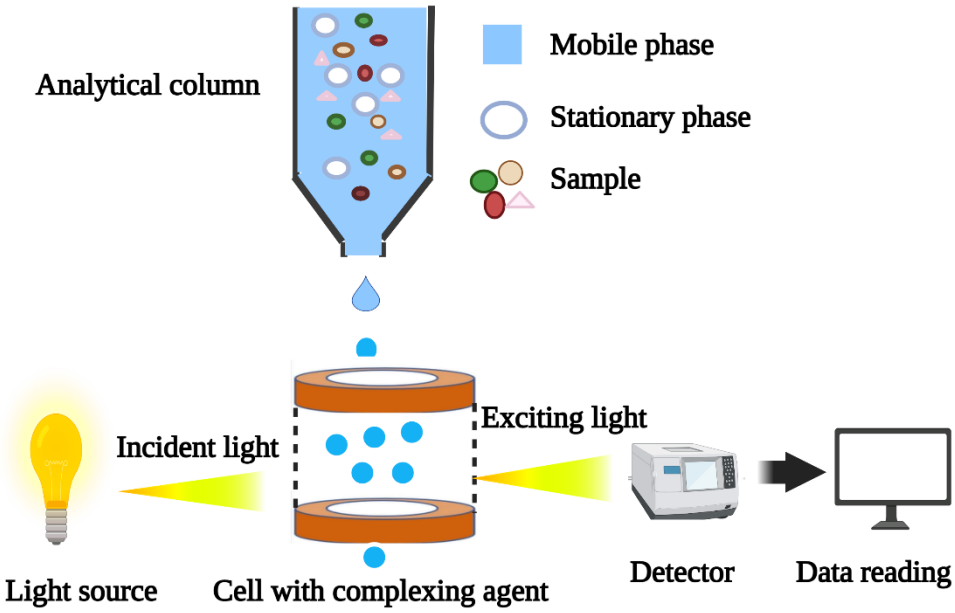

Figure 12. Schematic configuration of the Ion Chromatography (IC) showing its working principle, flow path and the different components.

- **Measurement**

The sample filtrates were analysed by ion chromatography with suppressed conductivity detection using ThermoFisher Scientific ICS-6000 dual-channel capillary ion chromatograph equipped with an eluent generator. Anions (F^-, Cl^-, NO_3^-, NO2–, SO_4^{2-} and PO_4^{3-}) were separated by capillary columns at 23°C (Dionex Ion Pac AS18 2x250 mm with guard column AG18 2 × 50 mm). The cations, NH_4^+, K^+, Na^+, Ca^{2+} and Mg^{2+} were separated using capillary columns at 40°C (Dionex Ion Pac CS16 µm 2 × 250 mm with guard column CG16 µm 2 × 50 mm) (Figure 13).

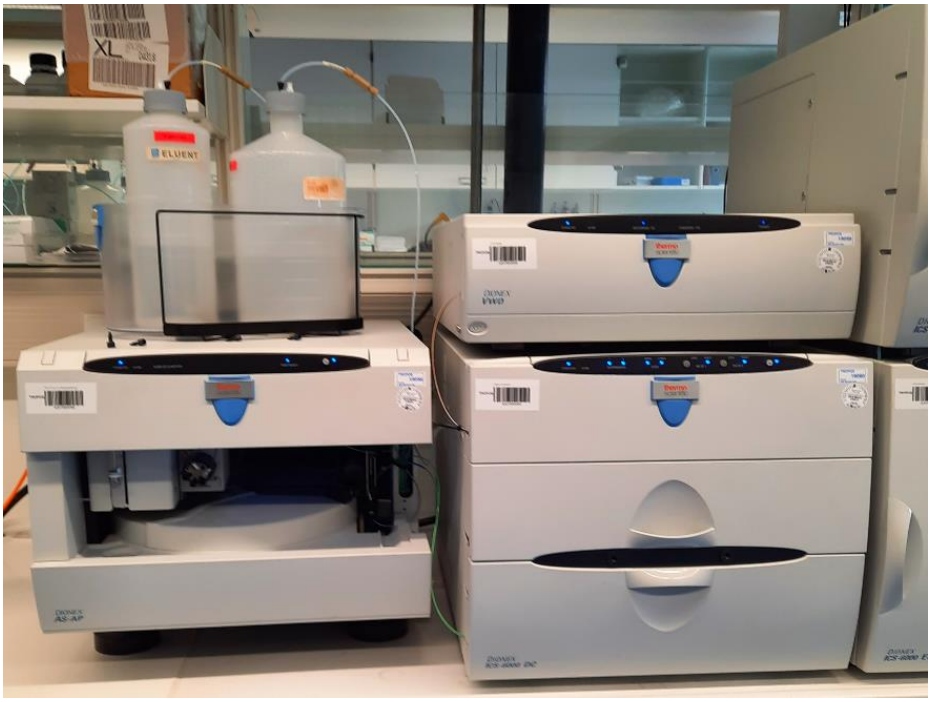

Figure 13. Ion chromatography system (Dionex ICS-6000) used for ion analysis.

3.3 Data Analysis

3.3.1 Calculation of chemical's atmospheric concentration

After obtaining the mass of each trace element from the two angle measurements using the T-STAR, the average mass concentration was calculated using the values of the two angles. And then, from the average of the two angles, the field blank sample concentration was subtracted from the sample values. After the blank subtraction, the final atmospheric concentrations were calculated according to equation 4 below. The same equation was used to calculate the atmospheric concentration of the water-soluble inorganic ions.

$$\mathbf{C_{e/i}} = \frac{\mathbf{M_c} \times \mathbf{D_f}}{\mathbf{V_a}} \times \mathbf{F_r} \qquad \textbf{(Eq.4)}$$

With:

- $\boldsymbol{C_{e/i}}$: The measured air concentration of the species (metal/ion)
- M_c: The mass of the species (metal/ion)
- D_f: The dilution factor (ratio of digesting solution volume to the sample volume)
- F_r: The filter ratio (total area covered by dust to the sub-sample area)
- V_a: The Volume of collected air (m^3)

3.3.2 Backward Trajectory Analysis

Ninety-six-hour air mass back trajectories (AMBTs) were computed from the National Oceanic and Atmospheric Administration[2] (NOAA) database using the Hybrid Single-Particle Lagrangian Integrated Trajectories (HY-SPLIT) program. The trajectories were calculated following the sample collection times at an altitude of 500 m. The model was operated with meteorological data from the Global Data Assimilation System (GDAS).

3.3.3 Dry deposition flux model

The depositional velocity (V_d) is necessary to calculate the mass deposition flux. It quantifies the speed a particle or a particle population experiences during the deposition process. The term V_d is hard to describe because it is affected by a series of physical processes, including gravitational settling, impaction, and diffusion. The dry depositional velocity is usually obtained by depositional models (Duce et al., 1991). Niedermeier (2014) developed an experimental model to determine mineral dust's dry mass deposition flux to the ocean at the CVAO based on (Zhang et al., 2001) parameterisation. The dry deposition velocity is given by the equation 5:

$$\mathbf{V_d} = \frac{\mathbf{1}}{\mathbf{R_a} + \mathbf{R_s}} + \mathbf{V_g} \qquad \textbf{(Eq.5)}$$

Where:

- R_a denotes the aerodynamic resistance
- R_s denotes surface resistance
- V_g is the gravitational settling velocity.

[2] https://www.ready.noaa.gov/HYSPLIT.php

In this study, the depositional velocity values were based on a non-linear model developed and used to calculate the dry deposition velocities for PM_{10} particles collected for each sampling date. The dry deposition velocity derived from Niedermeier (2014) is given by

$$\mathbf{V_d = 0.0042 \times U^2 - 0.015 \times U + 0.6468} \quad \textbf{(Eq.6)}$$

Where U is the wind speed (m s^{-1}).

The dry deposition flux of particulate species was calculated using the following equation:

$$\mathbf{F_d = C_a \times V_d} \quad \textbf{(Eq.7)}$$

Where:

- F_d is the dry deposition flux,
- C_a is the atmospheric concentration of particulate species,
- V_d is the dry deposition velocity.

3.3.4 Potential new production supported by dry deposition fluxes

Assuming that all dry atmospheric inputs of dissolved inorganic nitrogen (DIN) and dissolved inorganic (DIP) were effectively utilised by marine phytoplankton, the Redfield ratio (C:N:P = 106:16:1) was used to calculate the dry deposition fluxes from inorganic N and P to carbon flux. The new production (NP) was calculated as follows:

$$\mathbf{NP_{DIN} = F_{DIN} \times 6.625} \quad \textbf{(Eq.8)}$$

$$\mathbf{NP_{DIP} = F_{DIP} \times 106} \quad \textbf{(Eq.9)}$$

Where:

- NP_{DIN}: "New production" supported by atmospheric dry inorganic N flux
- NP_{DIP}: "New production" supported by atmospheric dry inorganic P flux
- F_{DIN}: atmospheric dry inorganic N deposition flux
- F_{DIP}: atmospheric dry inorganic P deposition flux

3.3.5 Satellite-derived Chlorophyll-a and primary producers' data processing

The coupling between dust aerosols and phytoplankton concentrations around CVAO waters was examined at the same timescales using Moderate Resolution Imaging

Spectrometer (MODIS) Sensor observations (January 1– March 31, 2022). The dust-induced phytoplankton response was analysed to make the time series comparable; the chlorophyll-a concentration and the different groups of phytoplankton concentration in seawater were computed with a grid 50 km x 50 km average in a rectangular area: latitude Nord (17.99, 18.22), longitude West (−23.72, −23.60) corresponding area as shown in Figure 14. The satellite data was processed with python software V.3.8 under the PyCharm interface. The following libraries were used to process the data: netCDF4, NumPy, DateTime, and pandas.

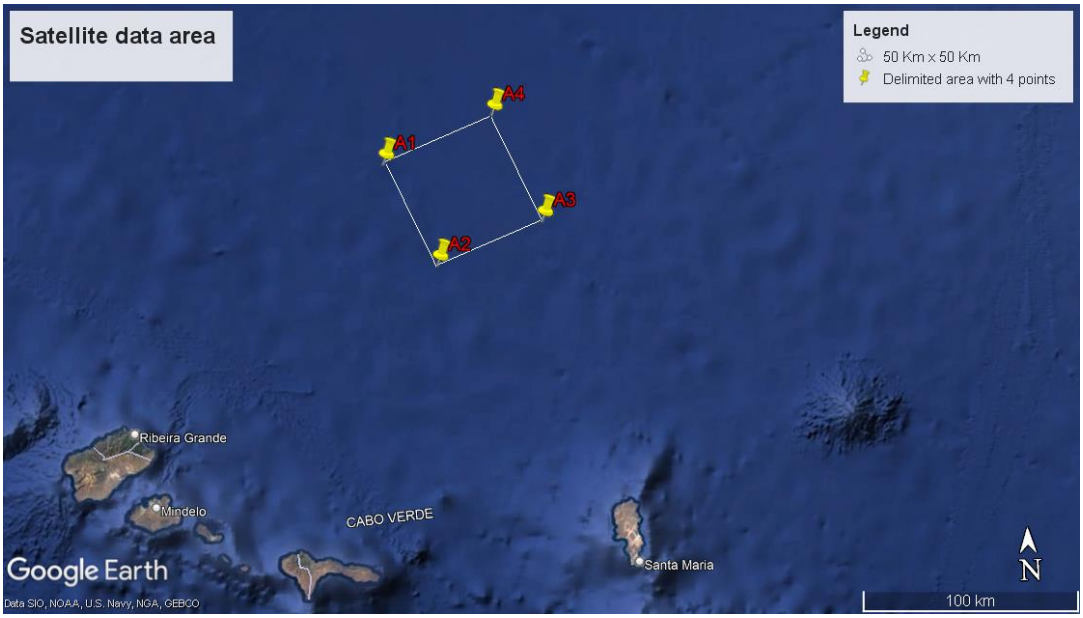

Figure 14. Selected area 50 km x 50 km for computing the Moderate Resolution Imaging Spectrometer (MODIS) Sensor observations data.

4. Results and discussion

This chapter presents the principal analysis and results obtained from the lab measurements and satellite-derived parameters. The chapter starts by giving the temporal variation of PM_{10} mass concentration, water-soluble inorganic ions (WSIIs), trace metals (TMs), and meteorological parameters during the sampling period. Then the correlation between chlorophyll and PM_{10} is shown. After, results on relationships between the Redfield ratios and deposition fluxes are shown. The chapter ends with discussion on the impacts of dust-induced nutrient inputs on the phytoplankton stoichiometry, the productivity and their diversification.

4.1 Atmospheric deposition

4.1.1 Variation of PM_{10} mass concentration during the sampling period

The measured aerosol concentrations (PM_{10}) at CVAO showed high temporal variability. In the sampling period, three dust storm episodes were observed at the CVAO. The first dust storm (DS1) lasted from January 31 to February 5, 2022, the second (DS2) lasted from February 9-11, and the third dust storm lasted from February 17-18, 2022 (Figure 15). The daily (24-hr) PM_{10} mass average and standard deviation were 67.72 ± 70.09 μg m^{-3} (Appendix A I) for the whole sampling period, which was above the limits stated in the World Health Organisation (WHO) air quality guidelines (50 μg m^{-3}). The PM_{10} mass concentrations ranged from 0.72 to 35.66 μg m^{-3}, with a mean of 16.64 ± 13.0 μg m^{-3} in the dust-free day samples. The PM_{10} mass concentration increased significantly by up to 250 μg m^{-3} in dust day samples, with a mean of 118.80 ± 66.40 μg m^{-3} corresponding to a 614% increase compared to all the non-dust days (Appendix A II). PM_{10} mass concentration was slightly larger in DS1 than in DS2 (118.86 and 84.91 μg m^{-3}, respectively) (Appendix A III). However, in DS3, it was relatively a factor of 2 of that of DS2. In each pair of dust day samples and the reference sample, a net increase in the mass concentration of PM_{10} was observed from event to event. PM_{10} increased in all three dust events but was more marked in DS1 with an increase of 3524 % in comparison to the reference sample (Appendix A IV).

PM_{10} concentrations exhibited a strong daily trend characterised by a significant increase during the dust days samples of PM_{10}. The high standard deviation values associated with the mass concentrations of PM_{10} samples and some of the analysed species are due to the

day-to-day variability of the dust storms and, hence, to the high day-to-day variability of the composition of the analysed samples. The average PM_{10} concentration at the CVAO during the twenty-two-day sampling period was relatively higher than the 1-year PM_{10} average observed by (Gama et al., 2015), studying the seasonal patterns of Saharan dust over Cabo Verde on the island of Santiago between January 2011 and January 2012. Our PM_{10} mean was about a factor of two that of Fomba et al. (2014), who reported a 5-year PM_{10} mean value of 47.19 ±55.5 $\mu g.m^{-3}$ at CVAO on Sao Vicente Island. The results were also higher than the 1-year mean (48 ± 64) reported by (Pio et al., 2014), who conducted a 1-year (2011) continuous field measurement campaign on Santiago Island, Cape Verde, as part of the CV - DUST implemented project. The mean PM_{10} value from dust day samples was about half that documented by (Kandler et al., 2011) when an intensive month-long field experiment was conducted in Praia in January 2008, integrated with the SAMUM-2 campaign and PM_{10} values of 223 $\mu g.m^{-3}$ resulted in dust events with air masses transported directly from Africa. Our results were similar to those reported for 24 h (maximum, 150 $\mu g.m^{-3}$) in the Tenerife Island (Canary Islands) (Rodríguez et al., 2011) during periods of Saharan dust advection. The PM_{10} mass was not correlated with any meteorological parameter (Appendix A VI), indicating that no significant fraction of PM_{10} mass concentration was produced locally. These two considerably higher loads of PM_{10} over a 22 days short period demonstrate the episodic nature of the vast dust storms over the CVAO, which may be due to global circulation that lifted and transported the dust of the Saharan to the Atlantic Ocean

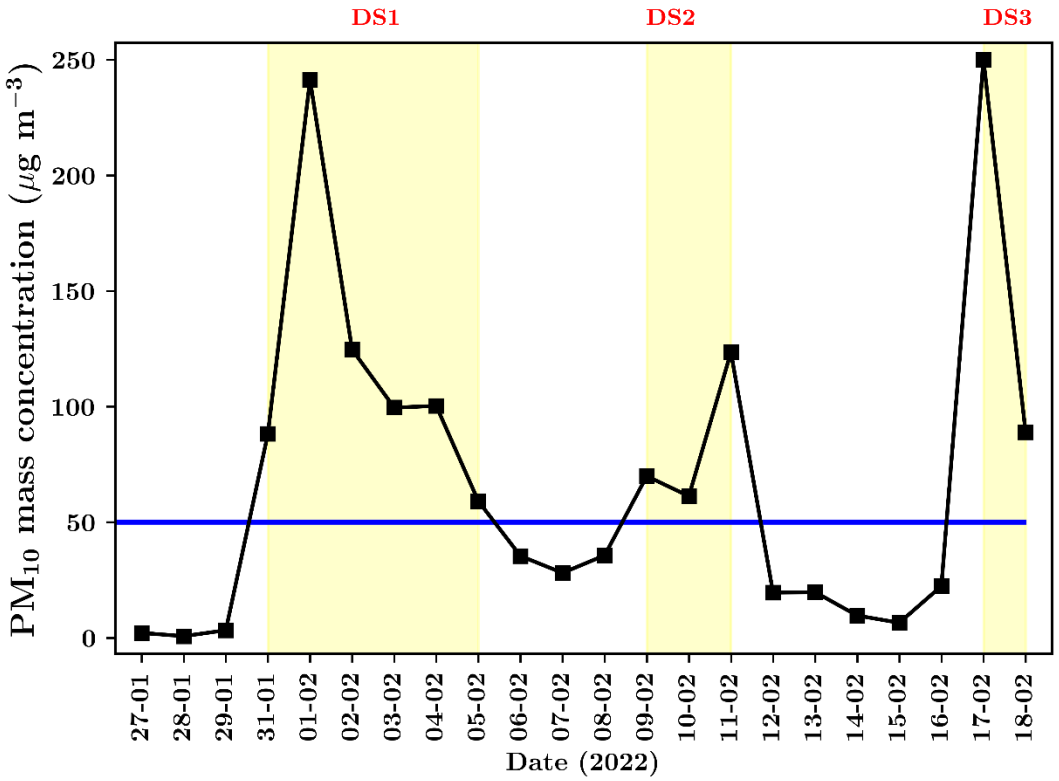

Figure 15. Temporal variability of PM_{10} mass concentrations at the CVAO site between January 27 and February 18, 2022. The blue line is the PM_{10} daily mean reference from World Health Organisation (WHO) air quality guidelines. The coloured vertical rectangles (light yellow) indicate periods of dusty day events.

4.1.2 Temporal variation of water-soluble inorganic ions (WSIIs)

Time series concentrations of WSIIs in atmospheric PM_{10} aerosols at CVAO during the sampling period are presented in Figure 16. The mean concentrations of the water-soluble inorganic ions in PM_{10} followed the order $Na^+ > SO_4^{2-} > Cl^- > NO_3^- > Ca^{2+} > K^+ > F^- > Mg^{2+} > NH_4^+ > PO_4^{3-} > NO_2^-$ during the sampling period (Appendix A I), and which showed high variation. Soluble NO_3^- and NH_4^+ were the two significant components of dissolved inorganic nitrogen (DIN) in the aerosol. Sodium, chlorides, and sulphates dominated the water-soluble inorganic ions (WSIIs). It is also worth noting that the NO_3^-, NO_2^-, F^-, Na^+ and NH_4^+ mean mass concentrations were similar in dust-free and dust-affected samples with variations of values of 59, 9, 4, 16, and 8%, respectively (Appendix A I and Appendix A II). Mg^{2+} and Ca^{2+} concentrations increased significantly during the dust storm days with values greater than 100 %. However, the increase in SO_4^{2-}, PO_4^{3-}, and K^+ concentrations was less than 100% (50, 28, and 64%, respectively) (Appendix A II).

When comparing the mean mass concentration of each water-soluble ion in each dust storm, the concentration of NO_2^-, PO_4^{3-}, PO_4^{3-}, and NH_4^+ showed no notable difference in

mean concentration between the three dust storms (as seen in Figure 16 and Appendix A III). However, the ions sulphate (SO_4^{2-}), nitrate (NO_3^-), calcium (Ca^{2+}), potassium (K^+), and magnesium (Mg^{2+}) showed distinct profiles from one dust event to another and proportionally with the PM_{10} mass concentration during the sampling period. Their shapes were closely related in each dust storm. The ionic species SO_4^{2-}, NO_3^-, Ca^{2+}, K^+, and Mg^{2+} reached their maximum one day after the dust intrusion in the three different dust events. However, significant differences were observed from one ion to another. There were significant correlations between the concentration values of some water-soluble ions from sample to sample (Appendix A V). It turned out that most water-soluble ions, including SO_4^{2-}, K^+, $Ca^{2+,}$ and Mg^2 showed significant positives correlations with NO_3^- during both the non-dust and dust events. NO_2^- and PO_4^{3-} did not correlate with any other ions during dust periods, but they showed a strong correlation with only PO_4^{3-}, and NO_3^-, NO_2^-, SO_4^{2-}, K^+ and Ca^{2+}, respectively, in non-dust period. NO_3^- did not show any correlation with NH_4^+ in the non-dust period, but showed, on the contrary, a strong positive correlation in the dust period. There was only a strong positive correlation between NH_4^+ and K^+ during the non-dust period.

The study's first objective was to analyse the relationship between dust events and the PM_{10} species' mass concentrations, including the water-soluble inorganic ions and trace metals. Our results indicated that the impact of dust on water-soluble inorganic ions varied from one species to another. In this study, SO_4^{2-}, NO_3^-, K^+, $Ca^{2+,}$ and Mg^{2+} significantly increased during the dust events. Furthermore, our results fully supported that dust events affected the species' deposition differently. We also found a slow deposition of species such as PO_4^{3-}, NO_2^- and $NH4^{+,}$ i.e., those species seemed to remain in the atmosphere after the first dust intrusion, while the depositions of the SO_4^{2-}, NO_3^-, K^+, Ca^{2+}, and Mg^{2+} were relatively quick. One must question the mechanism by which dust events may impact the concentration and the deposition of water-soluble inorganic ions. It may be simply a mix of mechanisms that could explain the evident increase of the species during the dust events (Wang et al., 2011). The formation of nitrate on dust strongly depends on the environmental conditions. Indeed, heterogeneous reactions could quickly form secondary particle components such as SO_4^{2-}, NO_3^-, and NH_4^+ from their precursors SO_2, NOx, and NH_3 on dust surfaces. Their increase could also be explained by air masses transporting them during long-distance transport. There is some evidence that high relative humidity and high temperature may promote/favour heterogeneous reactions, i.e., the formation of nitrate, sulphate, and ammonium (Wang et al., 2018). For instance, during the first dust storm DS1, the high relative humidity could lead to the secondary formation of SO_4^{2-}, NO_3^-, and NH_4^+. During

DS2, RH was at a moderately high level, enhancing the efficiency of aqueous processing on the particles (Wang et al., 2016, 2018).

Our results were consistent with many studies that reported significantly increased mass concentrations of SO_4^{2-}, NO_3^-, and NH_4^+. The increase is attributable to the long-distance transport of dust particles from emission sources or to physical mixing and the heterogeneous formation on the dust surfaces (Liu & Bei, 2016; Qi et al., 2018; Wang et al., 2018). However, previous studies also reported conflicting results that the concentration of SO_4^{2-}, NO_3^-, and NH_4^+ in atmospheric aerosols on dusty days was significantly lower during a dust episode than during a non-dust episode (Huang et al., 2010; Kang et al., 2013; Wang et al., 2011; Wu et al., 2017). They found that in dust pollution episodes, concentrations of NO_3^- and NH_4^+ were much lower, while SO_4^{2-} increased significantly. The high concentration of K^+, $Ca^{2+,}$ and Mg^{2+} can be attributed to the proximity of the study site to the sea. It could also be attributed to the combination of sea salt and the crustal elements introduced by the dust from the emission sources. This finding supports the results of other studies linking dust intrusion with the concentration of K^+, $Ca^{2+,}$ and Mg^{2+} (Fan et al., 2013; Fomba et al., 2014; Liu & Bei, 2016). During the dust episodes, the air masses travelled over the ocean. They may carry a higher amount of water vapour and SO_2 and NO_2. In this regard, the heterogeneous reactions between calcium carbonate and acidic gases can be enhanced. The enhancement could lead to a higher fraction of calcium carbonate from dust particles that could be transformed into soluble calcium (Wang et al., 2018). In some species such as K^+, $Ca^{2+,}$ and Mg^{2+}, high concentrations were attributed to the combination of crustal elements and sea salt, while the secondary species were attributed to physical mixing and heterogeneous dust formation.

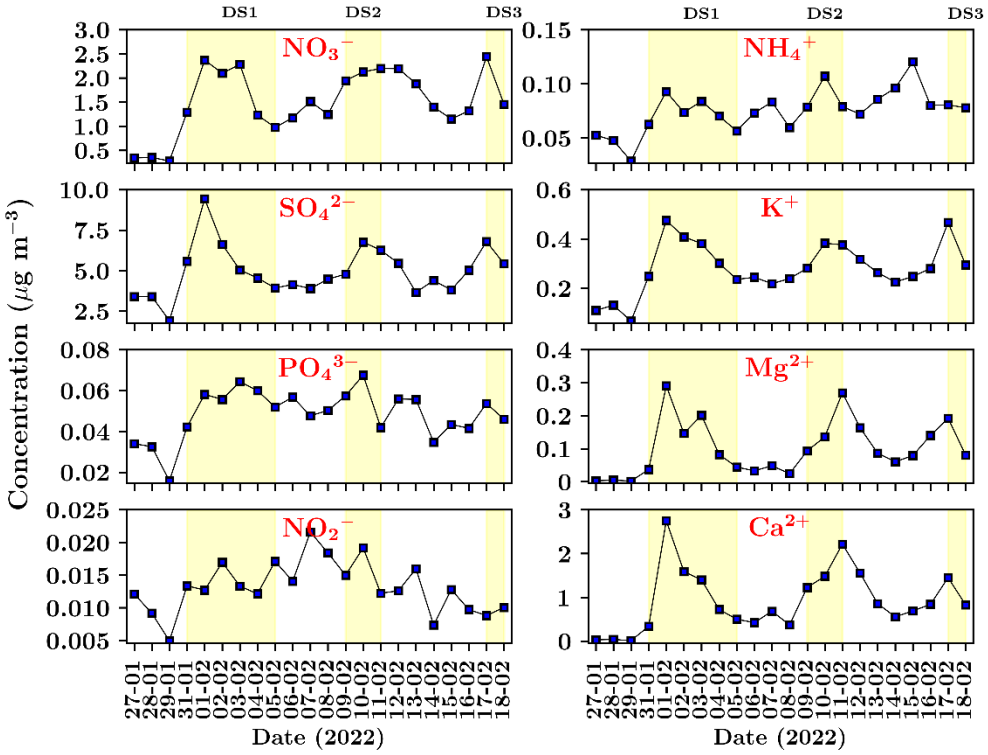

Figure 16. Temporal variation in concentrations of inorganic ions during the sampling period at CVAO.

4.1.3 Temporal variation of trace metals during the sampling period

Figure 17 shows the temporal variation of eight trace elements during the sampling period. These eight elements included three heavy metals of mainly terrigenous origin, such as aluminium (Al), iron (Fe), and titanium (Ti); two heavy metals of mainly anthropogenic origins, such as zinc (Zn) and vanadium (V) and three elements with different natural and anthropogenic sources such as phosphorus (P), nickel (Ni), and chromium (Cr). Ni, V, Cr, Fe, Al, and Ti fluctuated a lot from day to day and from one dust event to another. The average Al, Fe, and Ti concentrations in dust samples increased 2- 3 times compared to those in non-dust samples with a variation of 203, 637, and 55% (Appendix A I and Appendix A II). In contrast, there was a slightly considerable difference between dust and non-dust samples for P, V, and Zn with low values of variation of 38, 3, and 23%, respectively. The mass concentration of Fe in DS3 was a factor 2 higher than those of DS1 and DS2 (Appendix A III). As shown in Figure 17, all the terrigenous origin trace elements significantly increased during dust pollution episodes and decreased during the non-dust days. In contrast, Zn concentrations (Figure 17) increased from 0.5 μg m^{-3} (January 29, 2022) to more than a factor of two within six days of the dust event. It stayed high till February 18, 2022. Zn and Ni reached their peak concentrations (2.8 μg m^{-3} and 0.05 μg m^{-3}, respectively) on February 1

and February 2, respectively, during DS1. In contrast, the other elements peaked on February 3, 2022. Significant correlations were seen between the concentration values of some trace elements from sample to sample (correlation matrix not shown here) during the dust period. Al, Fe, and Ti were strongly correlated ($R^2 > 0.8$); while V and Zn were weakly correlated ($R^2 < 0.8$).

As mentioned above, the first objective was to analyse the relationship between dust events and the PM_{10} species' mass concentrations, including the water-soluble inorganic ions and trace metals. The findings from this study revealed that dust storms might influence the concentrations of the different trace metals. Nonetheless, the dust had a pronounced positive impact on the following elements: Al, Fe, Ni, Ti, Cr, V, and Zn, suggesting that the dust storm was a primary contributor of Al, Fe, Ni, Ti, Cr, V, and Zn. In addition, we found rapid deposition of species such as Al, Fe, Ni, Ti, Cr, and V. In contrast, the deposition of Zn was very slow. The low deposition may be because Zn is a chalcophile element with a low melting point that is easy to melt and even evaporates at high temperatures. As soon as the vaporised substances are emitted into the atmosphere, they would immediately form nuclei on aerosol particles in the atmosphere (Fan et al., 2013). Several previous studies reported a significant increase in the concentration of those elements, Al, Ti, P, Fe, Zn, Cr, and V, during dust episodes (Fan et al., 2013; Gunawardena et al., 2013; Liu & Bei, 2016; Qi et al., 2018; Wang et al., 2011). Similarly, in our study, these trace metals also increased during dust episodes, indicating the influence of dust pollution. However, Gunawardena et al. (2013) and Fan et al. (2013) found that the concentration of Ni was much lower in dust storms than in the non-dust period, which was not consistent with our results.

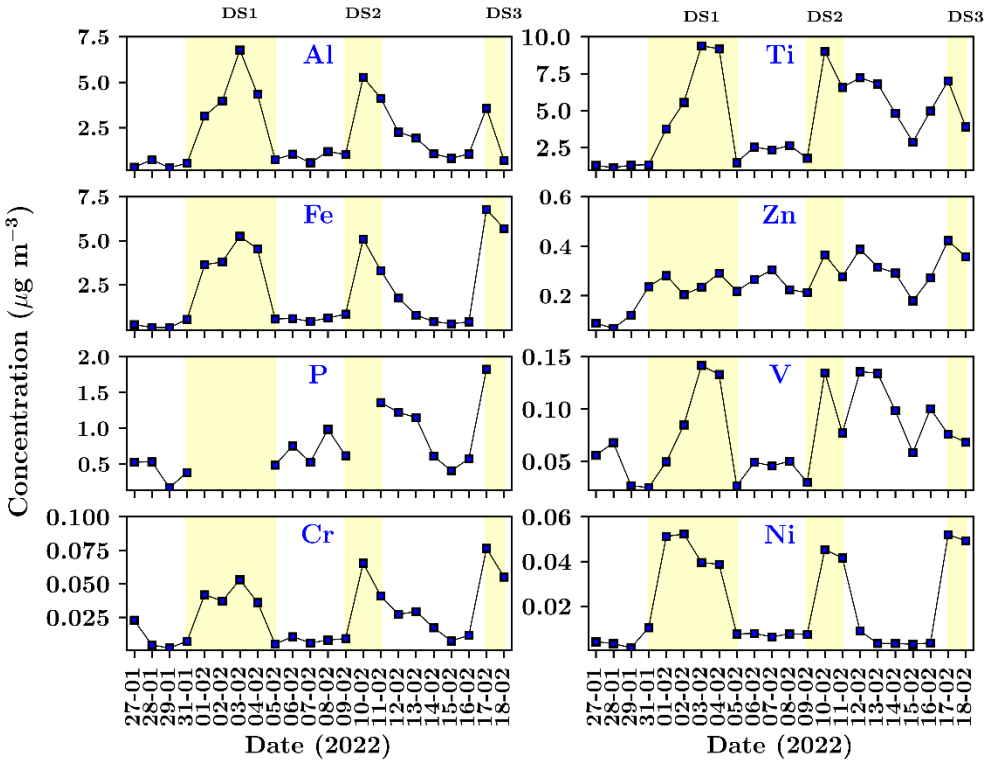

Figure 17. Temporal variation in the daily concentrations of some trace elements at CVAO during the sampling period from January 27 to February 18, 2022.

4.1.4 Variation of meteorological conditions during the sampling period

Meteorological conditions are an important driving force for atmospheric deposition at CVAO. During the sampling campaign, air temperature, air pressure, relative humidity, solar radiation, and wind speed were recorded at the CVAO site. The daily mean values of air temperature, relative humidity, pressure, and solar radiation are presented in Figure 18. The maximum temperature corresponded to the day after the first dust eruption, while the maximum relative humidity (84.5%) was observed at the beginning of the dust outbreak. The warmest day was February 6 (22.3°C), while the lowest temperature was reached on February 18 (20.8°C), indicating a clear daily pattern. However, a weak positive correlation was observed between the temperature and the relative humidity. The maximum relative humidity was recorded on the first-day dust outbreak and gradually decreased until the sixth day. The mean temperature, relative humidity, wind speed, and pressure during the dust period were 21.3 ± 0.4 °C, 79.4 ± 2.8%, 9.1 ± 1.8 m s^{-1}, 1015.9 ± 0.8 mbar, respectively. They were approximately similar to the values (21.4 ± 0.4 °C, 78.2 ± 3.8%, 8.9 ± 1.8 m s^{-1}, 1016 ± 1.3 mbar, respectively) during the dust-free period. On the other hand, mean solar radiation

increased slightly (173.4 ± 50.9 W m^{-2}) during the dusty period compared to the free dust period (149.5 ± 27.7 W m^{-2}). Solar radiation was high in the first dust outbreak and slowly declined within ten days. The pressure peaked the day before the first dust eruption. It progressively declined and peaked again the day before the last dust outbreak. SO_4^{2-}, NO_3^-, PO_4^{3-}, Ca^{2+}, K^+, Mg^{2+} and NH_4^+ showed a significant positive correlation (Appendix A VI) with relative humidity during the non-dust events while NO_3^-, NH_4^+, Ca^{2+}, and K^+ showed negative correlation with relative humidity during the dust events, indicating that relative humidity influenced the concentration of species during the dust events.

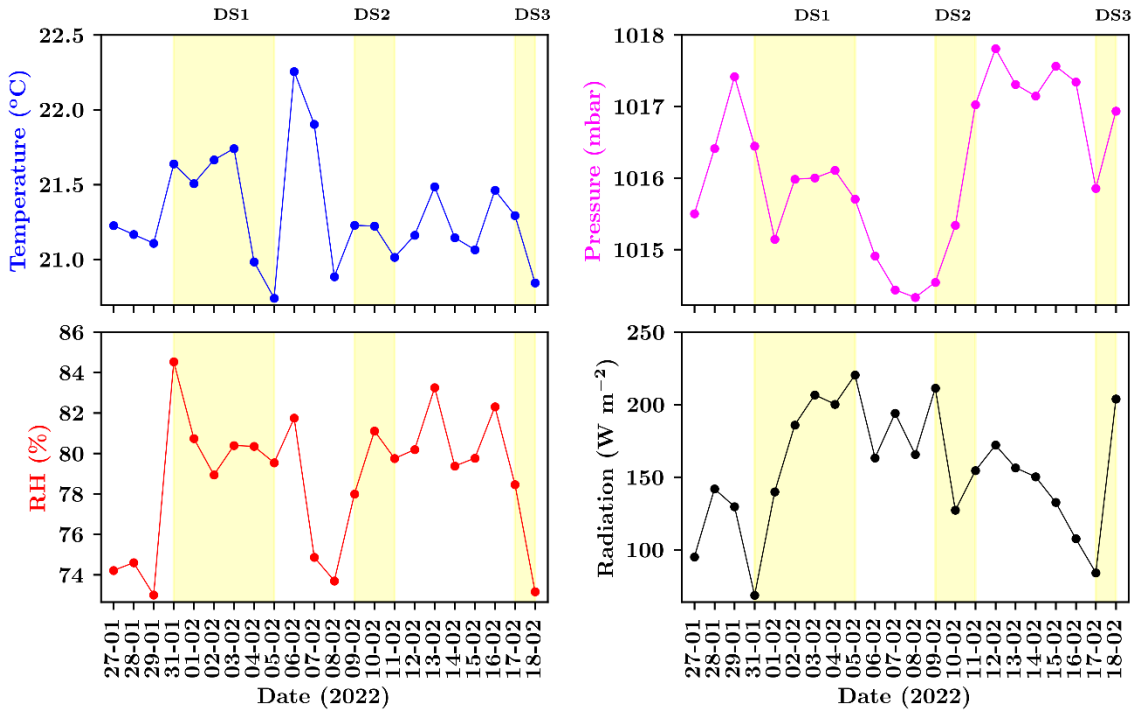

Figure 18. Temporal profiles of the daily average of temperature (upper right), pressure (upper left), relative humidity (bottom right), and radiation (bottom left) at the CVAO site during the sampling period.

4.1.5 Air mass trajectory

To analyse the source regions of PM_{10} during the three dust events, we examined 96-hour backward trajectories for dust events over the sampling period.

In the case of DS1, the trajectory showed that air masses over the CVAO region came from different areas, including the South Atlantic Ocean, the west coast of Africa and the desert regions from West African countries, Mali, Burkina Faso and Niger at elevations between 1000 and 4000 m (Figure 19a). However, in the DS2 and DS3, on the second day after the dust outbreak, the air masses travelled from western coastal Africa and the Sahara Desert regions in west Africa at low altitudes (compared to the first dust event) to the

sampling site (Figure 19b and c). They crossed the polluted cities (Dakar, Nouakchott) before reaching the sampling site. In the non-dust events, the air masses travelled from the Atlantic Ocean and the west coast of Africa. Figure 19d, e, and f showed air parcels at 500m at the CVAO during the non-dust days originating from higher altitudes 1000 m, 5000 m over the Atlantic Ocean and western desert regions from African coastal areas in North Africa.

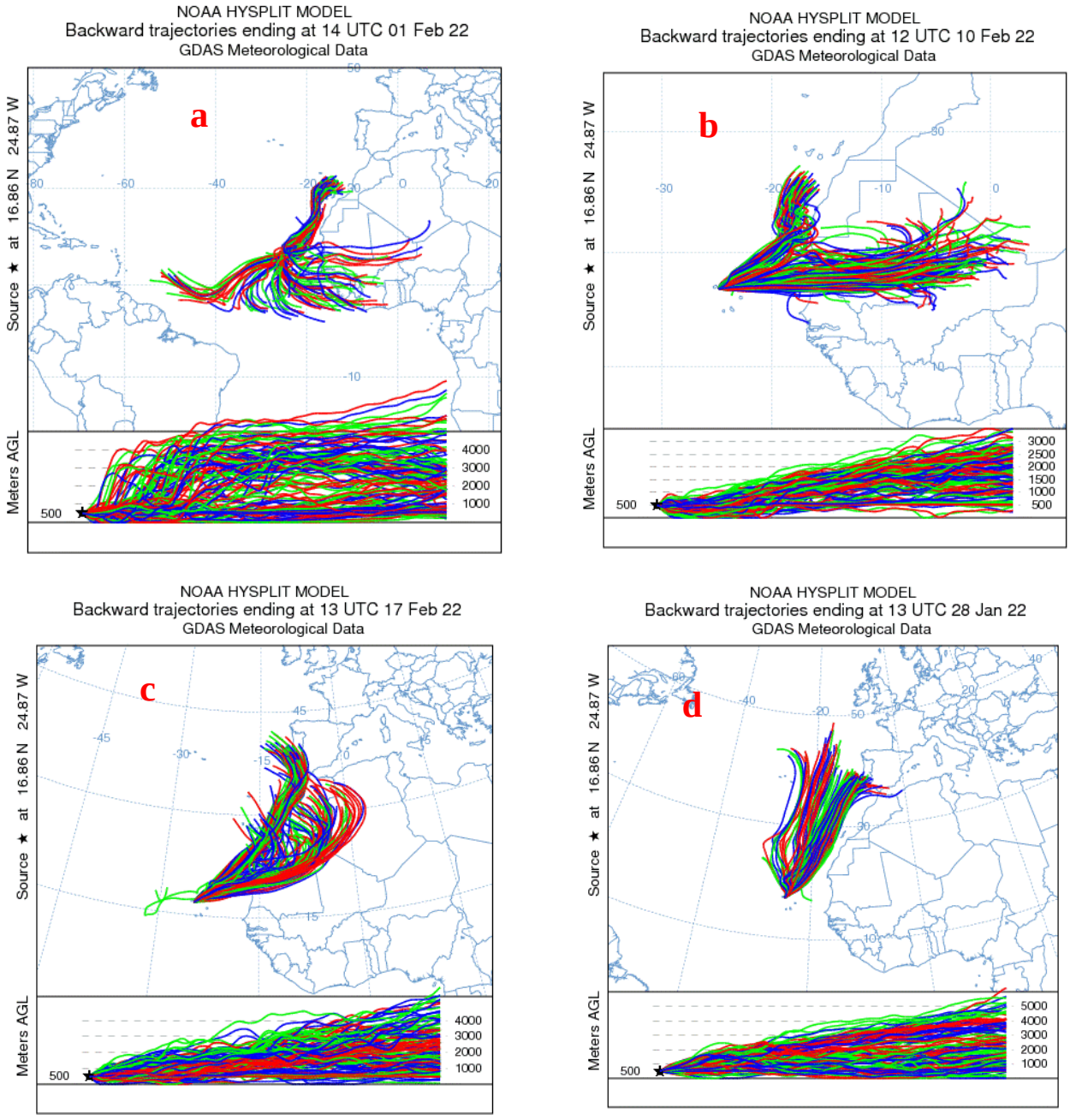

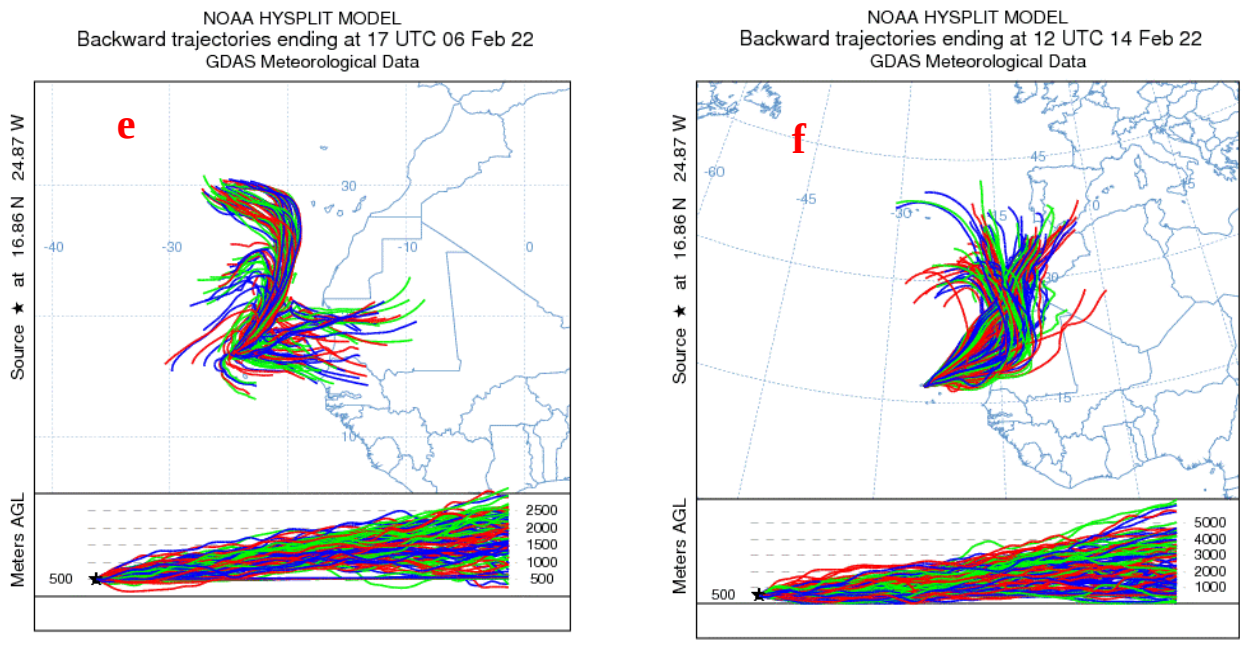

Figure 19. Representative 96 hours backward trajectories from the CVAO region, calculated at an altitude of 500 m asl, for samples collected: (a) during the DS1; (b) during the DS2; (c) during the DS3; (d) before the DS1; (e) before the DS2; (f) before the DS3. The figure was drawn with HYSPLIT: The Hybrid Single-Particle Lagrangian Integrated Trajectory. Maryland: NOAA Air Resources Laboratory

4.2 Correlation between the PM_{10}, the dust and the chlorophyll *a*

4.2.1 Temporal variation between chlorophyll *a* and PM_{10}

From Figure 20, Chl *a* concentration was found to be higher during the dust-free days (January 27-29, 2022). Due to weather conditions and the availability of the fishing boat, the Chl *a* samples were not taken on all the days, making difficult a good comparison between the particle deposition and Chl *a*. However, a significant decrease in the surface Chl *a* concentration during the dust episodes was observed. Indeed, negative correlations were observed between elements such as phosphorus (R^2 =0.85) and titanium (r^2 =0.6) with Chl *a* as shown in Figure 21, indicating that dust input may lead to a sudden decrease in the surface Chl *a* concentration. This could be due to the ballasting effect of dust deposition onto the surface waters. Ocean surface aggregates can be formed with ballast minerals and the aggregates descent into the deep waters might explain the decrease in the measured Chl *a* concentration. Our results are in line with those of van der Jagt et al. (2018) who conducted two experiments during a cruise called RV Poseidon (POS481) off Cape Blanc, Mauritania, from 15 February to 3 March 2015, to investigate how dust deposition influences aggregate formation in natural plankton communities exposed to varying amounts of added Saharan

dust. In their studies, they found that aggregates formed more quickly when exposed to Saharan dust. Also, according to Nowald et al. (2015), Saharan dust deposition only increased aggregate abundance in the deep ocean off Cape Blanc, Mauritania. Nevertheless, as discussed below, satellite remote sensing data showed that there is an increase in phytoplankton communities after a time lag of about 5 days after dust events. This suggests that the dust has an instantaneous negative effect on the surface Chl *a* concentration but subsequently a delayed positive feedback on marine bio productivity.

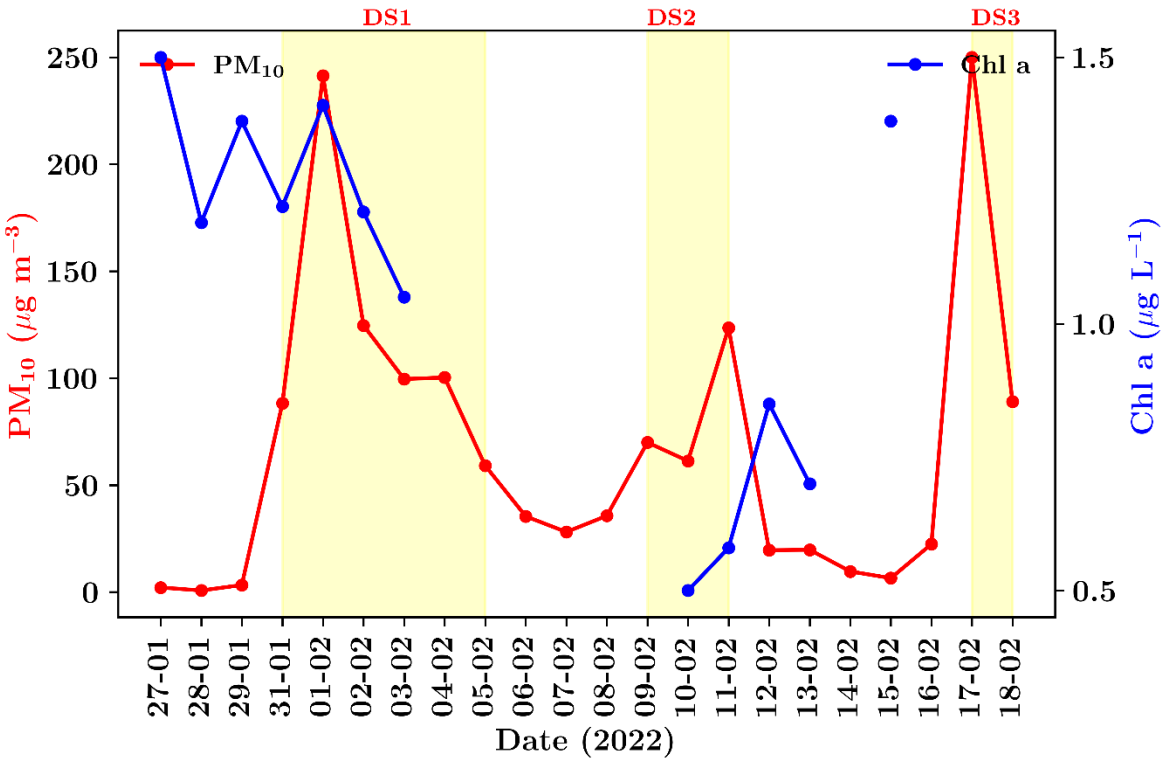

Figure 20. Temporal variation of chlorophyll *a* and PM_{10} at the CVAO site between January 27 and February 18, 2022. The coloured vertical rectangles (light yellow) indicate periods of dusty day events.

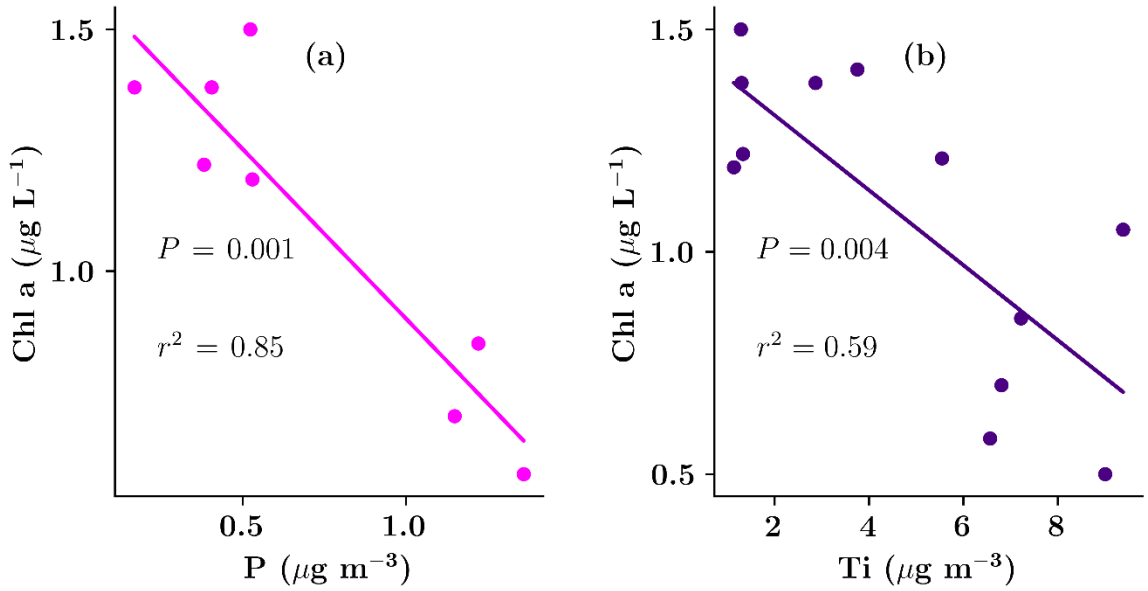

Figure 21. Correlation between the measured chlorophyll-*a* and phosphorus and titanium. Note that n=8 for phosphorus and n=12 for the titanium

4.2.2 Influence of dust on chlorophyll a and phytoplankton biomass from satellite-derived data

We analysed satellite-derived chlorophyll-*a* and phytoplankton data to investigate the biological response time to dust deposition. A total of eleven dust days were observed during the sampling period. Figure 22 represents the clearest example of a significant phytoplankton increase 5–6 days after a dust event. Note that the phytoplankton response to dust deposition differed according to their size. The picophytoplankton (0.2 – 2 μm) showed the highest response to the two dust events (0.19 and 0.23 mg m^{-3}, respectively). In contrast, the microphytoplankton (20 – 200+ μm) and nanophytoplankton (2 – 20 μm) responded similarly to the dust events. The diatoms, green algae, and dinoflagellates groups showed the lowest response to the two dusty events. The chlorophyll *a* concentration from satellite-derived data peaked on the same days as the phytoplankton (February 6, 2022, and February 22, 2022) with the same time response of 5-6 days after the dust day.

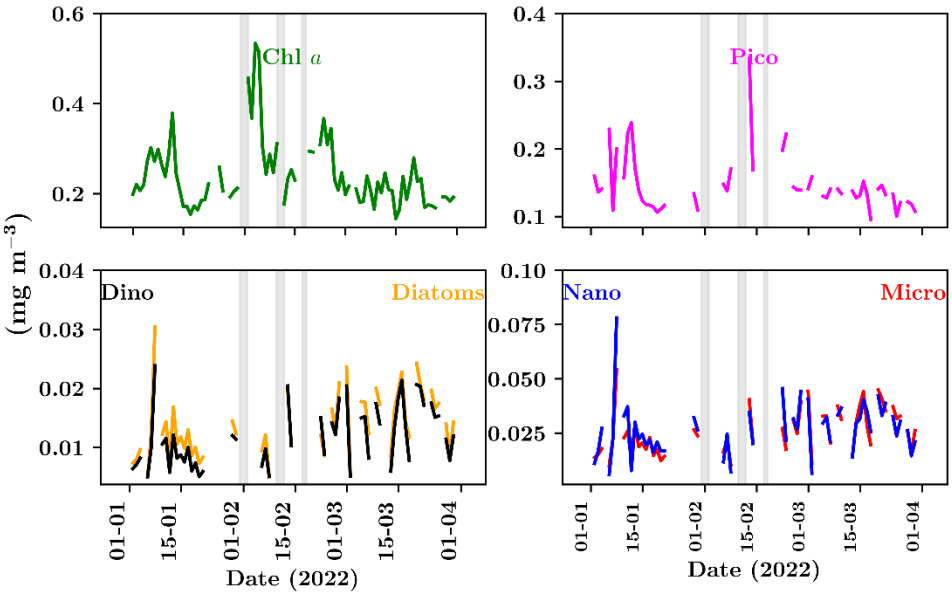

Figure 22. Temporal variabilities in the concentrations of satellite-derived different phytoplankton biomass expressed as chlorophyll in seawater and the chlorophyll concentration. The shaded vertical rectangles represent the dust storms events

4.3 Redfield ratios and deposition fluxes

The DIN/PO_4^{3-} ratio was generally above the Redfield ratio (N: P = 16: 1) throughout the sampling period, ranging from 24 to 91. The average DIN/ PO43− ratio was 55. It is worth noting that a decrease in the DIN/PO_4^{3-} also occurred on February 1 to February 5, corresponding to periods characterised by the intense dry deposition affected by the first dust episode (Figure 23). The calculated depositional velocities of nutrients are shown in Figure 24. The deposition velocities varied between 0.6 −1 mm s^{-1} with a mean value of 0.85 mm s^{-1}. The temporal variations of dry deposition fluxes of WSIIs and TMs during the sampling period are shown in Figure 25. The overview data is presented in Appendix A VII. Only dry deposition fluxes of nutrients to the Atlantic Ocean around CVAO were estimated in our study. A total of 22 daily dry deposition fluxes of N species were calculated using the depositional velocity (Vd) and mass concentrations during the sampling period. As it is seen from Appendix A VII, the PM_{10} mass flux at CVAO recorded an average of 5 mg m^{-2} d^{-1} during the sampling period. However, a remarkably high flux was recorded for dust days samples as they exhibited the most increased dust flux (9.4 ± 5.25 mg m^{-2} d^{-1}). On the contrary, the PM_{10} deposition flux in the free dust days PM_{10} samples showed a low mean value (0.075 ± 0.008 mg m^{-2} d^{-1}). The mean dry deposition flux of atmospheric DIN species at CVAO was estimated to be 2.2 µmol m^{-2} d^{-1} (Appendix A VII). Trace metals deposition supplied surface waters primarily with Al and Fe, contributing 60.3% and 27.6%,

respectively, to the deposition of eight trace metals. The calculated fluxes of water-soluble inorganic N and PO_4^{3-} showed high temporal variability and ranged between 0.5– 3.1 and 0.01 – 0.05 μmol m^{-2} d^{-1} during twelve dust-free days sampling and between 1.2 – 3.4 and 0.03 – 0.05 mmol m^{-2} d^{-1} during dust days sampling period, respectively. The mean fluxes of water-soluble ions and some trace metals PO_4^{3-}, NO_2^-, NH_4^+, K^+, Mg^{2+}, Ni, V, and Cr derived from dust-free and dusty days aerosol samples were found to be similar.

Estimated N and P ratios in the deposit were highly variable daily, even during dust storm periods. A high mean DIN/PO_4^{3-} ratio of 55, indicates that the unbalanced atmospheric N and P dry deposition can significantly alter the nutrient content in the study area. The mean ratio of 55 is slightly higher than that reported by (Duarte et al., 2006) and (Milinković et al., 2022) with 47 and 30, respectively. Our estimate of mean DIN, PO_4^{3-}, NO_3^-, and NH_4^+ fluxes in both dust and non-dust storms is about 30 times less than those of the central Adriatic (Milinković et al., 2022) but also about 30 times larger and less similar to that of the Mediterranean Sea (Kocak, 2015). Our PO_4^{3-} deposition flux during dust events was within the range found by (Seok et al., 2021). They reported a range of 0.01 to 0.05 μmol m^{-2} d^{-1} of PO_4^{3-} in the Western North Pacific Ocean. Our NO_3^- and NH_4^+ fluxes are out of the ranges (2.8 to 31.6 and 0.1 to 3.5 μmol m^{-2} d^{-1}, respectively) reported by Seok and co-workers. However, our dry mean DIN flux ranged within the values (2 to 83 μmol m^{-2} d^{-1}) reported by (Srinivas et al., 2011) in the Bay of Bengal. Myriokefalitakis et al. (2020), using a model simulating the biogeochemical cycles of carbon and the major nutrients, showed that the elemental ratio of deposited N:P drives productivity in marine regions with macronutrient limitations. Their model highlighted an excess of N compared to P, in the atmospheric deposition, which is in line with our findings. As suggested in previous studies, the north Atlantic Ocean (NAO) experienced high fluxes of DIN compared to DIP (Duarte et al., 2006; Zamora et al., 2013; Powell et al., 2015). Our NO_3^- and NH_4^+ fluxes were factor 3 and 4 lower than those reported by (Powell et al., 2015) in the North Atlantic. The estimated dry fluxes of DIN reported by (Zamora et al., 2013) at Barbados and Miami (14.8 and 37 μmol m^{-2} d^{-1}, respectively) were factors of 4 and 14, respectively higher than our DIN flux during the dust episodes.

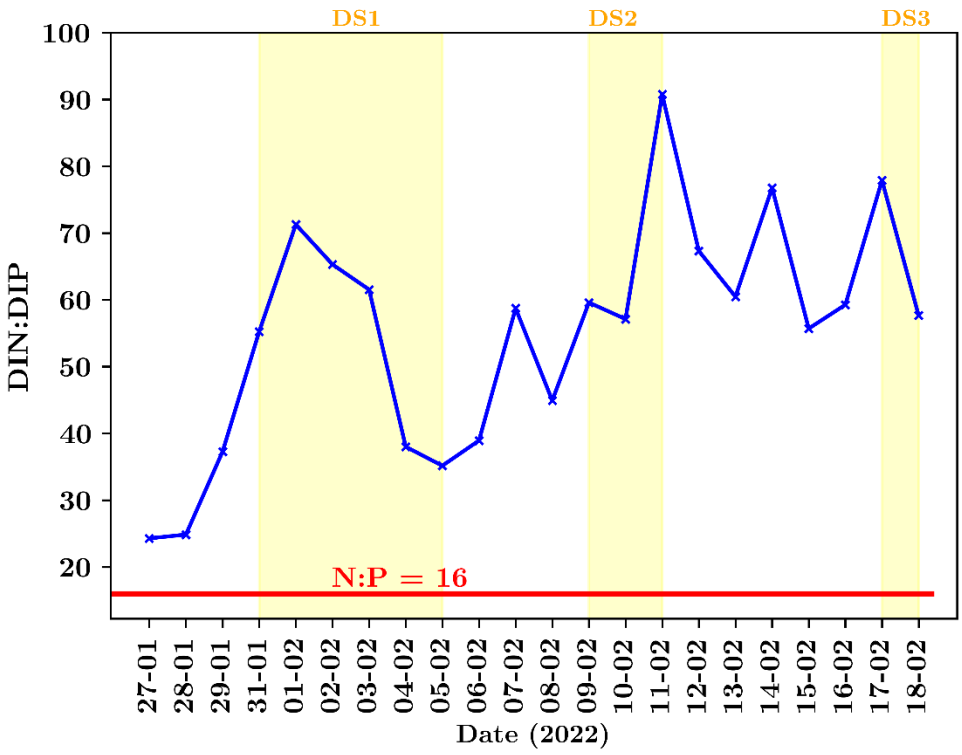

Figure 23. Temporal variabilities in the N and P ratios during the sampling period. DIN represents soluble inorganic nitrogen defined as a sum of NH_4^+, NO_3^-, and NO_2^-. DIP represents dissolved inorganic phosphate (PO_4^{3-}).

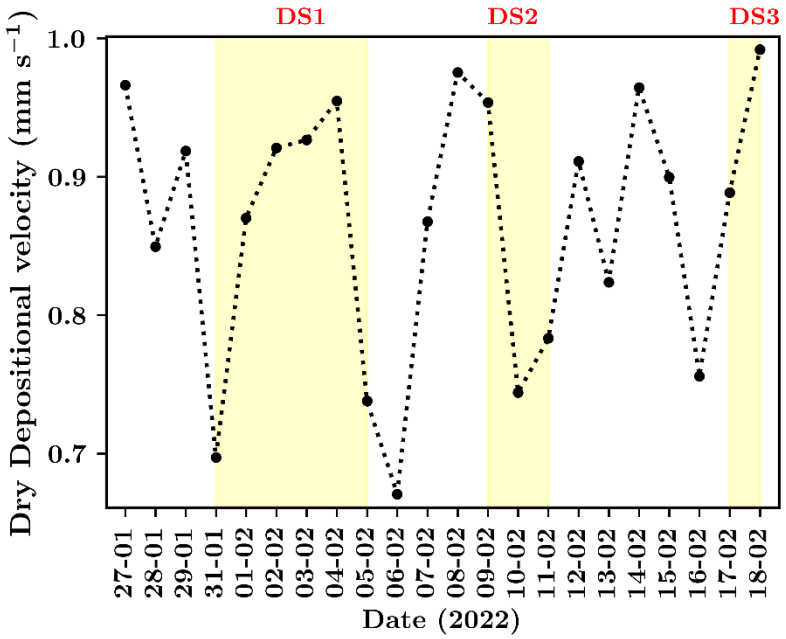

Figure 24. Temporal variation of the dry deposition velocities calculated for the PM_{10} chemical species during the sampling period of January 27 to February 18, 2022.

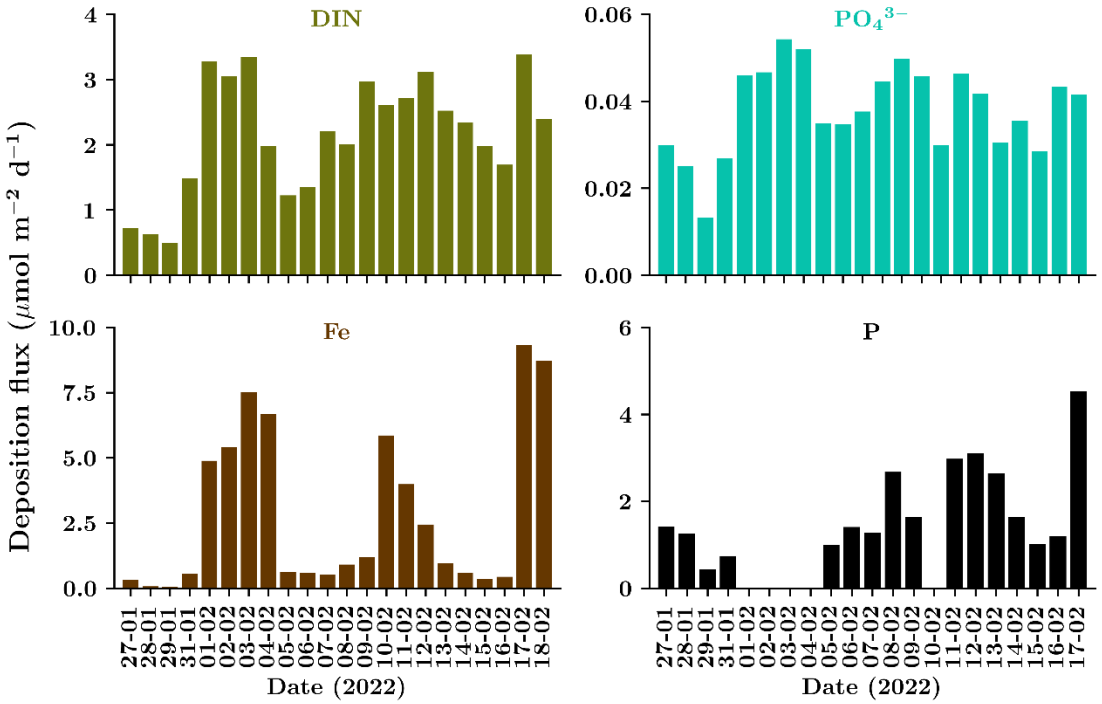

Figure 25. Temporal variation of dry deposition fluxes of DIN (= NO_3^- + NO_2^- + NH_4^+), PO_4^{3-}, Fe and P during the sampling period.

4.4 New potential production derived from the dry atmospheric N and P deposition

Many factors contribute to marine primary production, including atmospheric, riverine, and industrial inflows, as well as internal factors such as upwelling nutrients. To estimate the level of productivity that the entire atmospheric dry deposition could support, we calculated the new production based on the whole DIN deposition fluxes. As shown in Figure 26, the time series of the calculated production at CVAO significantly varied from 55.93 to 334.57 μg C m^{-2} d^{-1}. We assumed a constant molar C: N requirement of 6.625 for many plankton species (Redfield, 19). Accordingly, the total mean deposition flux of atmospheric DIN and DIP over the study area may support carbon uptake of ~220 μg C m^{-2} d^{-1} (Appendix A VIII). During the period of June 5–27, 2017, Gao et al., (2020) collected 22 aerosol samples over the South China Sea. From these samples, they estimated that atmospheric DIN deposition could potentially support 5860 μg C m^{-2} d^{-1} of new production. In comparison with our mean new production supported by DIN, their value is 34 times higher. In their study of the atmospheric dry deposition to the Gulf of Aqaba and the evaluation of the new production using the Redfield ratio of 106:16, Chen et al., (2007) estimated the dry atmospheric deposition and determined that the atmospheric deposition of DIN and DIP can contribute to

the new production in the region with a potential contribution of 3000, and 300 μg C m^{-2} d^{-1}, respectively. In comparison with their estimate, ours is quite lower than theirs. The estimated contribution to new production from atmospherically deposited nitrogen was not negligible, as atmospheric input is an important external nutrient source in the NETA region.

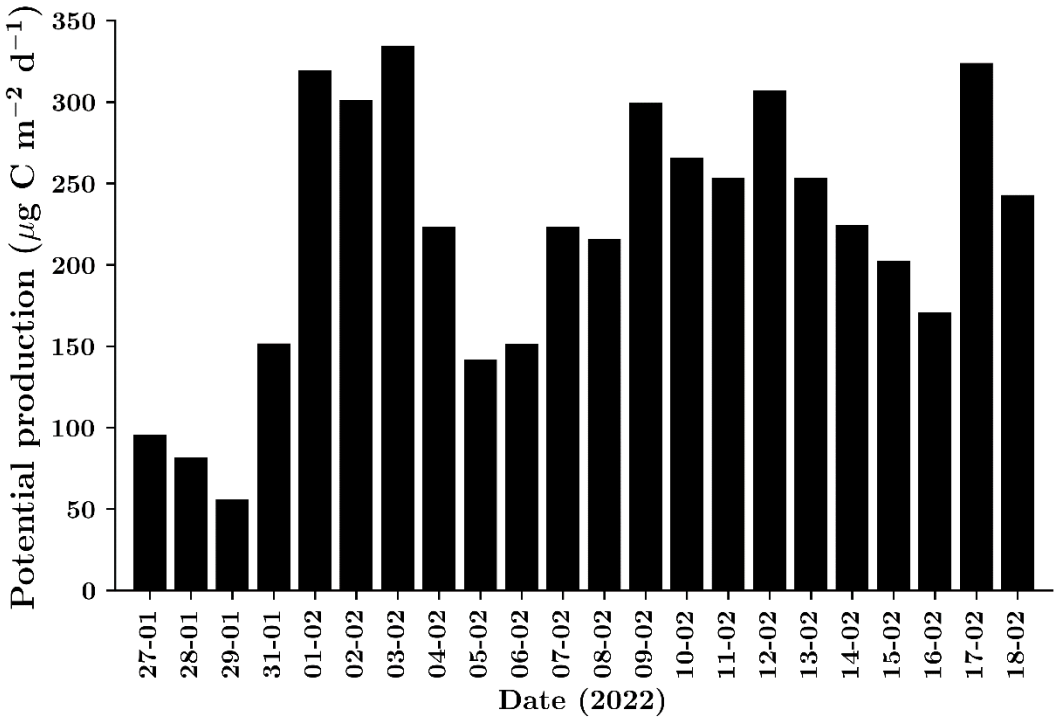

Figure 26. Temporal variations of potential production resulted from dry deposition N and P fluxes at CVAO during the sampling period in 2022.

4.5 Potential impact of dust on phytoplankton stoichiometry and growth

Results from DIN and DIP ratios indicated increases during non-dust events and the inverse during dust events, suggesting P input from dust sources. Our results regarding the fluxes showed significant fluxes of DIN, DIP, Fe during dust storms. Due to phytoplankton stoichiometry being a strong indicator of nutrient availability within a particular environment (Galbraith & Martiny, 2015) and autotrophs requiring and storing nutrients, their C:N:P ratios may be significantly affected by nutrient availability (Meunier et al., 2017). According to our results, high N:P ratios in phytoplankton might fluctuate during dust episodes due to high N:P depositions. In a recent study (Gerhard et al., 2019), phytoplankton N:P ratios were found to be higher when N concentrations were high, and lower when P concentrations were high. Sauterey & Ward, (2022) found that phytoplankton C: N stoichiometry is influenced more by the availability of nitrate below 40 º N in the North Atlantic Ocean (NAO). We could be

confident that the substantial deposition of nitrate during dust events may significantly increase the C:N ratios of phytoplankton in this region since it is dominated by small cell phytoplankton and smallest phytoplankton are known to have lower C:N (Marañón et al., 2013). The fluctuating C:N ratios of phytoplankton could impact the quality of the food web and the efficiency of the exportation of the organic matter towards the deep waters since the increased resource use efficiency is associated with higher nutrient availability (Marañón et al., 2018; Verbeek et al., 2018).

Furthermore, we believe that the large amounts of DIN that were deposited in the surrounding waters during dust outbreaks could have further increased phytoplankton growth, since nitrogen (N) is the most limiting nutrient in most oceans, including the North Atlantic (Moore et al., 2013). In oligotrophic waters such as our study region, phytoplankton are known to develop the K-strategy or affinity-adapted species defined by (Sommer, 1984), which are able to take up and assimilate growth-limiting nutrients at low concentrations. Dusty days may favour high maximum uptake rates of N and P and increase autotrophic biomass, owing to high atmospheric inputs of these nutrients. We argue that the high N:P ratio in atmospheric inputs into the NETA region might sustain P limitation.

4.6 Potential impact of dust-induced nutrient fluxes on productivity

The fifth objective of the study was to evaluate the potential new production supported by the dry deposition. As shown in Figure 26, the potential production is more pronounced during periods of dust events resulting from the high nutrient fluxes during dust days. The potential impact is supported by the satellite-derived chlorophyll *a* data. Primary production is promoted by atmospheric input of all soluble elements, including iron, nitrogen and phosphorus, in the Atlantic Ocean (Baker et al., 2003). Some studies on dust addition experiments established that metals, such as Fe, Mn, and Al, play a significant role in ocean productivity (Giovagnetti et al., 2013; Zhang et al., 2018). Also, Ridame et al. (2014) found that atmospheric dust deposition of N and P-derived ions into the surface waters enhanced chlorophyll-*a* production and nitrogen fixation. The N_2-fixers are known to have trace metals and phosphate as the main limiting nutrients (Hutchins & Fu, 2008) and we think that atmospheric deposition of both trace metal and phosphate could increase their abundance. Knowing also that Fe is required by nitrogen-fixing enzyme (nitrogenase), the high deposition of such micronutrient might enhance the N_2 fixation rate contributing to a high productivity

4.7 Impact of dust on phytoplankton diversification

The Sahara dust deposition increased the growth, composition, and abundance of phytoplankton as shown in Figure 22 from satellite data. The dust-induced effect occurred four to five days following the dust outbreak. These results are consistent with findings from a recent study on atmospheric input via satellite data (Shen et al., 2020). Moreover, from our satellite-derived results, picophytoplankton benefited more from dust deposition than nano and microplankton according to the logarithmic size classes (Sieburth et al., 1978). The most abundant plankton species in oligotrophic, nutrient-poor tropical waters are picophytoplankton (Durand et al., 2001) whereas large plankton dominate in high production waters (Marañón, 2015). We may assume, based on the dominance of picoplankton in nutrient-poor waters and their high surface area-to-volume ratio that aids in absorbing nutrients, that the bloom of picoplankton over other types of plankton resulted from the high N and P species input to the surrounding waters. It is known that Prochlorococcus and *Synechococcus* are two dominant unicellular picocyanobacterial genera in oligotrophic regions (Boyd et al., 2010). *Prochlorococcus* has a low P requirement but an efficient P utilisation while *Synechococcus* utilises all the nitrogenous components such as nitrate , nitrite , and ammonium (Moore et al., 2002). A correlation between nitrate concentration in the North Atlantic Ocean and *Synechococcus* biomass has been found by Johnson et al., (2006). Considering the environmental controls discussed above for *Prochlorococcus* and *Synechococcus,* we argue that these species have benefited more from the deposition of dust during dust storms. The significant and equal response to dust of both diatoms and dinoflagellates from satellite-derived data may reflect the fact that these species are relatively resource intensive (Irwin et al., 2012) and diatoms are more co-limited in oligotrophic water by nitrate and trace metals, especially iron (Boyd et al., 2010). Hence, the high input of nitrate and trace metals during the dust events might lead to their bloom after the short timescale of dust outbreak. Dinoflagellates are known to exhibit mixotrophy (Stoecker et al., 2017) and that could contribute to their bloom.

5. Conclusions

We investigated the impacts of dust intrusion on atmospheric PM_{10} components' concentrations and, consequently, potential effects on ocean marine productivity using aerosol samples and satellite datasets in the north-eastern Atlantic Ocean. Our findings indicate the positive influence of Saharan dust intrusion on water-soluble inorganic ions and trace metals. The marine aerosols were dominant in PM_{10} samples due to the proximity of the sampling site to the ocean. Al, Fe, V, Ni, and Cr metal species had faster deposition rates. At the same time, Zn showed a low deposition rate after each dust storm event. The satellite data revealed that Sahara dust intrusion to the NETA positively affected primary producer communities differently, with a lag time between 4 and 5 days after the dust event. Regarding the N and P species, NO_2^-, NH_4^+ and PO_4^{3-} showed the lowest deposition rate, while NO_3^-, SO_4^{2-}, K^+, Ca^{2+}, and Mg^{2+} fastly depleted in the atmosphere after a dust event. Also, the N/P ratios were well above the Redfield ratios with an excess N deposition. The picophytoplankton group was enhanced by dust more than nano and micro phytoplankton. The dry atmospheric deposition during the dust storm episodes was found to impact the N and P pool due to their significantly high depositional fluxes. However, we could not measure the nutrient variability from sea microlayer waters during the dust events. Long-term field monitoring is needed to elucidate the ecosystem responses to dust pollution.

6. References

Abadi, M. S., Owens, J. D., Liu, X., Them, T. R., Cui, X., Heavens, N. G., & Soreghan, G. S. (2020). Atmospheric dust stimulated marine primary productivity during earth's penultimate icehouse. *Geology*, *48*(3), 247–251. https://doi.org/10.1130/G46977.1

Aghnatios, C., Losno, R., & Dulac, F. (2014). A fine fraction of soil used as an aerosol analogue during the DUNE experiment: Sequential solubility in water, decreasing pH step-by-step. *Biogeosciences*, *11*(17), 4627–4633. https://doi.org/10.5194/bg-11-4627-2014

Almeida-Silva, M., Almeida, S. M., Freitas, M. C., Pio, C. A., Nunes, T., & Cardoso, J. (2013). Impact of sahara dust transport on cape verde atmospheric element particles. *Journal of Toxicology and Environmental Health - Part A: Current Issues*, *76*(4–5), 240–251. https://doi.org/10.1080/15287394.2013.757200

Baker, A. R., Kelly, S. D., Biswas, K. F., Witt, M., & Jickells, T. D. (2003). Atmospheric deposition of nutrients to the Atlantic Ocean. *Geophysical Research Letters*, *30*(24). https://doi.org/10.1029/2003GL018518

Barcelos Ramos, E. J., Schulz, K. G., Voss, M., Narciso, Á., Müller, M. N., Reis, F. V., Cachão, M., & Azevedo, E. B. (2017). Nutrient-specific responses of a phytoplankton community: A case study of the North Atlantic Gyre, Azores. *Journal of Plankton Research*, *39*(4), 744–761. https://doi.org/10.1093/plankt/fbx025

Barlow, R., Lamont, T., Britz, K., & Sessions, H. (2013). Mechanisms of phytoplankton adaptation to environmental variability in a shelf ecosystem. *Estuarine, Coastal and Shelf Science*, *133*, 45–57. https://doi.org/10.1016/j.ecss.2013.08.006

Bishop, M. L. (2020). Clinical Chemistry: Principles, Techniques, and Correlations, Enhanced Edition: Principles, Techniques, and Correlations. Jones & Bartlett Learning.

Boyd, P W, Sundby, S., & Pörtner, H.-O. (2014). Cross-chapter box on net primary production in the ocean. *Climate Change2014: Impacts, Adaptation, and Vulnerability. Part A: Global and Sectoral Aspects. Contribution of Working Group II to the Fifth Assessment Report of the Intergovernmental Panel of Climate Change*, 133–136.

Boyd, Philip W., Strzepek, R., Fu, F., & Hutchins, D. A. (2010). Environmental control of open-ocean phytoplankton groups: Now and in the future. *Limnology and Oceanography*, *55*(3), 1353–1376. https://doi.org/10.4319/lo.2010.55.3.1353

Bressac, M., Guieu, C., Doxaran, D., Bourrin, F., Desboeufs, K., Leblond, N., & Ridame, C.

(2014). Quantification of the lithogenic carbon pump following a simulated dust-deposition event in large mesocosms. *Biogeosciences*, *11*(4), 1007–1020. https://doi.org/10.5194/bg-11-1007-2014

Bressac, Matthieu, & Guieu, C. (2013). Post-depositional processes: What really happens to new atmospheric iron in the ocean's surface? *Global Biogeochemical Cycles*, *27*(3), 859–870. https://doi.org/10.1002/gbc.20076

Bristow, C. S., Hudson-Edwards, K. A., & Chappell, A. (2010). Fertilizing the Amazon and equatorial Atlantic with West African dust. *Geophysical Research Letters*, *37*(14), 3–7. https://doi.org/10.1029/2010GL043486

Bristow, L. A., Mohr, W., Ahmerkamp, S., & Kuypers, M. M. M. (2017). Nutrients that limit growth in the ocean. *Current Biology*, *27*(11), R474–R478. https://doi.org/10.1016/j.cub.2017.03.030

Carpenter, L. J., Fleming, Z. L., Read, K. A., Lee, J. D., Moller, S. J., Hopkins, J. R., Purvis, R. M., Lewis, A. C., Müller, K., Heinold, B., Herrmann, H., Fomba, K. W., Van Pinxteren, D., Müller, C., Tegen, I., Wiedensohler, A., Müller, T., Niedermeier, N., Achterberg, E. P., … Wallace, D. W. R. (2010). Seasonal characteristics of tropical marine boundary layer air measured at the cape verde atmospheric observatory. *Journal of Atmospheric Chemistry*, *67*(2), 87–140. https://doi.org/10.1007/s10874-011-9206-1

Chen, Y., Mills, S., Street, J., Golan, D., Post, A., Jacobson, M., & Paytan, A. (2007). Estimates of atmospheric dry deposition and associated input of nutrients to Gulf of Aqaba seawater. *Journal of Geophysical Research Atmospheres*, *112*(4). https://doi.org/10.1029/2006JD007858

Chiapello, I. (1997). Origins of African dust transported over the northeastern tropical Atlantic. *Journal of Geophysical Research Atmospheres*, *102*(D12), 13701–13709. https://doi.org/10.1029/97JD00259

Chien, C. T., Mackey, K. R., Dutkiewicz, S., Mahowald, N. M., Prospero, J. M., & Paytan, A. (2016). Effects of African dust deposition on phytoplankton in the western tropical Atlantic Ocean off Barbados. *Global Biogeochemical Cycles*, *30*(5), 716–734. https://doi.org/10.1002/2015GB005334.Received

Chu, Q., Liu, Y., Shi, J., Zhang, C., Gong, X., Yao, X., Guo, X., & Gao, H. (2018). Promotion Effect of Asian Dust on Phytoplankton Growth and Potential Dissolved Organic Phosphorus Utilization in the South China Sea. *Journal of Geophysical Research: Biogeosciences*, *123*(3), 1101–1116. https://doi.org/10.1002/2017JG004088

Desboeufs, K., Leblond, N., Wagener, T., Nguyen, E. B., & Guieu, C. (2014). Chemical fate

and settling of mineral dust in surface seawater after atmospheric deposition observed from dust seeding experiments in large mesocosms. *Biogeosciences*, *11*(19), 5581–5594. https://doi.org/10.5194/bg-11-5581-2014

Designs, T. (2006). *Trilogy laboratory fluorometer user's manual.* (Vol. 1).

Du, S., Ariful Islam, G. M., Xiang, R., & Yang, X. (2021). The Dust Deposition Process and Biogeochemical Impacts in the Northern South China Sea. *Asia-Pacific Journal of Atmospheric Sciences*, *57*(1), 77–87. https://doi.org/10.1007/s13143-019-00171-4

Duarte, C. M., Dachs, J., Llabrés, M., Alonso-Laita, P., Gasol, J. M., Tovar-Sánchez, A., Sañudo-Wilhemy, S., & Agustí, S. (2006). Aerosol inputs enhance new production in the subtropical northeast Atlantic. *Journal of Geophysical Research: Biogeosciences*, *111*(4), 1–8. https://doi.org/10.1029/2005JG000140

Duce, R. A., Liss, P. S., Merrill, J. T., Atlas, E. L., Buat-Menard, P., Hicks, B. B., ... & Zhou, M. (1991). The atmospheric input of trace species to the world ocean. *Global biogeochemical cycles*, *5*(3), 193-259.

Durand, M. D., Olson, R. J., & Chisholm, S. W. (2001). Phytoplankton population dynamics at the Bermuda Atlantic Time-series station in the Sargasso Sea. *Deep-Sea Research Part II: Topical Studies in Oceanography*, *48*(8–9), 1983–2003. https://doi.org/10.1016/S0967-0645(00)00166-1

Echeveste, P., Agustí, S., & Tovar-Sánchez, A. (2012). Toxic thresholds of cadmium and lead to oceanic phytoplankton: Cell size and ocean basin-dependent effects. *Environmental Toxicology and Chemistry*, *31*(8), 1887–1894. https://doi.org/10.1002/etc.1893

Eker-Develi, E., Kideys, A. E., & Tugrul, S. (2006). Role of Saharan dust on phytoplankton dynamics in the northeastern Mediterranean. *Marine Ecology Progress Series*, *314*(2001), 61–75. https://doi.org/10.3354/meps314061

Falkowski, P. G., & Raven, J. A. (2007). *Aquatic Photosynthesis*. Princeton University Press.

Fan, Q., Shen, C., Wang, X., Li, Y., Huang, W., Liang, G., Wang, S., & Huang, Z. (2013). Impact of a dust storm on characteristics of particle matter (PM) in Guangzhou, China. *Asia-Pacific Journal of Atmospheric Sciences*, *49*(1), 121–131. https://doi.org/10.1007/s13143-013-0013-2

Faria, B., & Fonseca, J. F. B. D. (2014). Investigating volcanic hazard in Cape Verde Islands through geophysical monitoring: Network description and first results. *Natural Hazards and Earth System Sciences*, *14*(2), 485–499. https://doi.org/10.5194/nhess-14-485-2014

Fernandes, M. J., Lázaro, C., Santos, A. M. P., & Oliveira, P. (2005). Oceanographic characterisation of the cape verde region using multisensor data. *European Space*

Agency, (Special Publication) ESA SP.

Fomba, K. W., Müller, K., Van Pinxteren, D., Poulain, L., Van Pinxteren, M., & Herrmann, H. (2014). Long-term chemical characterization of tropical and marine aerosols at the Cape Verde Atmospheric Observatory (CVAO) from 2007 to 2011. *Atmospheric Chemistry and Physics*, *14*(17), 8883–8904. https://doi.org/10.5194/acp-14-8883-2014

Fomba, K. wadinga, Deabji, N., El Islam Barcha, S., Ouchen, I., Mehdi Elbaramoussi, E., Cherkaoui El Moursli, R., Harnafi, M., El Hajjaji, S., Mellouki, A., & Herrmann, H. (2020). Application of TXRF in monitoring trace metals in particulate matter and cloud water. *Atmospheric Measurement Techniques*, *13*(9), 4773–4790. https://doi.org/10.5194/amt-13-4773-2020

Formenti, P., Elbert, W., Maenhaut, W., Haywood, J., & Andreae, M. O. (2003). Chemical composition of mineral dust aerosol during the Saharan Dust Experiment (SHADE) airborne campaign in the Cape Verde region, September 2000. *Journal of Geophysical Research: Atmospheres*, *108*(18). https://doi.org/10.1029/2002jd002648

Fu, W., Randerson, J., & Moore, J. K. (2015). Climate change impacts on net primary production (NPP) and export production (EP) regulated by increasing stratification and phytoplankton community structure in CMIP5 models. *Biogeosciences Discussions*, *12*(15), 12851–12897. https://doi.org/10.5194/bgd-12-12851-2015

Galbraith, E. D., & Martiny, A. C. (2015). A simple nutrient-dependence mechanism for predicting the stoichiometry of marine ecosystems. *Proceedings of the National Academy of Sciences of the United States of America*, *112*(27), 8199–8204. https://doi.org/10.1073/pnas.1423917112

Gama, C., Tchepel, O., Baldasano, J. M., Basart, S., Ferreira, J., Pio, C., Cardoso, J., & Borrego, C. (2015). Seasonal patterns of Saharan dust over Cape Verde - a combined approach using observations and modelling. *Tellus, Series B: Chemical and Physical Meteorology*, *67*(1). https://doi.org/10.3402/tellusb.v67.24410

Gao, Y., Wang, L., Guo, X., Xu, Y., & Luo, L. (2020). Atmospheric wet and dry deposition of dissolved inorganic nitrogen to the South China Sea. *Science China Earth Sciences*, *63*(9), 1339–1352. https://doi.org/10.1007/s11430-019-9612-2

Gerhard, M., Koussoroplis, A. M., Hillebrand, H., & Striebel, M. (2019). Phytoplankton community responses to temperature fluctuations under different nutrient concentrations and stoichiometry. *Ecology*, *100*(11), 1–11. https://doi.org/10.1002/ecy.2834

Giering, S. L. C., Sanders, R., Lampitt, R. S., Anderson, T. R., Tamburini, C., Boutrif, M., Zubkov, M. V., Marsay, C. M., Henson, S. A., Saw, K., Cook, K., & Mayor, D. J.

(2014). Reconciliation of the carbon budget in the ocean's twilight zone. *Nature*, *507*(7493), 480–483. https://doi.org/10.1038/nature13123

Giovagnetti, V., Brunet, C., Conversano, F., Tramontano, F., Obernosterer, I., Ridame, C., & Guieu, C. (2013). Assessing the role of dust deposition on phytoplankton ecophysiology and succession in a low-nutrient low-chlorophyll ecosystem: A mesocosm experiment in the mediterranean sea. *Biogeosciences*, *10*(5), 2973–2991. https://doi.org/10.5194/bg-10-2973-2013

Guieu, C., Dulac, F., Ridame, C., & Pondaven, P. (2014). Introduction to project DUNE, a DUst experiment in a low nutrient, low chlorophyll ecosystem. *Biogeosciences*, *11*(2), 425–442. https://doi.org/10.5194/bg-11-425-2014

Gunawardena, J., Ziyath, A. M., Bostrom, T. E., Bekessy, L. K., Ayoko, G. A., Egodawatta, P., & Goonetilleke, A. (2013). Characterisation of atmospheric deposited particles during a dust storm in urban areas of Eastern Australia. *Science of the Total Environment*, *461–462*, 72–80. https://doi.org/10.1016/j.scitotenv.2013.04.080

Guo, C., Yu, J., Ho, T. Y., Wang, L., Song, S., Kong, L., & Liu, H. (2012). Dynamics of phytoplankton community structure in the South China Sea in response to the East Asian aerosol input. *Biogeosciences*, *9*(4), 1519–1536. https://doi.org/10.5194/bg-9-1519-2012

Guo, Cui, Jing, H., Kong, L., & Liu, H. (2013). Effect of East Asian aerosol enrichment on microbial community composition in the South China Sea. *Journal of Plankton Research*, *35*(3), 485–503. https://doi.org/10.1093/plankt/fbt002

Guo, Cui, Liu, H., Yu, J., Zhang, S., & Wu, C. J. (2014). Role of microzooplankton grazing in regulating phytoplankton biomass and community structure in response to atmospheric aerosol input. *Marine Ecology Progress Series*, *507*, 69–79. https://doi.org/10.3354/meps10809

Guo, Cui, Xia, X., Pitta, P., Herut, B., Rahav, E., Berman-Frank, I., Giannakourou, A., Tsiola, A., Tsagaraki, T. M., & Liu, H. (2016). Shifts in microbial community structure and activity in the ultra-oligotrophic eastern mediterranean sea driven by the deposition of saharan dust and European Aerosols. *Frontiers in Marine Science*, *3*(SEP), 1–13. https://doi.org/10.3389/fmars.2016.00170

Hein, M., & Sand-Jensen, K. (1997). CO 2 increases oceanic primary production. *Nature*, *388*(6642), 526–527.

Henson, S. A., Yool, A., & Sanders, R. (2015). Variability in efficiency of particulate organic carbon export: A model study. *Global Biogeochemical Cycles*, *29*(1), 33–45. https://doi.org/10.1002/2014GB004965.Received

Howarth, R., Chan, F., Conley, D. J., Garnier, J., Doney, S. C., Marino, R., & Billen, G. (2011). Coupled biogeochemical cycles: Eutrophication and hypoxia in temperate estuaries and coastal marine ecosystems. *Frontiers in Ecology and the Environment*, *9*(1), 18–26. https://doi.org/10.1890/100008

Huang, K., Zhuang, G., Li, J., Wang, Q., Sun, Y., Lin, Y., & Fu, J. S. (2010). Mixing of Asian dust with pollution aerosol and the transformation of aerosol components during the dust storm over China in spring 2007. *Journal of Geophysical Research*, *115*, 1–13. https://doi.org/10.1029/2009jd013145

Hutchins, D. A., & Fu, F. X. (2008). Linking the Oceanic Biogeochemistry of Iron and Phosphorus with the Marine Nitrogen Cycle. In *Nitrogen in the Marine Environment*. https://doi.org/10.1016/B978-0-12-372522-6.00038-4

IOCCG. (2014). Phytoplankton Functional Types from Space. *Sathyendranath, S. (Ed.), Reports of the International Ocean-Colour Coordinating Group, No. 15, IO*, Dartmouth, Canada.

Irwin, A. J., Nelles, A. M., & Finkel, Z. V. (2012). Phytoplankton niches estimated from field data. *Limnology and Oceanography*, *57*(3), 787–797. https://doi.org/10.4319/lo.2012.57.3.0787

Jickells, T. D., An, Z. S., Andersen, K. K., Baker, A. R., Bergametti, C., Brooks, N., Cao, J. J., Boyd, P. W., Duce, R. A., Hunter, K. A., Kawahata, H., Kubilay, N., LaRoche, J., Liss, P. S., Mahowald, N., Prospero, J. M., Ridgwell, A. J., Tegen, I., & Torres, R. (2005). Global iron connections between desert dust, ocean biogeochemistry, and climate. *Science*, *308*(5718), 67–71. https://doi.org/10.1126/science.1105959

Jickells, T., & Moore, C. M. (2015). The Importance of Atmospheric Deposition for Ocean Productivity. *Annual Review of Ecology, Evolution, and Systematics*, *46*, 481–501. https://doi.org/10.1146/annurev-ecolsys-112414-054118

Johnson, Z. I., Zinser, E. R., Coe, A., McNulty, N. P., Woodward, E. M. S., & Chisholm, S. W. (2006). Niche partitioning among Prochlorococcus ecotypes along ocean-scale environmental gradients. *Science*, *311*(5768), 1737–1740. https://doi.org/10.1126/science.1118052

Kandler, K., Schütz, L., Jäckel, S., Lieke, K., Emmel, C., Müller-Ebert, D., Ebert, M., Scheuvens, D., Schladitz, A., Šegvić, B., Wiedensohler, A., & Weinbruch, S. (2011). Ground-based off-line aerosol measurements at Praia, Cape Verde, during the Saharan Mineral Dust Experiment: Microphysical properties and mineralogy. *Tellus, Series B: Chemical and Physical Meteorology*, *63*(4), 459–474. https://doi.org/10.1111/j.1600-

0889.2011.00546.x

Kang, E., Han, J., Lee, M., Lee, G., & Kim, J. C. (2013). Chemical characteristics of size-resolved aerosols from Asian dust and haze episode in Seoul Metropolitan City. *Atmospheric Research*, *127*, 34–46. https://doi.org/10.1016/j.atmosres.2013.02.002

Kessler, N., Armoza-Zvuloni, R., Wang, S., Basu, S., Weber, P. K., Stuart, R. K., & Shaked, Y. (2020). Selective collection of iron-rich dust particles by natural Trichodesmium colonies. *ISME Journal*, *14*(1), 91–103. https://doi.org/10.1038/s41396-019-0505-x

Kirk, J. T. (1994). Light and Photosynthesis in Aquatic Ecosystems. In *Cambridge University Press*. Cambridge university press.

Kocak, M. (2015). *Solubility of Atmospheric Nutrients over the Eastern Mediterranean : Comparison between Pure-Water and Sea-Water , Implications Regarding Marine Production*. *71*, 59–71. https://doi.org/10.4194/1303-2712-v15

Krishnamurthy, A., Moore, J. K., Mahowald, N., Luo, C., & Zender, C. S. (2010). Impacts of atmospheric nutrient inputs on marine biogeochemistry. *Journal of Geophysical Research*, *115*(G1), 1–13. https://doi.org/10.1029/2009jg001115

Liao, W. H., Yang, S. C., & Ho, T. Y. (2017). Trace metal composition of size-fractionated plankton in the Western Philippine Sea: The impact of anthropogenic aerosol deposition. *Limnology and Oceanography*, *62*(5), 2243–2259. https://doi.org/10.1002/lno.10564

Liu, Q., & Bei, Y. (2016). Impacts of crystal metal on secondary aliphatic amine aerosol formation during dust storm episodes in Beijing. *Atmospheric Environment*, *128*, 227–234. https://doi.org/10.1016/j.atmosenv.2016.01.013

Mackey, K. R. M., Buck, K. N., Casey, J. R., Cid, A., Lomas, M. W., Sohrin, Y., & Paytan, A. (2012). Phytoplankton responses to atmospheric metal deposition in the coastal and open-ocean Sargasso Sea. *Frontiers in Microbiology*, *3*(OCT), 1–15. https://doi.org/10.3389/fmicb.2012.00359

Maki, T., Ishikawa, A., Mastunaga, T., Pointing, S. B., Saito, Y., Kasai, T., Watanabe, K., Aoki, K., Horiuchi, A., Lee, K. C., Hasegawa, H., & Iwasaka, Y. (2016). Atmospheric aerosol deposition influences marine microbial communities in oligotrophic surface waters of the western Pacific Ocean. *Deep-Sea Research Part I: Oceanographic Research Papers*, *118*(October), 37–45. https://doi.org/10.1016/j.dsr.2016.10.002

Marañón, E. (2015). Cell Size as a key determinant of phytoplankton metabolism and community structure. *Annual Review of Marine Science*, *7*, 241–264. https://doi.org/10.1146/annurev-marine-010814-015955

Marañón, E., Cermeño, P., López-Sandoval, D. C., Rodríguez-Ramos, T., Sobrino, C., Huete-

Ortega, M., Blanco, J. M., & Rodríguez, J. (2013). Unimodal size scaling of phytoplankton growth and the size dependence of nutrient uptake and use. *Ecology Letters*, *16*(3), 371–379. https://doi.org/10.1111/ele.12052

Marañón, E., Fernández, A., Mouriño-Carballido, B., Martínez-García, S., Teira, E., Cermeño, P., Chouciño, P., Huete-Ortega, M., Fernández, E., Calvo-Díaz, A., Morán, X. A. G., Bode, A., Moreno-Ostos, E., Varela, M. M., Patey, M. D., & Achterberg, E. P. (2010). Degree of oligotrophy controls the response of microbial plankton to Saharan dust. *Limnology and Oceanography*, *55*(6), 2339–2352. https://doi.org/10.4319/lo.2010.55.6.2339

Marañón, E., Lorenzo, M. P., Cermeño, P., & Mouriño-Carballido, B. (2018). Nutrient limitation suppresses the temperature dependence of phytoplankton metabolic rates. *ISME Journal*, *12*(7), 1836–1845. https://doi.org/10.1038/s41396-018-0105-1

Matthew M. Mills, Celine Ridame, Margaret Davey, Julie La Roche, R. J. G. (2004). Iron and phosphorus co-limit. *Letters To Nature*, *429*(May), 292–294.

Meng, X., Chen, Y., Wang, B., Ma, Q. W., & Wang, F. J. (2016). Responses of phytoplankton community to the input of different aerosols in the East China Sea. *Geophysical Research Letters*, *43*(13), 7081–7088. https://doi.org/10.1002/2016GL069068

Meunier, C. L., Boersma, M., El-Sabaawi, R., Halvorson, H. M., Herstoff, E. M., Van de Waal, D. B., Vogt, R. J., & Litchman, E. (2017). From elements to function: Toward unifying ecological stoichiometry and trait-based ecology. *Frontiers in Environmental Science*, *5*(MAY), 1–10. https://doi.org/10.3389/fenvs.2017.00018

Milinković, A., Penezić, A., Kušan, A. C., Gluščić, V., Žužul, S., Skejić, S., Šantić, D., Godec, R., Pehnec, G., Omanović, D., Engel, A., & Frka, S. (2022). Variabilities of biochemical properties of the sea surface microlayer: Insights to the atmospheric deposition impacts. *Science of the Total Environment*, *838*(December 2021). https://doi.org/10.1016/j.scitotenv.2022.156440

Moore, C. M., Mills, M. M., Arrigo, K. R., Berman-Frank, I., Bopp, L., Boyd, P. W., ..., & Ulloa, O. (2013). Processes and patterns of oceanic nutrient limitation. *Nature Geoscience*, *6*(9), 701–710.

Moore, C. M., Mills, M. M., Arrigo, K. R., Berman-Frank, I., Bopp, L., Boyd, P. W., Galbraith, E. D., Geider, R. J., Guieu, C., Jaccard, S. L., Jickells, T. D., La Roche, J., Lenton, T. M., Mahowald, N. M., Maranon, E., Marinov, I., Moore, J. K., Nakatsuka, T., Oschlies, A., … Ulloa, O. (2013). Processes and patterns of oceanic nutrient limitation -

Supplemental Information. *Nature Geosci*.

Moore, L. R., Post, A. F., Rocap, G., & Chisholm, S. W. (2002). Utilization of different nitrogen sources by the marine cyanobacteria Prochlorococcus and Synechococcus. *Limnology and Oceanography*, *47*(4), 989–996. https://doi.org/10.4319/lo.2002.47.4.0989

Myriokefalitakis, S., Gröger, M., Hieronymus, J., & Döscher, R. (2020a). An explicit estimate of the atmospheric nutrient impact on global oceanic productivity. *Ocean Science*, *16*(5), 1183–1205. https://doi.org/10.5194/os-16-1183-2020

Myriokefalitakis, S., Gröger, M., Hieronymus, J., & Döscher, R. (2020b). An explicit estimate of the atmospheric nutrient impact on global oceanic productivity. *Ocean Science*, *16*(5), 1183–1205. https://doi.org/10.5194/os-16-1183-2020

Niedermeier, N. (2014). *Experimental determination of the mass deposition flux of mineral dust at the Cape Verde Islands.* [Doctoral dissertation, Universität Leipzig]. https://nbn-resolving.org/urn:nbn:de:bsz:15-qucosa-141260

Niedermeier, N., Held, A., Müller, T., Heinold, B., Schepanski, K., Tegen, I., Kandler, K., Ebert, M., Weinbruch, S., Read, K., Lee, J., Fomba, K. W., Müller, K., Herrmann, H., & Wiedensohler, A. (2014). Mass deposition fluxes of Saharan mineral dust to the tropical northeast Atlantic Ocean: An intercomparison of methods. *Atmospheric Chemistry and Physics*, *14*(5), 2245–2266. https://doi.org/10.5194/acp-14-2245-2014

Nowald, N., Iversen, M. H., Fischer, G., Ratmeyer, V., & Wefer, G. (2015). Time series of in-situ particle properties and sediment trap fluxes in the coastal upwelling filament off Cape Blanc, Mauritania. *Progress in Oceanography*, *137*, 1–11. https://doi.org/10.1016/j.pocean.2014.12.015

Okin, G. S., Baker, A. R., Tegen, I., Mahowald, N. M., Dentener, F. J., Duce, R. A., Galloway, J. N., Hunter, K., Kanakidou, M., Kubilay, N., Prospero, J. M., Sarin, M., Surapipith, V., Uematsu, M., & Zhu, T. (2011). Impacts of atmospheric nutrient deposition on marine productivity: Roles of nitrogen, phosphorus, and iron. *Global Biogeochemical Cycles*, *25*(2), 1–10. https://doi.org/10.1029/2010GB003858

Pan, X., Uno, I., Wang, Z., Nishizawa, T., Sugimoto, N., Yamamoto, S., Kobayashi, H., Sun, Y., Fu, P., Tang, X., & Wang, Z. (2017). Real-time observational evidence of changing Asian dust morphology with the mixing of heavy anthropogenic pollution. *Scientific Reports*, *7*(1), 1–8. https://doi.org/10.1038/s41598-017-00444-w

Pio, C. A., Cardoso, J. G., Cerqueira, M. A., Calvo, A., Nunes, T. V., Alves, C. A., Custódio, D., Almeida, S. M., & Almeida-Silva, M. (2014). Seasonal variability of aerosol

concentration and size distribution in cape verde using a continuous aerosol optical spectrometer. *Frontiers in Environmental Science*, *2*(MAY), 1–11. https://doi.org/10.3389/fenvs.2014.00015

Pitta, P., Kanakidou, M., Mihalopoulos, N., Christodoulaki, S., Dimitriou, P. D., Frangoulis, C., Giannakourou, A., Kagiorgi, M., Lagaria, A., Nikolaou, P., Papageorgiou, N., Psarra, S., Santi, I., Tsapakis, M., Tsiola, A., Violaki, K., & Petihakis, G. (2017). Saharan dust deposition effects on the microbial food web in the Eastern Mediterranean: A study based on a mesocosm experiment. *Frontiers in Marine Science*, *4*(MAY), 1–19. https://doi.org/10.3389/fmars.2017.00117

Powell, C. F., Baker, A. R., Jickells, T. D., W. Bange, H., Chance, R. J., & Yodle, C. (2015). Estimation of the atmospheric flux of nutrients and trace metals to the eastern tropical North Atlantic Ocean. *Journal of the Atmospheric Sciences*, *72*(10), 4029–4045. https://doi.org/10.1175/JAS-D-15-0011.1

Qi, J., Liu, X., Yao, X., Zhang, R., Chen, X., Lin, X., Gao, H., & Liu, R. (2018). The concentration, source and deposition flux of ammonium and nitrate in atmospheric particles during dust events at a coastal site in northern China. *Atmospheric Chemistry and Physics*, *18*(2), 571–586. https://doi.org/10.5194/acp-18-571-2018

Rahav, E., Shun-Yan, C., Cui, G., Liu, H., Tsagaraki, T. M., Giannakourou, A., Tsiola, A., Psarra, S., Lagaria, A., Mulholland, M. R., Stathopoulou, E., Paraskevi, P., Herut, B., & Berman-Frank, I. (2016). Evaluating the impact of atmospheric depositions on springtime dinitrogen fixation in the cretan sea (Eastern Mediterranean)-A mesocosm approach. *Frontiers in Marine Science*, *3*(SEP), 1–13. https://doi.org/10.3389/fmars.2016.00180

Ramalho, R. A. S. (2011). Building the Cape Verde Islands. In *Building the Cape Verde Islands*. https://doi.org/10.1007/978-3-642-19103-9

Ramessur, R. T., Boodhoo, K., Balgobin, J., Povinec, P., & Burnett, W. (2011). Dissolved Nutrients from Submarine Groundwater in Flic en Flac Lagoon, Mauritius. *Western Indian Ocean Journal of Marine Science*, *10*(2), 121–127.

Redfield, A. C. (1963). The influence of organisms on the composition of sea water. *The Sea*, *2*, 26–77.

Reich, H. G., Rodriguez, I. B., LaJeunesse, T. C., & Ho, T. Y. (2020). Endosymbiotic dinoflagellates pump iron: differences in iron and other trace metal needs among the Symbiodiniaceae. *Coral Reefs*, *39*(4), 915–927. https://doi.org/10.1007/s00338-020-01911-z

Ridame, C., Dekaezemacker, J., Guieu, C., Bonnet, S., L'Helguen, S., & Malien, F. (2014a). Contrasted Saharan dust events in LNLC environments: Impact on nutrient dynamics and primary production. *Biogeosciences*, *11*(17), 4783–4800. https://doi.org/10.5194/bg-11-4783-2014

Ridame, C., Dekaezemacker, J., Guieu, C., Bonnet, S., L'Helguen, S., & Malien, F. (2014b). Phytoplanktonic response to contrasted Saharan dust deposition events during mesocosm experiments in LNLC environment. *Biogeosciences Discussions*, *11*, 753–796. https://doi.org/10.5194/bgd-11-753-2014

Ridame, Céline, Dekaezemacker, J., Guieu, C., Bonnet, S., Ridame, C., Dekaezemacker, J., Guieu, C., Bonnet, S., & Helguen, S. (2014). Phytoplanktonic response to contrasted Saharan dust deposition events during mesocosm experiments in LNLC environment. *Biogeosciences Discussions*, *11*(1), 753–796. https://doi.org/10.5194/bgd-11-753-2014

Ridame, Céline, Dinasquet, J., Hallstrøm, S., Bigeard, E., Riemann, L., Van Wambeke, F., Bressac, M., Pulido-Villena, E., Taillandier, V., Gazeau, F., Tovar-Sanchez, A., Baudoux, A. C., & Guieu, C. (2022). N2 fixation in the Mediterranean Sea related to the composition of the diazotrophic community and impact of dust under present and future environmental conditions. *Biogeosciences*, *19*(2), 415–435. https://doi.org/10.5194/bg-19-415-2022

Robinson, A., Bouman, H. A., Tilstone, G. H., & Sathyendranath, S. (2018). High photosynthetic rates associated with pico and nanophytoplankton communities and high stratification index in the North West Atlantic. *Continental Shelf Research*, *171*, 126–139. https://doi.org/10.1016/j.csr.2018.10.010

Rodríguez, S., Alastuey, A., Alonso-Pérez, S., Querol, X., Cuevas, E., Abreu-Afonso, J., Viana, M., Pérez, N., Pandolfi, M., & De La Rosa, J. (2011). Transport of desert dust mixed with North African industrial pollutants in the subtropical Saharan Air Layer. *Atmospheric Chemistry and Physics*, *11*(13), 6663–6685. https://doi.org/10.5194/acp-11-6663-2011

Sauterey, B., & Ward, B. A. (2022). Environmental control of marine phytoplankton stoichiometry in the North Atlantic Ocean. *Proceedings of the National Academy of Sciences of the United States of America*, *119*(1), 1–6. https://doi.org/10.1073/pnas.2114602118

Schulhof, M. A., Shurin, J. B., Declerck, S. A. J., & Van de Waal, D. B. (2019). Phytoplankton growth and stoichiometric responses to warming, nutrient addition and grazing depend on lake productivity and cell size. *Global Change Biology*, *25*(8), 2751–

2762. https://doi.org/10.1111/gcb.14660

Seok, M. W., Kim, D., Park, G. H., Lee, K., Kim, T. H., Jung, J., Kim, K., Park, K. T., Kim, Y. H., Mo, A., Park, S., Ko, Y. H., Kang, J., Kim, H., & Kim, T. W. (2021). Atmospheric deposition of inorganic nutrients to the Western North Pacific Ocean. *Science of the Total Environment*, *793*, 148401. https://doi.org/10.1016/j.scitotenv.2021.148401

Shen, C., Zhao, H., Chen, F., & Xiao, H. (2020). The Distribution of Aerosols and Their Impacts on Chlorophyll-a Distribution in the South China Sea. *Journal of Geophysical Research: Biogeosciences*, *125*(6), 0–3. https://doi.org/10.1029/2019JG005490

Sieburth, J. M. N., Smetacek, V., & Lenz, J. (1978). Pelagic ecosystem structure: Heterotrophic compartments of the plankton and their relationship to plankton size fractions. *Limnology and Oceanography*, *23*(6), 1256–1263. https://doi.org/10.4319/lo.1978.23.6.1256

Sommer, U. (1984). The paradox of the plankton: Fluctuations of phosphorus availability maintain diversity of phytoplankton in flow-through cultures. *Limnology and Oceanography*, *29*(3), 633–636. https://doi.org/10.4319/lo.1984.29.3.0633

Srinivas, B., Sarin, M. M., & Sarma, V. V. S. S. (2011). Atmospheric dry deposition of inorganic and organic nitrogen to the Bay of Bengal: Impact of continental outflow. *Marine Chemistry*, *127*(1–4), 170–179. https://doi.org/10.1016/j.marchem.2011.09.002

Stoecker, D. K., Hansen, P. J., Caron, D. A., & Mitra, A. (2017). Mixotrophy in the Marine Plankton. *Annual Review of Marine Science*, *9*(1), 311–335. https://doi.org/10.1146/annurev-marine-010816-060617

Strickland, J. D. H., & Parsons, T. R. (1972). A practical handbook of seawater analysis. *The Journal of Higher Education*.

Tagliabue, A., & Völker, C. (2011). Towards accounting for dissolved iron speciation in global ocean models. *Biogeosciences*, *8*(10), 3025–3039. https://doi.org/10.5194/bg-8-3025-2011

Tyrrell T. (1999). The relative influences of nitrogen and phosphorus on oceanic primary production. *Nature*, *400*, 525–531.

Van De Waal, D. B., Verschoor, A. M., Verspagen, J. M. H., Van Donk, E., & Huisman, J. (2010). Climate-driven changes in the ecological stoichiometry of aquatic ecosystems. *Frontiers in Ecology and the Environment*, *8*(3), 145–152. https://doi.org/10.1890/080178

van der Jagt, H., Friese, C., Stuut, J. B. W., Fischer, G., & Iversen, M. H. (2018). The

ballasting effect of Saharan dust deposition on aggregate dynamics and carbon export: Aggregation, settling, and scavenging potential of marine snow. *Limnology and Oceanography*, *63*(3), 1386–1394. https://doi.org/10.1002/lno.10779

Verbeek, L., Gall, A., Hillebrand, H., & Striebel, M. (2018). Warming and oligotrophication cause shifts in freshwater phytoplankton communities. *Global Change Biology*, *24*(10), 4532–4543. https://doi.org/10.1111/gcb.14337

von Holdt, J. R. C., Eckardt, F. D., Baddock, M. C., & Wiggs, G. F. S. (2019). Assessing Landscape Dust Emission Potential Using Combined Ground-Based Measurements and Remote Sensing Data. *Journal of Geophysical Research: Earth Surface*, *124*(5), 1080–1098. https://doi.org/10.1029/2018JF004713

Wang, F. J., Chen, Y., Guo, Z. G., Gao, H. W., Mackey, K. R., Yao, X. H., Zhuang, G. S., & Paytan, A. (2017). Combined effects of iron and copper from atmospheric dry deposition on ocean productivity. *Geophysical Research Letters*, *44*(5), 2546–2555. https://doi.org/10.1002/2016GL072349

Wang, L., Du, H., Chen, J., Zhang, M., Huang, X., Tan, H., Kong, L., & Geng, F. (2013). Consecutive transport of anthropogenic air masses and dust storm plume: Two case events at Shanghai, China. *Atmospheric Research*, *127*, 22–33. https://doi.org/10.1016/j.atmosres.2013.02.011

Wang, Q., Dong, X., Fu, J. S., Xu, J., Deng, C., Jiang, Y., Fu, Q., Lin, Y., Huang, K., & Zhuang, G. (2018). Environmentally dependent dust chemistry of a super Asian dust storm in March 2010: Observation and simulation. *Atmospheric Chemistry and Physics*, *18*(5), 3505–3521. https://doi.org/10.5194/acp-18-3505-2018

Wang, Q., Zhuang, G., Huang, K., Liu, T., Lin, Y., Deng, C., Fu, Q., Fu, J. S., Chen, J., Zhang, W., & Yiming, M. (2016). Evolution of particulate sulfate and nitrate along the Asian dust pathway: Secondary transformation and primary pollutants via long-range transport. *Atmospheric Research*, *169*(X), 86–95. https://doi.org/10.1016/j.atmosres.2015.09.013

Wang, Q., Zhuang, G., Li, J., Huang, K., Zhang, R., Jiang, Y., Lin, Y., & Fu, J. S. (2011). Mixing of dust with pollution on the transport path of Asian dust-Revealed from the aerosol over Yulin, the north edge of Loess Plateau. *Science of the Total Environment*, *409*(3), 573–581. https://doi.org/10.1016/j.scitotenv.2010.10.032

Wang, S., Koedooder, C., Zhang, F., Kessler, N., Eichner, M., Shi, D., & Shaked, Y. (2022). Colonies of the marine cyanobacterium Trichodesmium optimize dust utilization by selective collection and retention of nutrient-rich particles. *IScience*, *25*(1), 103587.

https://doi.org/10.1016/j.isci.2021.103587

Wang, Z., Pan, X., Uno, I., Li, J., Wang, Z., Chen, X., Fu, P., Yang, T., Kobayashi, H., Shimizu, A., Sugimoto, N., & Yamamoto, S. (2017). Significant impacts of heterogeneous reactions on the chemical composition and mixing state of dust particles: A case study during dust events over northern China. *Atmospheric Environment*, *159*, 83–91. https://doi.org/10.1016/j.atmosenv.2017.03.044

Ward, B. A., Dutkiewicz, S., Moore, C. M., & Follows, M. J. (2013). Iron, phosphorus, and nitrogen supply ratios define the biogeography of nitrogen fixation. *Limnology and Oceanography*, *58*(6), 2059–2075. https://doi.org/10.4319/lo.2013.58.6.2059

Wen, Z., Browning, T. J., Cai, Y., Dai, R., Zhang, R., Du, C., Jiang, R., Lin, W., Liu, X., Cao, Z., Hong, H., Dai, M., & Shi, D. (2022). Nutrient regulation of biological nitrogen fixation across the tropical western North Pacific. *Science Advances*, *8*(5), 1–11. https://doi.org/10.1126/sciadv.abl7564

Wu, F., Zhang, D., Cao, J., Guo, X., Xia, Y., Zhang, T., Lu, H., & Cheng, Y. (2017). Limited production of sulfate and nitrate on front-Associated dust storm particles moving from desert to distant populated areas in northwestern China. *Atmospheric Chemistry and Physics*, *17*(23), 14473–14484. https://doi.org/10.5194/acp-17-14473-2017

Wuttig, K., Wagener, T., Bressac, M., Dammshäuser, A., Streu, P., Guieu, C., & Croot, P. L. (2013). Impacts of dust deposition on dissolved trace metal concentrations (Mn, Al and Fe) during a mesocosm experiment. *Biogeosciences*, *10*(4), 2583–2600. https://doi.org/10.5194/bg-10-2583-2013

Xing, J., Song, J., Yuan, H., Wang, Q., Li, X., Li, N., & & Qu, B. (2018). Water-soluble nitrogen and phosphorus in aerosols and dry deposition in Jiaozhou Bay, North China: Deposition velocities, origins and biogeochemical implication. *Atmospheric Research*, *207*(7), 90–99.

Zamora, L. M., Landolfi, A., Oschlies, A., Hansell, D. A., Dietze, H., & Dentener, F. (2010). Atmospheric deposition of nutrients and excess N formation in the North Atlantic. *Biogeosciences*, *7*(2), 777–793. https://doi.org/10.5194/bg-7-777-2010

Zamora, L. M., Prospero, J. M., Hansell, D. A., & Trapp, J. M. (2013). Atmospheric P deposition to the subtropical North Atlantic: Sources, properties, and relationship to N deposition. *Journal of Geophysical Research Atmospheres*, *118*(3), 1546–1562. https://doi.org/10.1002/jgrd.50187

Zhang, C., Gao, H., Yao, X., Shi, Z., Shi, J., Yu, Y., Meng, L., & Guo, X. (2018). Phytoplankton growth response to Asian dust addition in the northwest Pacific Ocean

versus the Yellow Sea. *Biogeosciences*, *15*(3), 749–765. https://doi.org/10.5194/bg-15-749-2018

Zhang, C., He, J., Yao, X., Mu, Y., Guo, X., Ding, X., Yu, Y., Shi, J., & Gao, H. (2020). Dynamics of phytoplankton and nutrient uptake following dust additions in the northwest Pacific. *Science of the Total Environment*, *739*, 139999. https://doi.org/10.1016/j.scitotenv.2020.139999

Zhang, L., Gong, S., Padro, J., & Barrie, L. (2001). A size-segregated particle dry deposition scheme for an atmospheric aerosol module. *Atmospheric Environment*, *35*(3), 549–560. https://doi.org/10.1016/S1352-2310(00)00326-5

Zhang, W., Zhuang, G., Huang, K., Li, J., Zhang, R., Wang, Q., Sun, Y., Fu, J. S., Chen, Y., Xu, D., & Wang, W. (2010). Mixing and transformation of Asian dust with pollution in the two dust storms over the northern China in 2006. *Atmospheric Environment*, *44*(28), 3394–3403. https://doi.org/10.1016/j.atmosenv.2010.06.011

Appendix

Appendix A: Tables of mean mass concentration, variation of water-soluble inorganic ions, metals, meteorological parameters, correlation between the WSIIs, deposition fluxes and new potential production during the sampling period and each dust storm event.

The variation means the difference of species concentration during the dust episode minus the concentration during the non-dust day's samples and then divided by the concentration during the non-dust episode.

Appendix A I. Summary of the PM_{10} aerosol chemical component mass concentrations observed from January 27 to February 18, 2022, at CVAO. The minimum (Min), maximum (Max), average (Mean), and standard deviation (Std) values are in ng m^{-3} for the species highlighted in light green. The remaining species are in µg m^{-3}.

Elements	Whole Period(n=22)				Dust Period(n=11)				Non-Dust Period(n=11)			
	Min	Max	Mean	Std	Min	Max	Mean	Std	Min	Max	Mean	Std
PM_{10}	0.72	250.00	67.72	70.10	59.07	250.00	118.80	66.40	0.72	35.66	16.64	13.00
Cl^-	1.46	9.09	4.92	1.92	2.89	9.09	6.03	1.86	1.46	6.20	3.81	1.26
NO_3^-	0.28	2.44	1.51	0.66	0.97	2.44	1.85	0.52	0.28	2.19	1.17	0.62
SO_4^{2-}	1.91	9.44	4.94	1.59	3.92	9.44	5.92	1.51	1.91	5.45	3.96	0.94
Na^+	6.90	17.70	14.55	2.33	13.16	17.70	15.65	1.51	6.90	17.17	13.45	2.55
Ca^{2+}	0.01	2.75	0.93	0.71	0.34	2.75	1.32	0.72	0.01	1.56	0.55	0.46
NO_2^-	4.94	21.59	13.16	4.01	8.81	19.16	13.71	3.11	4.94	21.59	12.61	4.84
F^-	52.70	284.26	183.33	63.81	134.86	218.74	186.97	26.39	52.70	284.26	179.70	88.45
PO_4^{3-}	15.81	67.57	48.51	12.10	41.92	67.57	54.44	8.43	15.81	56.82	42.58	12.61

NH_4^+	28.64	120.43	75.53	19.98	56.48	107.18	78.42	13.75	28.64	120.43	72.65	25.12
K^+	67.45	475.53	282.05	105.08	236.19	475.53	350.58	83.01	67.45	318.17	213.52	77.23
Mg^{2+}	1.82	290.74	100.88	82.80	37.24	290.74	143.09	86.43	1.82	163.73	58.67	54.83
Al	0.30	6.77	2.07	1.84	0.55	6.77	3.11	2.09	0.30	2.26	1.03	0.61
P	0.17	1.83	0.76	0.44	0.38	1.83	0.93	0.63	0.17	1.22	0.68	0.32
Ti	1.14	9.39	4.40	2.80	1.33	9.39	5.36	3.12	1.14	7.22	3.45	2.18
V	0.025	0.142	0.076	0.039	0.025	0.142	0.077	0.044	0.027	0.136	0.075	0.037
Fe	0.045	6.78	2.06	2.22	0.52	6.78	3.63	2.17	0.045	1.73	0.49	0.47
Zn	0.07	0.42	0.26	0.09	0.20	0.42	0.28	0.07	0.07	0.39	0.23	0.10
Ag	0.33	2.53	1.07	0.56	0.60	2.53	1.38	0.60	0.33	1.36	0.75	0.28
Ba	1.47	7.88	3.44	1.27	2.32	4.19	3.08	0.64	1.47	7.88	3.81	1.64
Sc	18.32	506.14	101.19	106.42	18.32	506.14	130.16	139.37	20.55	164.89	72.21	50.13
Cr	2.06	76.41	26.06	21.94	5.02	76.41	38.81	23.75	2.06	29.28	13.30	9.43
Mn	26.46	1185.72	412.91	406.21	95.58	1185.72	690.72	412.88	26.46	298.41	135.10	79.05
Ni	1.48	52.30	20.40	20.38	7.44	52.30	35.95	18.27	1.48	8.99	4.84	2.44
Ir	9.48	1752.51	538.45	635.71	151.73	1752.51	1009.81	595.46	9.48	177.63	67.10	72.83

Appendix A II Variation in mass concentrations during the dust and non-dust storm periods from January 27 to February 18, 2022, at CVAO. The average (Mean) values are µg/m³.

Whole Sampling Period			
Species	**Mean mass concentration during the non-dust period**	**Mean mass concentration during the dust period**	**Variation (%)**
PM10	16.64	118.80	614%
Cl-	3.81	6.03	58%
NO3-	1.168	1.855	59%
SO4-	3.959	5.924	50%
NO2-	0.013	0.014	9%
F-	0.180	0.187	4%

PO43-	0.043	0.054	28%
Na+	13.447	15.646	16%
NH4+	0.073	0.078	8%
K+	0.214	0.351	64%
Mg2+	0.059	0.143	144%
Ca2+	0.551	1.318	139%
Al	1.028	3.111	203%
P	0.677	0.934	38%
Ti	3.446	5.357	55%
V	0.075	0.077	3%
Cr	0.013	0.039	192%
Fe	0.492	3.629	637%
Ni	0.005	0.036	642%
Zn	0.229	0.282	23%

Appendix A III. Summary of the PM_{10} aerosol chemical component mass concentrations and the meteorological parameters during each dust storm event from January 27 to February 18, 2022, at CVAO. The minimum (Min), maximum (Max), average (Mean), and standard deviation (Std) values are in μg/m³. DS1, DS2, and DS3 stand for dust storm 1, dust storm 2, and dust storm 3, respectively. Temp, RH, W_speed, and Vd mean temperature(ºC), relative humidity (%), wind speed (m s^{-1}) and depositional velocity (mm s^{-1}), respectively.

	DS1				**DS2**				**DS3**			
	Min	**Max**	**Mean**	**Std**	**Min**	**Max**	**Mean**	**Std**	**Min**	**Max**	**Mean**	**Std**
PM_{10}	59.07	241.33	118.86	63.66	61.25	123.53	84.91	33.73	88.98	250.00	169.49	113.86
Temp	20.74	21.74	21.38	0.41	21.01	21.23	21.15	0.12	20.84	21.29	21.07	0.32
RH	78.94	84.53	80.75	1.97	77.99	81.11	79.62	1.56	73.17	78.45	75.81	3.74
W_speed	5.68	10.53	8.75	2.02	6.92	10.52	8.40	1.88	9.58	11.02	10.30	1.02
Pressure	1015.14	1016.44	1015.90	0.44	1014.54	1017.03	1015.64	1.27	1015.86	1016.94	1016.40	0.76
Radiation	68.49	220.35	170.22	57.03	127.15	211.25	164.27	42.91	84.06	203.79	143.93	84.66
Vd	0.70	0.95	0.85	0.11	0.74	0.95	0.83	0.11	0.89	0.99	0.94	0.07

NO3-	0.97	2.37	1.71	0.61	1.94	2.20	2.09	0.13	1.45	2.44	1.95	0.70
SO4-	3.92	9.44	5.86	1.98	4.78	6.77	5.94	1.03	5.42	6.79	6.11	0.97
NO2-	0.012	0.017	0.014	0.002	0.012	0.019	0.015	0.003	0.009	0.010	0.009	0.001
PO43-	0.04	0.06	0.06	0.01	0.04	0.07	0.06	0.01	0.05	0.05	0.05	0.01
NH4+	0.056	0.093	0.073	0.013	0.079	0.107	0.088	0.016	0.078	0.081	0.079	0.002
K+	0.24	0.48	0.34	0.10	0.28	0.38	0.35	0.06	0.29	0.47	0.38	0.12
Mg^{2+}	0.04	0.29	0.13	0.10	0.09	0.27	0.17	0.09	0.08	0.19	0.14	0.08
Ca^{2+}	0.34	2.75	1.22	0.90	1.23	2.22	1.64	0.51	0.83	1.45	1.14	0.44
Al	0.55	6.77	3.25	2.35	1.03	5.27	3.47	2.19	0.709	3.569	2.139	2.022
P	0.38	0.49	0.43	0.07	0.62	1.36	0.99	0.53	1.83	1.83	1.83	-
Ti	1.33	9.39	5.11	3.59	1.77	9.01	5.78	3.68	3.90	7.01	5.45	2.20
V	0.025	0.142	0.077	0.052	0.030	0.135	0.081	0.052	0.068	0.076	0.072	0.006
Cr	0.01	0.05	0.03	0.02	0.01	0.07	0.04	0.03	0.05	0.08	0.07	0.02
Fe	0.52	5.25	3.04	2.03	0.811	5.090	3.064	2.148	5.687	6.776	6.232	0.770
Ni	0.008	0.052	0.033	0.020	0.007	0.045	0.031	0.021	0.049	0.052	0.051	0.002
Zn	0.20	0.29	0.24	0.034	0.212	0.365	0.285	0.077	0.357	0.423	0.390	0.046

Appendix A IV. Variation in mass concentrations of the PM_{10} aerosol chemical component during each dust storm event from January 27 to February 18, 2022, at CVAO. The average (Mean) and the reference values are in µg/m³. The reference is the sample collected immediately before the dust storm outbreak.

	DS1			**DS2**			**DS3**		
	Reference 29-01-2022	**Mean**	**Variation**	**Reference 08-02-2022**	**Mean**	**Variation**	**Reference 16-02-2022**	**Mean**	**Variation**
PM10	3.28	118.86	3524%	35.66	84.91	138%	22.38	169.49	657%
NO3-	0.28	1.71	511%	1.24	2.09	68%	1.32	1.95	48%
SO4-	1.91	5.86	206%	4.48	5.94	33%	5.03	6.11	21%
NO2-	0.005	0.01	188%	0.018	0.015	-16%	0.010	0.009	-3%
PO43-	0.02	0.06	250%	0.05	0.06	11%	0.04	0.05	20%
NH4+	0.03	0.07	156%	0.06	0.09	48%	0.080	0.079	-1%
K+	0.07	0.34	407%	0.24	0.35	45%	0.28	0.38	36%
Mg2+	0.002	0.13	7238%	0.02	0.17	580%	0.140	0.136	-3%
Ca2+	0.013	1.22	9517%	0.37	1.64	341%	0.84	1.14	36%
Al	0.30	3.25	974%	1.19	3.47	192%	1.05	2.14	103%
P	0.17	0.43	157%	0.98	0.99	1%	0.57	1.83	220

Ti	1.30	5.11	293%	2.64	5.78	119%	4.97	5.45	10%
V	0.027	0.077	187%	0.05	0.08	61%	0.10	0.07	-28%
Cr	0.002	0.03	1355%	0.01	0.04	381%	0.012	0.07	470%
Fe	0.045	3.04	6736%	0.60	3.06	411%	0.37	6.23	1566%
Ni	0.001	0.033	2157%	0.01	0.03	309%	0.004	0.05	1285%
Zn	0.12	0.24	102%	0.22	0.28	27%	0.27	0.39	43%

Appendix A V. Pearson correlation matrices (P and R values) for water-soluble irons in the non-dust periods (upper triangle) in violet and dust event periods (lower triangle) in green. The p-values are in brackets. Only correlation R > 0.7 and p-values < 0.02 are highlighted in colours

Ions	NO_3^-	SO_4^{2-}	NO_2^-	PO_4^{3-}	NH_4^+	K^+	Mg^{2+}	Ca^{2+}
NO_3^-		**0.781 (.003)**	0.557 (.060)	**0.834 (.001)**	0.658 (.020)	**0.924 (<.001)**	**0.833 (.001)**	**0.936 (<.001)**
SO_4^{2-}	**0.713 (.014)**		0.467 (.125)	**0.790 (.002)**	0.588 (.044)	**0.912 (<.001)**	**0.780 (.003)**	**0.831 (.001)**
NO_2^-	-0.299 *(.372)*	-0.290 *(.387)*		**0.771 (.003)**	0.400 (.198)	0.542 (.068)	0.204 (.525)	0.423 (.171)
PO_4^{3-}	0.213 *(.529)*	-0.034 *(.920)*	0.196 *(.564)*		0.590 (.043)	**0.886 (<.001)**	0.605 (.037)	**0.759 (.004)**
NH_4^+	**0.815 (.002)**	0.685 *(.020)*	-0.454 *(.161)*	0.351 *(.290)*		**0.740 (.006)**	0.596 (.041)	0.631 (.028)
K^+	**0.900 (<.001)**	**0.838 (.001)**	-0.367 *(.267)*	0.245 *(.468)*	**0.759 (.007)**		**0.856 (<.001)**	**0.914 (<.001)**
Mg^{2+}	**0.877 (<.001)**	**0.780 (.005)**	-0.302 *(.366)*	0.109 *(.750)*	**0.788 (.004)**	**0.882 (<.001)**		**0.942 (<.001)**
Ca^{2+}	**0.850 (.001)**	**0.836 (.001)**	-0.163 *(.631)*	0.117 *(.732)*	**0.796 (.003)**	**0.850 (.001)**	**0.959 (<.001)**	

Appendix A VI .Correlation coefficients between water-soluble inorganic ions and meteorological factors. in the non-dust periods in red and dust event periods in light blue. The p-values are in brackets. The following terms Temp, RH, SR stand for temperature, relative humidity and solar radiation, respectively.

	Temp	Pressure	RH	SR	Temp	Pressure	RH	SR
SO_4^{2-}	0.419 *(.200)*	-0.168 *(.621)*	0.135 *(.691)*	-0.517 *(.104)*	-0.003 *(.992)*	-0.143 *(.658)*	0.552 *(.063)*	0.066 *(.839)*
NO_3^-	0.525 *(.097)*	-0.241 *(.476)*	-0.013 *(.969)*	-0.288 *(.390)*	0.140 *(.664)*	0.048 *(.882)*	***0.682 (.015)***	0.449 *(.143)*
NO_2^-	0.083 *(.807)*	-0.445 *(.170)*	0.333 *(.317)*	0.222 *(.512)*	0.306 *(.333)*	***-0.680 (.015)***	0.105 *(.745)*	0.482 *(.113)*
PO_4^{3-}	0.254 *(.451)*	***-0.658 (.028)***	0.104 *(.762)*	0.243 *(.472)*	0.318 *(.313)*	-0.326 *(.300)*	***0.618 (.032)***	0.369 *(.237)*
NH_4^+	0.234 *(.490)*	-0.326 *(.328)*	-0.037 *(.915)*	-0.207 *(.542)*	0.093 *(.774)*	0.098 *(.762)*	***0.667 (.018)***	0.099 *(.758)*
Mg^{2+}	0.311 *(.351)*	-0.015 *(.966)*	0.036 *(.917)*	-0.183 *(.590)*	-0.020 *(.952)*	0.395 *(.203)*	***0.739 (.006)***	0.038 *(.906)*
Ca^{2+}	0.285 *(.396)*	-0.190 *(.575)*	-0.009 *(.979)*	-0.126 *(.711)*	0.029 *(.929)*	0.198 *(.537)*	***0.669 (.017)***	0.241 *(.450)*
K^+	0.439 *(.177)*	-0.142 *(.677)*	-0.006 *(.986)*	-0.344 *(.301)*	0.119 *(.713)*	-0.019 *(.953)*	***0.743 (.006)***	0.242 *(.449)*

PM_{10}	0.295 *(.378)*	-0.072 *(.833)*	-0.004 *(.992)*	-0.474 *(.141)*	0.288 *(.364)*	-0.536 *(.073)*	0.374 *(.231)*	0.269 *(.398)*

Appendix A VII . Mean ± standard deviation of dry inorganic N and P, and trace metals deposition fluxes (µmol m^{-2} d^{-1}) at Cape Verde Atmospheric Observatory, calculated during both dust and non-dust and sampling periods. The flux of PM_{10} is in mg m^{-2} d^{-1}

Deposition fluxes (µmol m^{-2} d^{-1})			
	Sampling period(n=22)	**Dust Period(n=11)**	**Non-dust Period(n=11)**
PM_{10}	5.0 ± 5.4	9.4 ± 5.25	0.075± 0.008
NO_3^-	1.8 ± 0.8	2.2 ± 0.7	1.5 ± 0.8
SO_4^{2-}	3.8 ± 1.3	4.6 ± 1.3	3.2 ± 0.9
NO_2^-	0.021 ± 0.007	0.021 ± 0.004	0.021 ± 0.008
PO_4^{3-}	0.04 ± 0.01	0.04 ± 0.01	0.03 ± 0.01
NH_4^+	0.3 ± 0.1	0.3 ± 0.1	0.3 ± 0.1
K^+	0.5 ± 0.2	0.7 ± 0.2	0.4 ± 0.2
Mg^{2+}	0.3 ± 0.3	0.4 ± 0.3	0.2 ± 0.2
Ca^{2+}	1.7 ± 1.3	2.5 ± 1.4	1.1 ± 0.9
Al	5.8 ± 5.2	8.6± 6.0	2.9 ± 1.7
P	1.8 ± 1.1	2.2 ± 1.6	1.6 ± 0.8
Ti	6.9 ± 4.5	8.4 5± 5.05	5.4 ± 3.4
V	0.11± 0.06	0.11 ± 0.07	0.11± 0.05
Cr	0.04 ± 0.03	0.05 ± 0.04	0.02 ± 0.02
Fe	2.82 ± 3.11	5.00 ± 3.11	0.66 ± 0.65
Ni	0.03 ± 0.03	0.05 ± 0.03	0.01 ± 0.01
Zn	0.29 ± 0.11	0.32 ± 0.09	0.26 ± 0.12
DIN	2.2 ± 0.9	2.6 ± 0.7	1.8 ± 0.8

Appendix A VIII. Summary of the potential new production supported by DIN and DIP from January 27 to February 18, 2022, at CVAO. The minimum (Min), maximum (Max), average (Mean), and standard deviation (Std) values are in µg C m^{-2} d^{-1}. N_P_DIN stands for new production supported by DIN, N_P_DIP stands for new production supported by DIP and Total_Prod stands for new production supported by DIN +DIP.

	Whole sampling period			Dust episodes			Non-dust episodes		
	N_P_DIN	N_P_DIP	Total_Prod	N_P_DIN	N_P_DIP	Total_Prod	N_P_DIN	N_P_DIP	Total_Prod
Min	39.12	16.80	55.93	97.42	34.08	141.75	39.12	16.80	55.93

Max	268.75	69.04	334.57	268.75	69.04	334.57	248.11	58.97	307.08
Mean	171.56	48.50	220.05	205.36	54.46	259.82	137.75	42.53	180.29
Std	70.94	12.96	81.34	59.16	11.30	66.21	67.49	12.11	77.66